

NASA CR

130077



(NASA-CR-130077) DEVELOPMENT AND  
FABRICATION OF A CHARGEABLE MAGNET SYSTEM  
FOR SPACECRAFT CONTROL Final Report  
(Ithaco, Inc.) 27 Jul. 1972 195 p CSCL

N72-33872

Unclas  
22B G3/31 45309



ITHACA, N.Y.

NASA CR-



130077

Design Study Report  
and  
Final Report

Contract NAS 5-21170

Development and Fabrication of a  
Chargeable Magnet System for  
Spacecraft Control

Prepared By

ITHACO, Inc.  
735 West Clinton Street  
Ithaca, New York 14850

Prepared For

National Aeronautics and Space Administration  
Goddard Space Flight Center  
Greenbelt, Maryland 20771

July 27, 1972

## TABLE OF CONTENTS

- I Design Study Report  
Chargeable Permanent Magnets
  - 1.0 Introduction
  - 2.0 Fundamentals
  - 3.0 Can
  - 4.0 Coil
  - 5.0 Magnet Weight
  - 6.0 Summary design curves for estimated size, weight, and power of variable permanent magnets
  - 7.0 Description of final magnet design and performance
- II Magnetic Acquisition System Implementation
  - 1.0 Introduction
  - 2.0 Description of Hardware
  - 3.0 Magnetometer Noise Measurements
  - Appendices
- III Electronics for Control of Variable Permanent Magnets
  - 1.0 Introduction
  - 2.0 Control Electronics
  - 3.0 Variable Permanent Magnet Breadboard Controller
- IV Horizon Scanner Breadboard
  - 1.0 Introduction
  - 2.0 Description of the X Scanner
  - 3.0 Operational Description
  - 4.0 Figures
  - Appendices

## INTRODUCTION

The work accomplished under the subject contract includes the following:

1. Chargeable permanent magnet technology development
2. Magnetometer development (Mod #4)
3. Horizon scanner breadboard (Mod #9)
4. Implementation of a Magnetic Acquisition System (Mod #11)
5. Development of electronics for dynamic closed loop operation of chargeable permanent magnets (Mod #12)

This report constitutes the final report on this contract and includes the Design Study Report on chargeable permanent magnets as well as summaries of all other work done under the contract.



# **I    DESIGN STUDY REPORT**

## **VARIABLE PERMANENT MAGNETS**

**1.0    Introduction**

**2.0    Fundamentals**

**3.0    Can**

**4.0    Coil**

**5.0    Magnet Weight**

**6.0    Summary design curves for estimates size, weight, and  
power of variable permanent magnets**

**7.0    Description of final magnet design and performance**

# I DESIGN STUDY REPORT - VARIABLE PERMANENT MAGNETS

## 1.0 Introduction

This design study report describes the work done under the subject contract on the design of variable permanent magnets for use in magnetic balancing and control of earth orbiting spacecraft. These magnets can be used instead of air core coils or electromagnets in applications where the objective is to produce, or eliminate, torque on the spacecraft through interaction with the earth's magnetic field. Such magnets are particularly useful for on-orbit magnetic balancing to minimize the effects of magnetic disturbance torques. Once the appropriate moment is achieved (by command), the magnet controller is turned off and the moment will be maintained indefinitely with no power.

For magnetic control applications, these magnets can have substantial power advantages where larger magnets are involved and where frequency of switching is low.

This report deals with design of the magnet for minimum size and weight, and describes the sensing configuration used for monitoring the state of the magnet.

## 2.0 FUNDAMENTALS

### 2.1 Magnetic Poles

In treating permanent magnets, it becomes convenient to deal with free magnetic poles in analogy to the free charges in electrostatics. A unit pole is defined so that two unit poles with a separation of one centimeter in vacuum would experience a force of one dyne, and the magnetic field strength (H) is defined as the force on a unit pole in this field. The fundamental relations giving the force (F) and the magnetic field strength (H) are

$$(2-1) \quad F = m H$$

$$(2-2) \quad H = \frac{m}{r^2}$$

where m is the pole strength and r is the distance from the pole. When two magnets are brought closely together in an end to end orientation, the force between the magnets is given by

$$(2-3) \quad F = \frac{m_1 m_2}{r^2}$$

provided the separation is small compared to the magnet length.

The effects of magnetic material are measured by the intensity of magnetization I -- which is the number of unit poles per cross sectional area. And because the dipole moment is the pole strength times separation, the intensity is also the magnetic moment density.

$$(2-4) \quad M = m\ell$$

$$(2-5) \quad I = \frac{M}{\text{volume}}$$

Early experimenters conceived of magnetism as a flow of magnetic flux -- perhaps because of the patterns formed in iron filings by the magnetic field. This flow was characterized by lines of induction which have the same direction as the magnetic field and indicate the flow by their concentration. The induction is the sum of the effect due to H and to I and is defined by

(2-6)

$$B = H + 4\pi I$$

where the factor  $4\pi$  occurs because a unit pole gives a unit magnetic field at unit distance, and the surface of a unit sphere is  $4\pi$ . The effects of material are often expressed for linear materials in the more familiar expression

(2-7)

$$B = \mu H$$

## 2.2 Self-Demagnetization and Geometry Effects

Within a magnetic material, we find an interesting effect which is quite important in our study of permanent magnets. In figure 2-1, a unit magnetic dipole is shown with its lines of induction. As is quite obvious, the direction of the magnetic field off the end of this dipole is aligned with the dipole so that another dipole in this position (shown dotted) would find an aiding field. Now consider a position to the side of this dipole; the dipole field is counter to the sense of the dipole, and a dipole of the same sense would find an opposing field in this region. The implications are quite clearly that: first, magnetic material generates its own demagnetizing field; and second, this effect can be minimized by selecting a long slender geometry.

The same result may be obtained by considering a current loop as the source of magnetic field because the field due to a current loop with infinitesimal dimensions is the same as the field due to a dipole of infinitesimal dimensions. The differential magnetizing force due to a differential current element ( $i \, d\vec{l}$ ) at a distance  $r$  is

$$(2-8) \quad \vec{dH} = \frac{i}{10} \frac{d\vec{l} \times \hat{r}}{r^2}$$

where  $\hat{r}$  is a unit vector directed from the current element to the point of observation.

The magnetic moment of a current loop may be calculated from

$$(2-9) \quad M = \frac{i}{10} (\text{Area})$$

It should be realized that the magnetic moment of a current loop is defined such that a current loop with unit magnetic moment will give unit torque in a field with flux density ( $B$ ), but a unit dipole is defined to give a unit torque with unit magnet field strength ( $H$ ).

Although these two types of moment are dimensionally different, they will give the same numerical results in air in systems of units where  $\mu$  equals one.

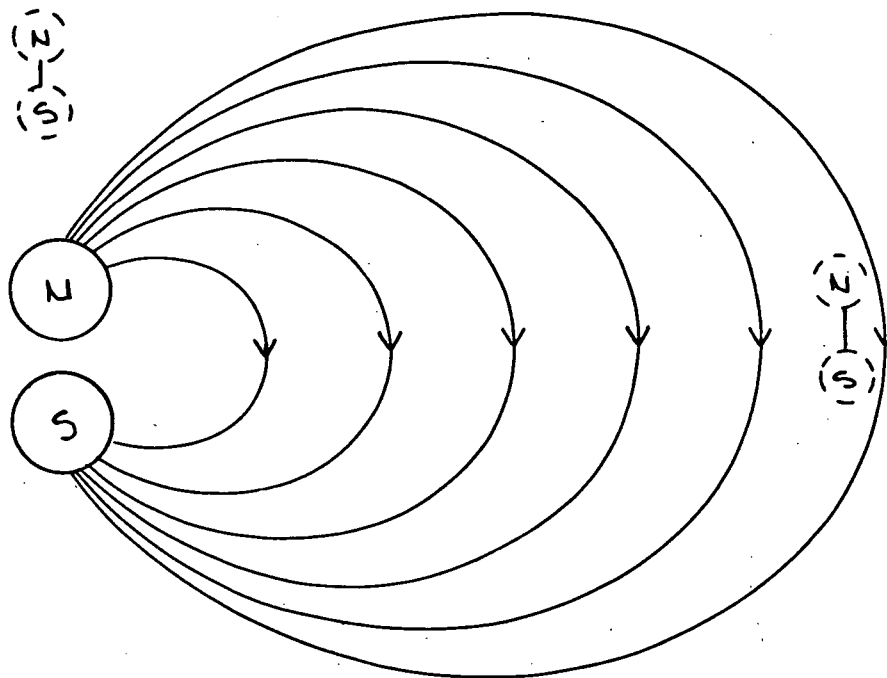


Figure 2-1 Field due to a Magnetic Dipole

From this we can readily see that the conversion to mks units is one pole cm equals  $10^{-3}$  ampere meter<sup>2</sup>.

Several researchers have investigated self-demagnetization effects, but most magnetic materials are highly nonlinear and quantitative information is usually obtained from graphed experimental data. This data has been summarized to reasonable accuracy by assuming that the self-demagnetizing field near the center of the magnet is proportional to induction and formulating an empirical equation for the proportionality constant. The proportionality constant is taken to be a function of only the geometry and is given for long slender bars<sup>1</sup> by

$$(2-10) \quad \left(\frac{B}{H}\right)_D = \sqrt{\frac{.49\pi}{2}} \frac{\sqrt{p}}{a} \left(\frac{l}{D}\right) \sqrt{\frac{l}{D} + 2 \frac{a}{p}}$$

where  $l$  is the magnet length,  $D$  is the width of the bar,  $pD$  is the perimeter of the cross section, and  $aD^2$  is the cross sectional area.

Again, this is an empirical relation giving only the self-demagnetizing force near the center of the magnet and makes no attempt to include the effect of properties of the material on the field distribution, but results obtained from this relation have been quite accurate.

Using the assumption that the self-demagnetizing force is proportional to induction in the center of a magnet, we may determine the induction and effective net magnetizing force quite simply by using the load line technique. This technique is best described by example.

<sup>1</sup>Parker & Studders (Ref. 8) page 165

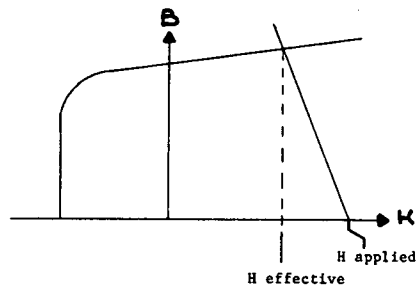


Figure 2-2 Load Line Example

Turning to Figure 2-2, the procedure is simply to draw a load line of slope  $-(B/H)_D$  through the H axis at the applied magnetizing force on a graph of B vs H for the material. This line represents the locus of all points which satisfy

$$B = \left(\frac{B}{H}\right)_D (H_{\text{applied}} - H)$$

so the intersection of this line with the B-H curve of the material indicates both the net magnetizing force seen by the material, and the corresponding induction.

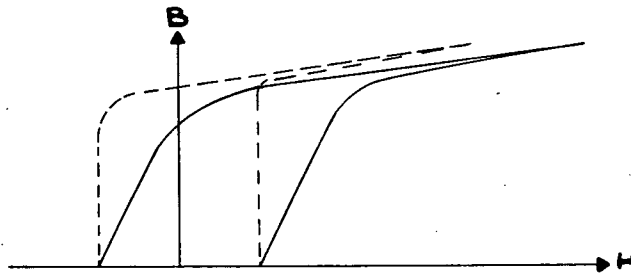


Figure 2-3 Typical Sheared B-H Curve

The same result can also be obtained by redrawing the B-H curve of the material for a specific geometry so that the self-demagnetizing effects are included in the sheared curve. Figure 2-3 shows the effect of shearing on a typical curve shape.

Before leaving the subject of self-demagnetization, one observation will be noted. This is the effect of shearing on the slope of the curve. It is easily shown either through differential calculus or plane geometry that slopes on the sheared curves can be determined from the original slope, and the load line slope, from

$$(2-11) \quad \left( \frac{\partial B}{\partial H} \right)_{\text{sheared}} = \left( \frac{\partial B}{\partial H} \right)_{\text{old}} + \left( \frac{B}{H} \right)_D$$

which is to say that slopes add like resistances in parallel. Very small slopes will be unchanged in the sheared curve, but slopes much greater than  $(B/H)_D$  will appear in the sheared curve with a slope of  $(B/H)_D$ .

These considerations will allow us to determine the flux density at the center of the bar, but it remains to determine the effect of the spatial distribution of magnetic intensity (or dipole moment density). As our interest here is with macroscopic effects, we need only a gross measure as an average.

Recalling equation 2-6, if we take averages over the entire magnet we have

$$(2-12) \quad \text{Avg}(B) = \text{Avg}(H) + \text{Avg}(4\pi I) \quad (\text{from 2-6})$$

because averaging (arithmetic mean) is a linear process. Fortunately, experimental work has been done to determine the leakage of induction lines from the sides of a bar magnet. From this we can readily determine the average flux density, then using the load line slope we can determine the self-demagnetizing force and if we know the average applied magnetizing force we have the average magnetic intensity.

Figure 2-4 is a graph showing the empirical relationship between average induction in a bar magnet and slenderness ratio  $l/D$ .



The significant point is that for  $\ell/D$  ratios greater than 4, the induction averaged over the volume of the bar is 70% of the maximum induction at any point in the bar. The discrepancy between predicted magnetic moment and measured moment for magnets with  $\ell/D$  ratios from 12 to 50 ranged from -1% to +7%.

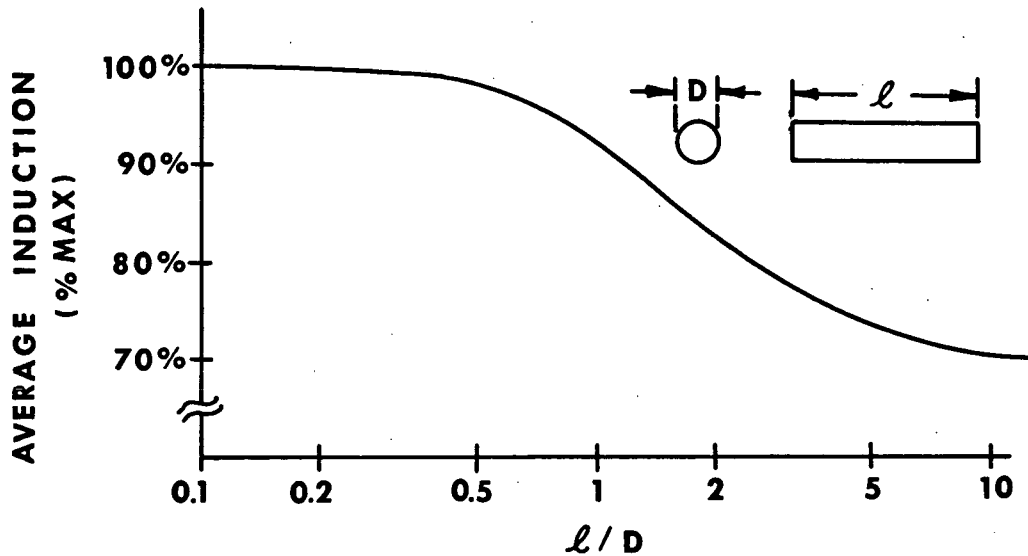


Figure 2-4 Effect of Slenderness on Average Induction

### 2.3. Magnetizing Coils

The standard approximation for the magnetizing force due to a coil wound on a long bar is

$$(2-13) \quad H = \frac{4\pi}{10} \frac{ni}{\ell_c}$$

where  $ni$  is the number of ampere-turns, and  $\ell_c$  is the coil length.

In order to determine limits on the validity of this approximation, we return to equation 2-8 and calculate the magnetic field on the axis of symmetry for several current distributions with cylindrical symmetry. The coordinate system and applicable dimensions are shown in figure 2-5. Note that a uniform radial current distribution is assumed for all cases, and that distance is measured from the coil center so the coil ends are at  $z = \pm \frac{\ell_c}{2}$

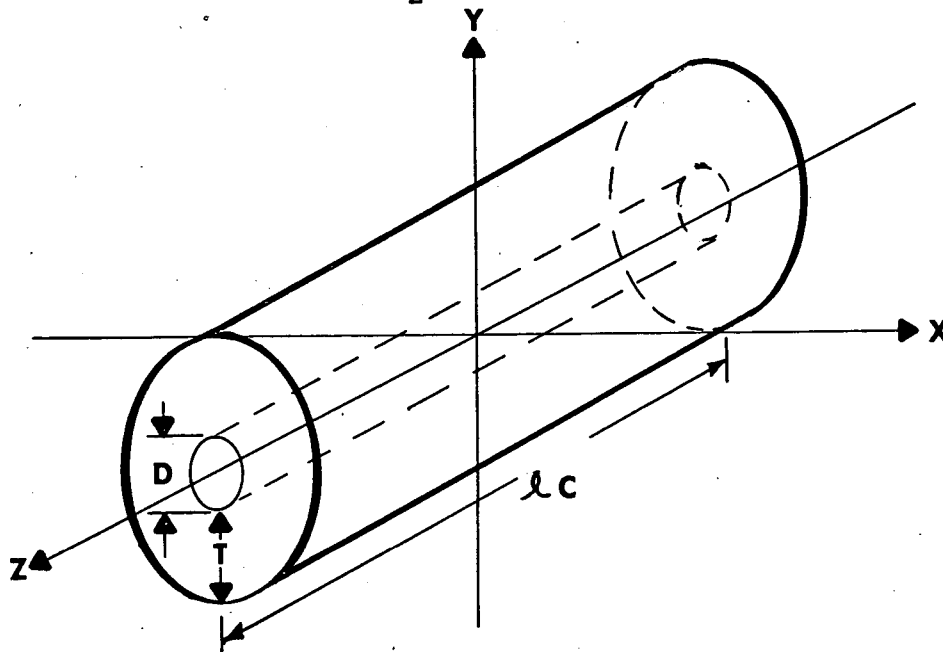


Figure 2-5 Coil Dimensions

Without showing details of the mathematics, the results are:

for a circular current filament

$$(2-14) \quad H = \frac{4\pi}{10} \frac{ni}{D} \left[ 1 + \left( \frac{2z}{D} \right)^2 \right]^{-3/2}$$

for a current disc ( $l = 0$ )

$$(2-15) \quad H = \frac{4\pi}{10} \frac{ni}{2T} \left\{ \frac{1}{\sqrt{1 + \left(\frac{2z}{D+2T}\right)^2}} - \frac{1}{\sqrt{1 + \left(\frac{2z}{D}\right)^2}} \right. \\ \left. + \ln \left[ \frac{D}{D+2T} \frac{1 + \sqrt{1 + \left(\frac{2z}{D}\right)^2}}{1 + \sqrt{1 + \left(\frac{2z}{D+2T}\right)^2}} \right] \right\}$$

for a cylindrical current sheath ( $T = 0$ )

$$(2-16) \quad H = \frac{2\pi}{10} \frac{ni}{l} \left\{ \frac{l + 2z}{\sqrt{D^2 + (2z+l)^2}} + \frac{l - 2z}{\sqrt{D^2 + (2z-l)^2}} \right\}$$

for a hollow cylinder of current

$$(2-17) \quad H = \frac{2\pi}{10} \frac{ni}{l} \left\{ \frac{2z+l}{2T} \ln \left[ \frac{D+2T}{D} \frac{1 + \sqrt{1 + \left(\frac{2z+l}{D+2T}\right)^2}}{1 + \sqrt{1 + \left(\frac{2z+l}{D}\right)^2}} \right] \right. \\ \left. - \frac{2z-l}{2T} \ln \left[ \frac{D+2T}{D} \frac{1 + \sqrt{1 + \left(\frac{2z-l}{D+2T}\right)^2}}{1 + \sqrt{1 + \left(\frac{2z-l}{D}\right)^2}} \right] \right\}$$

The cylindrical current sheath has a particularly simple expression for magnetizing force which is convenient to establish bounds on the  $H$  distribution of the hollow cylinder. The field distribution of the hollow cylinder will be between the two distributions given by cylindrical sheaths with diameters  $D$  and  $D+2T$ .

Inspection of equation 2-16 reveals two useful facts. First, the field maximum occurs at the coil center ( $z=0$ ) and approaches  $0.4\pi ni/l$  asymptotically from below with increasing length. The length to diameter ratio which gives 10% error is easily shown to be  $(l/D)=2$  while an  $(l/D)$  of 7 gives 1% error. This confirms equation 2-13 even for quite short coils.

The field at the coil end is very nearly half the field at the coil center for  $(\ell/D)$  as low as 2 and monotonically approaches half the maximum field as  $(\ell/D)$  increases. The variation for intermediate positions is shown in figure 2-6.

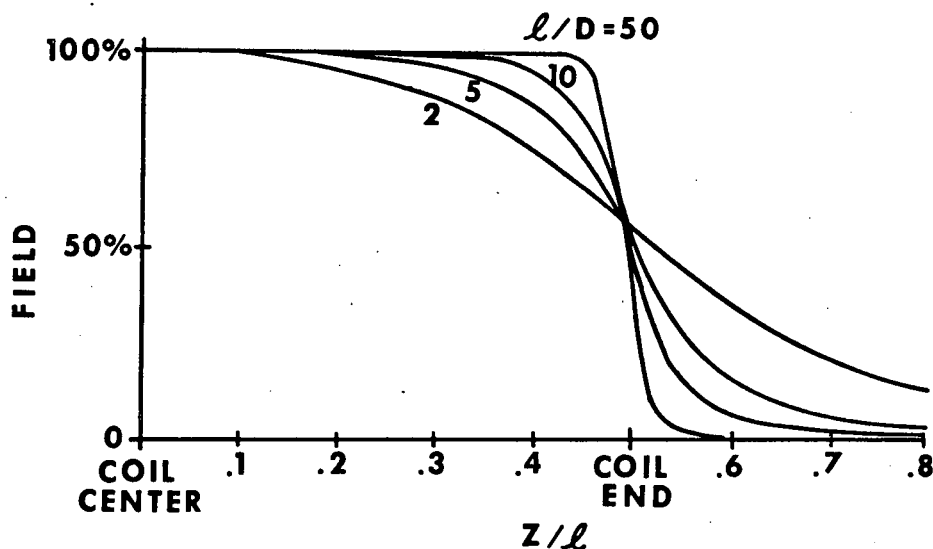


Figure 2-6 Magnetic Field Strength Normalized to  $0.4\pi ni/\ell_c$  vs position

While equation 2-17 could be graphed in a similar manner, the addition of a third variable (coil thickness) provides little additional information.

#### 2.4 Magnetic Moment Measurement

Laboratory measurement of magnetic dipole moment may be, in principle, accomplished by either making a torque measurement in a calibrated magnetic field, or by making magnetic measurements on the magnet.

The most obvious method is a direct torque measurement, but the torque requirements for small satellites have historically been in the vicinity of  $10^{-2}$  Newton-meters ( $10^{-3}$  in-lb). It would seem that such delicate torque measurements could be circumvented by scaling either the magnet dimensions or the ambient magnetic field, but both of these approaches have serious drawbacks.

Because the magnetic core material must be cold worked to develop the magnet properties, scaling the core dimensions will require the magnetic material manufacturer to scale the size of the cast billet. If this is not done, the material must be worked to a different degree and the finished stock will exhibit different magnetic properties.

The second approach is even less desirable if a significant scaling is required. Should the ambient magnetic field be increased, the magnetic state of the core material will be altered. As the core material is highly nonlinear, test results could not be linearly scaled.

The magnetic moment of a bar magnet can in theory be determined by averaging the flux density within the magnet -- but this requires detailed knowledge of the field distribution within the magnet.

The flux density within a permanent magnet is not readily measured but another method is available for determining the average magnetic intensity.

Consider a magnet of length  $\ell$  and the magnetic field due to this magnet being measured at a distance  $R$  as shown in figure 2-7.

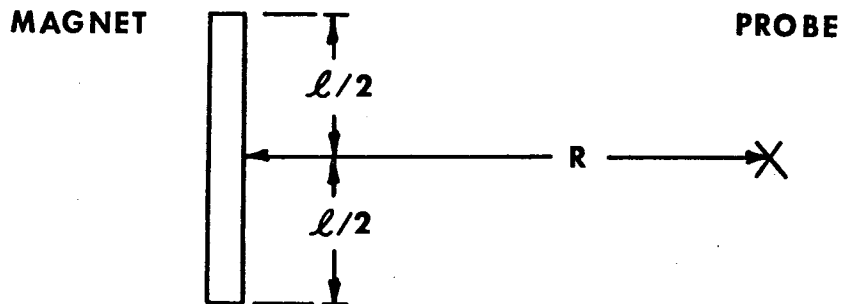


Figure 2-7 Position of Magnet & Test Probe  
for Moment Measurement

If we consider the magnet to be two equal and opposite poles of strength  $m$  and separation  $\ell$ , then the field at the measurement point will be

$$(2-18) \quad H = \frac{m\ell}{(R^2 + \frac{\ell^2}{4})^{3/2}}$$

but  $B = H$  in air, and the moment is  $m\ell$ . Therefore, we can calculate the dipole moment by making a remote measurement of the magnetic field and calculating the moment from

$$(2-19) \quad M = BR^3 \left( 1 + \frac{\ell^2}{4R^2} \right)^{3/2}$$

This relation will be in error for any magnet because the effective magnetic length is not known precisely, and when the measurement is made very close to the magnet the effect of local flux density variations within the magnet may give significant error. Both of these effects diminish rapidly with increased measurement distance, with the effect of local variations decreasing at least as the fifth power of separation.

Ignoring flux density variations within the magnet for the moment, we may determine the sensitivity of the measurement to probe placement and to uncertainty in the effective length of the magnet. This information can then be used to balance the error caused by the magnetic environment against the errors due to probe placement and uncertainty in magnet length.

Consider two attempts at measuring the dipole moment of a magnet. Let one measurement be error free and the other measurement made with an error  $\delta$  in probe distance and a relative error  $\gamma$  in determining the magnet length. The relative measurement error is then

$$(2-20) \quad \epsilon = \left( \frac{R^2 + \frac{\ell^2}{4}}{(R+\delta)^2 + \frac{(1+\gamma)^2 \ell^2}{4}} \right)^{3/2} - 1$$

This may be rewritten to show the position error  $\delta$  which will give an error  $\epsilon$ .

$$(2-21) \quad \delta = \sqrt{\left(\frac{1}{1+\epsilon}\right)^{2/3} R^2 + \frac{l^2}{4} \left(\frac{1}{1+\epsilon}\right)^{2/3} - (1+\gamma)^2} - R$$

Figure 2-8 is a graph of equation 2-21 with zero uncertainty in magnet length. This shows the permissible error in probe placement which will cause a +5% error in dipole moment when the magnet length is known precisely. The significant feature in figure 2-8 is the variation of position tolerance with separation. If the probe is placed close to the magnet to obtain a large field, the tolerance on probe position virtually disappears.

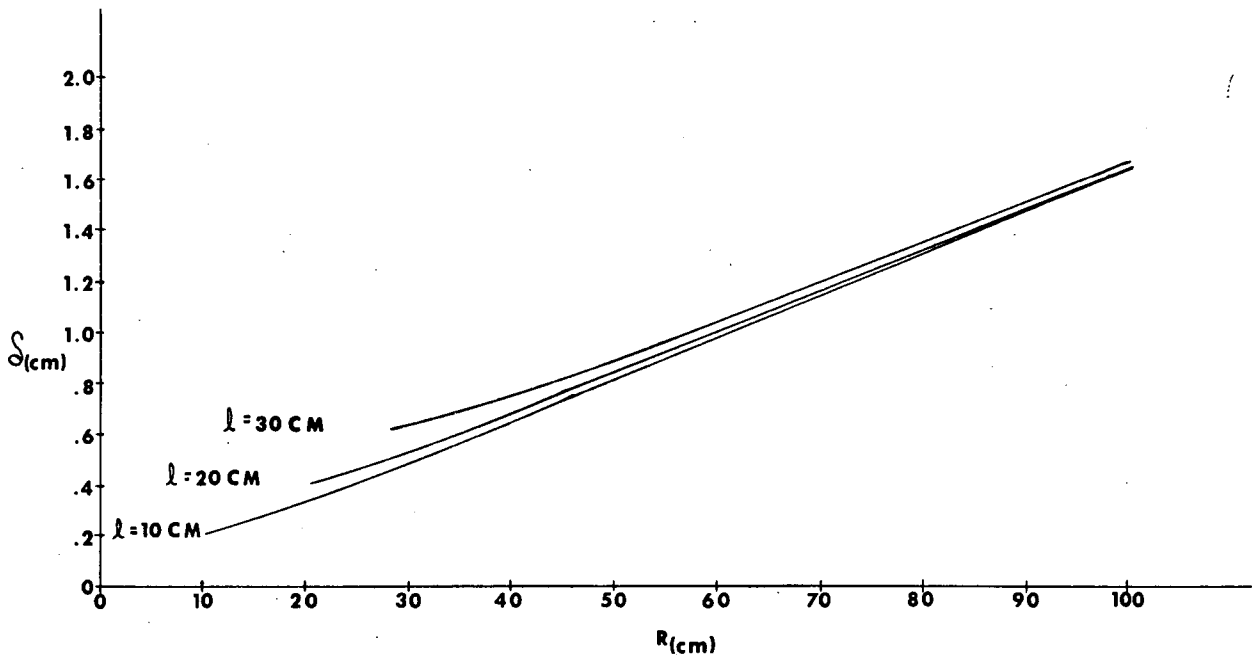


Figure 2-8 Probe Position Error to Give 5% Error in Moment Determination

Figure 2-9 shows the tolerance on probe position to give +5% error in dipole moment when the effective magnet length has been estimated 10% too long. This amount of error in magnet length will give an error of 5% in moment for separation of 1.16 magnet lengths, so the position must be exact to obtain 5% accuracy at this separation and it is no longer possible to obtain 5% accuracy for measurement distance less than 1.16 magnet lengths.

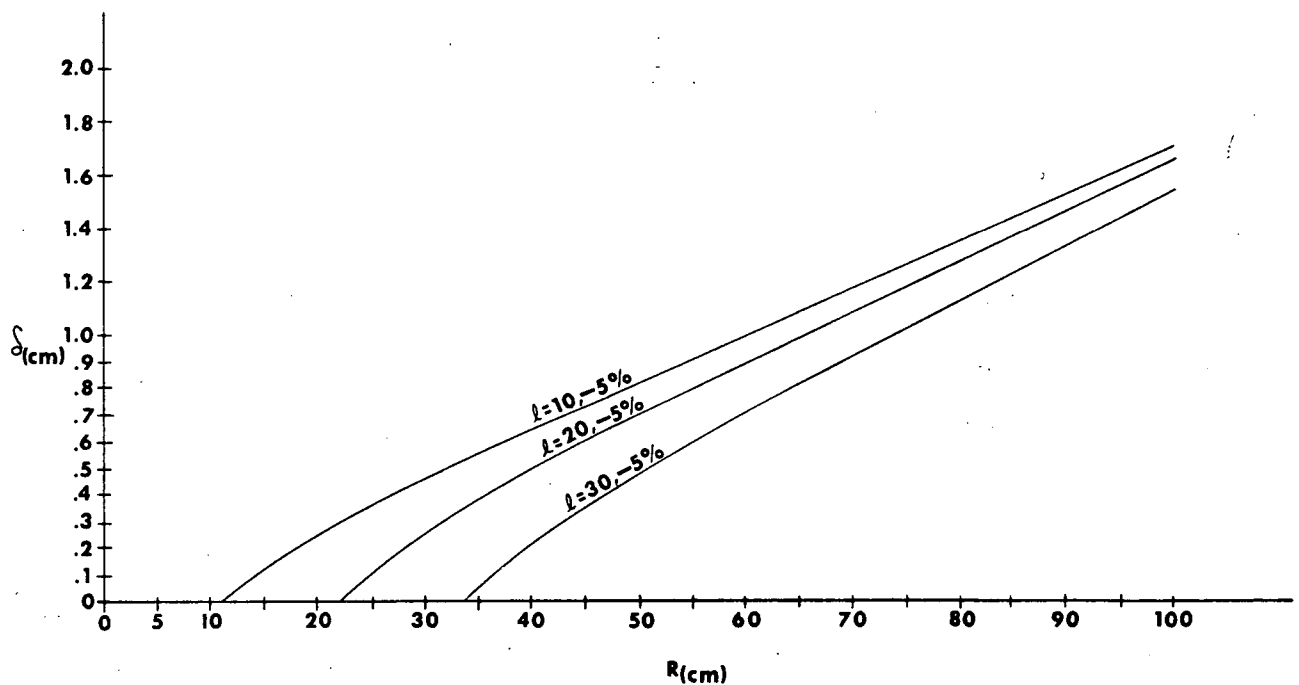


Figure 2-9 Probe Position Error to Give 5%  
Error in Moment Determination  
Magnet Length is 10% in error.



## 2.5 Quadrupole Effects

In this section we estimate the effect of non-uniform flux distribution on the field strength due to a bar magnet.

Let us approximate a magnet with the array of equal charges as shown in Figure 2-10.

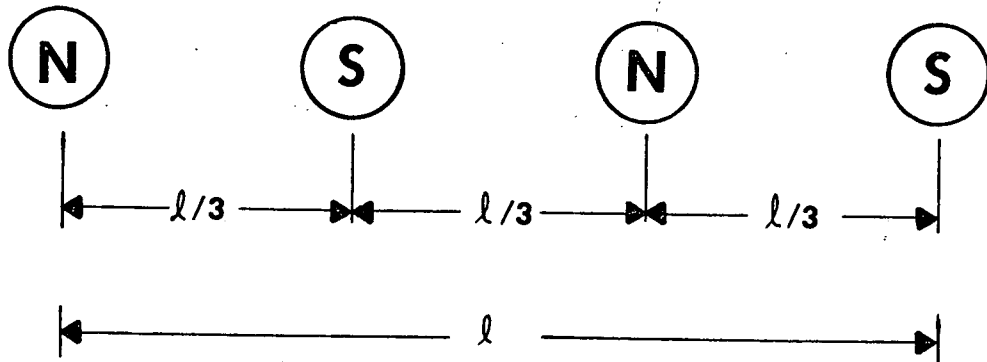


Figure 2-10 Point Charge Approximation to Bar Magnet

This arrangement of charges may be considered as two dipoles superimposed - the dipole formed by the outer pair of charges form a dipole of moment  $m\bar{l}$ , and the inner pair of charges form a dipole of opposite sense and moment  $\frac{m\bar{l}}{3}$ . The net moment is then  $\frac{2}{3} m\bar{l}$ .

The magnetic field due to this arrangement of charges is simply the sum of the contributions by the inner dipole and the outer dipole. A measurement made as in figure 2-7 will indicate a field given by

$$(2-22) \quad H = \frac{m\bar{l}}{(R^2 + \frac{\bar{l}^2}{4})^{3/2}} - \frac{m\bar{l}/3}{(R^2 + \frac{\bar{l}^2}{36})^{3/2}}$$

The relative error in determining the magnetic moment from 2-19 is then

$$(2-23) \quad \epsilon = \frac{1}{2} \left[ 1 - \left( \frac{\frac{R^2}{\ell^2} + \frac{1}{4}}{\frac{R^2}{\ell^2} + \frac{1}{36}} \right)^{3/2} \right]$$

which is a function of distance relative to the magnet length rather than a function of absolute distance.

Returning to equations 2-22, notice that the variation of error with distance will disappear if the inner and outer dipoles have the same length. Quite obviously the worst variation with distance occurs with a very short inner dipole. Taking an infinitesimal dipole -- again with half the moment of the outer dipole -- the error in calculating the dipole moment from equation 2-19 will be given by

$$(2-24) \quad \epsilon = \frac{1}{2} \left[ 1 - \left( 1 + \frac{\ell^2}{4R^2} \right)^{3/2} \right]$$

which is also a function of relative distance.

Figure 2-11 shows the variation of error with distance for these two cases. Both of these assume an inner dipole with moment equal to half the net moment. The case of an infinitesimal dipole is the limiting case for the relative dipole strengths considered. For either case, the error is less than 5% for measurement distance greater than two magnet lengths.

In view of the uncertainty in effective magnet length, the selected measurement distance should be as great as allowed by equipment sensitivity and by interference from the magnetic environment.

## 2.6 Characteristics of Magnetic Materials

The origin of magnetic effects in materials lies in atomic dipoles formed by electronic circulation and spin. Classical forces tend to align the atomic dipoles in opposition to an applied magnetic field, but quantum mechanical exchange forces tend to cause the dipoles to align in an aiding orientation. The net result is that the quantum mechanical forces dominate for small groups of atoms which will be aligned aiding, but classical forces will limit the size of these domains to about  $10^{-6} \text{ cm}^3$  to  $10^{-2} \text{ cm}^3$ . Macroscopic effects then, are due to the actions of these microscopic domains.

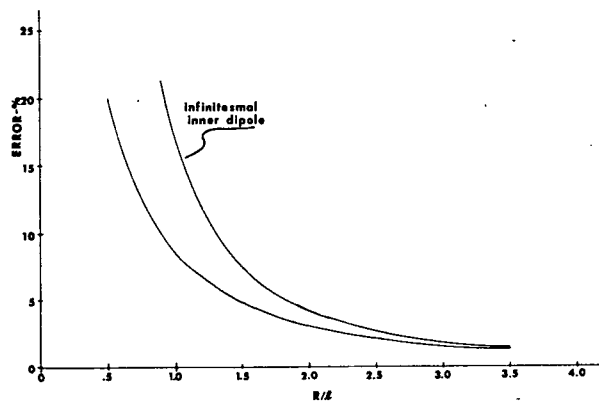


Figure 2-11 Error in Determining Dipole Moment Due to Quadrupole Effects

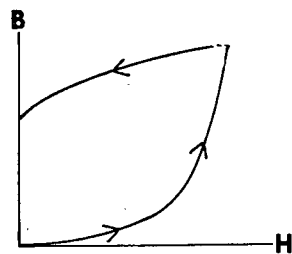


FIG. 2-12 A

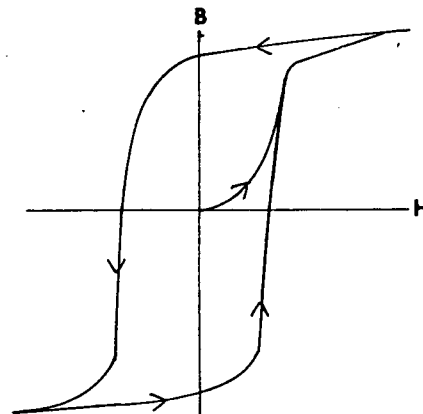


FIG. 2-12 B

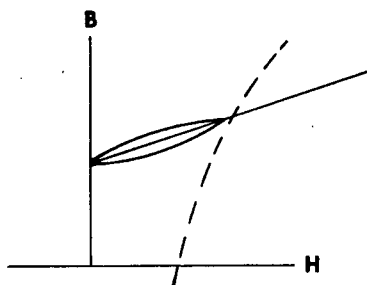


FIG. 2-12 C

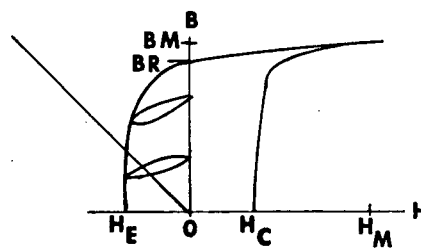


FIG. 2-12 D

Figure 2-12 Typical B-H Trajectories

The two outstanding features that one notices in magnetic materials are explainable in terms of magnetic domains. First is the saturation of the material which occurs when all the atomic dipoles are forced into alignment with the field. Because magnetic effects are due to the orientation of atomic dipoles, the intensity will not increase past the point where the magnetizing force causes complete alignment of all the atomic dipoles.

The other outstanding feature is the manner in which magnetization changes with applied field. When a magnetizing field is first applied to magnetic material, the domains deform elastically. Then as the field is increased, the domains in a favorable orientation begin to grow at the expense of less favorably oriented domains, and this process continues until either the magnetizing field no longer increases or until the material is saturated. This action of elastic deformation alternating with domain growth gives rise to a multiple valued curve of magnetic intensity vs magnetizing field as the field is cycled between some minimum and maximum values.

When a field is applied to a specimen the magnetization will begin to increase which will cause the magnetization to increase more rapidly (Figure 2-12A). As the applied field is then reduced, not all of the domains will return to their original (random) orientations giving rise to residual magnetization. This effect is sketched in Figures 2-12A and 2-12B which shows the characteristic shape of the hysteresis loop.

Figure 2-12C shows a minor hysteresis loop which occurs when the applied magnetizing field is cycled between zero and a value which does not result in domain growth. The average slope of this loop is very constant even for quite large values of magnetization. This average slope on a graph of induction vs applied field (see equation 6) is termed recoil permeability with symbol  $\mu_r$ . The recoil permeability can be assumed to decrease about 20% with peak magnetization of 90% of saturation.

Figure 2-12D shows a typical B-H curve shape with several recoil loops. Notice the terminology:  $B_m$  - maximum induction;  $H_m$  - magnetizing force;  $B_r$  - residual induction;  $H_c$  - coercive force.

From the preceding, we can identify several desirable characteristics for permanent magnets: the B-H curve of the material should intersect the load line at as high an induction as possible in order to minimize the mass of the magnet; the maximum required magnetizing force should be low to minimize coil requirements; a long slender magnet should be used to give as great a load line slope as possible; and the coercive force should be sufficiently high to minimize external demagnetizing effects.

## REFERENCES

- 1 Adler, R. B., Longini, R. L., and Smith, A. C.: Introduction to Semiconductor Physics. John Wiley & Sons, N.Y., 1964, page 55. Analysis of Hall Effect in Semiconductors.
- 2 Bozorth, R. M.: Ferro magnetism. D. Van Nostrand Co., Princeton, N.J., 1968. Fundamentals of magnetism are discussed in chapter 1, and pages 838-849; permanent magnet materials are discussed in chapters 2 and 9; and environmental effects on permanent magnets are discussed on pages 354-358.
- 3 Dummer, G. W. A.: Materials for Conductive and Resistive Functions. Hayden Book Co., N.Y., 1970. Characteristics of magnet wire are covered on pages 68-78.
- 4 Hudson, E. C.: Patent No. 3,389,230 - Semiconductor Magnetic Transducer. U.S. Patent Office, Washington, D.C., 1968.
- 5 Kroon, D. J.: Electromagnets. Boston Technical Publishers, Cambridge, Mass., 1968. Magnetic fundamentals are discussed in Chapter 2.
- 6 Montgomery, D. B.: Solenoid Magnet Design. Wiley-Interscience, N.Y., 1969. Choice between copper and aluminum conductor is explained in section 1.5, and the spatial distribution of the magnetic field due to a solenoid is calculated in Chapter 8.
- 7 Moser, H.: Magnetic Diodes AHY10 and their Application. AEG Telefunken Corp. application report explains the operation of a polarity sensitive magnetoresistor.
- 8 Parker, R. J. and Studders, R. J.: Permanent Magnets and Their Application. John Wiley and Sons, N.Y., 1962.
- 9 Pugh, E. M., and Pugh, E. W.: Principles of Electricity and Magnetism. Addison-Wesley, Reading, Mass., 1970.
- 10 Tenzer, R. K.: Technical Documentary Report No. ASD-TDR-63-500 Temperature Effects on the Remanence of Permanent Magnets. Air Force Systems Command, Wright-Patterson Air Force Base, Ohio, 1963.

### 3.0 THE MAGNETIC CORE

#### 3.1 Materials

The primary criteria for selecting the magnetic core material are those characteristics that result in a minimum weight system. Materials suited to use in variable magnetic moment applications are alloys with density very near 8 grams/cm<sup>3</sup>.-- and a 10% variation is unusual. Thus material density is not a significant factor.

With a choice of materials which have essentially the same mass density, the core material which gives minimum weight is the one with greatest residual induction at the desired operating point. This can be shown by combining equations 2-5 and 2-6 to give

$$(3-25) \quad \text{volume} = 4\pi \frac{M}{B-H}$$

which indicates that the minimum volume magnetic core is one with maximum induction.

The residual induction at the operating point is determined by both the B-H characteristics of the material and by self demagnetization due to core geometry (see next section). If we assume that the slenderness ratios of concern are greater than 20 and the residual induction is on the order of 10,000 gauss, then the self demagnetizing force is in the tens of oersteds. This indicates that the optimum material has maximum residual induction at a demagnetizing force of a few tens of oersteds - but the coil requirements should be borne in mind. If a material is selected with large residual induction but requires a very large magnetizing force, then the penalty in coil weight may be very large.

The core material which gives a minimum weight combines minimum coercive force and maximum induction at a demagnetizing field of a few tens of oersteds.

Several secondary considerations should be borne in mind when evaluating alternative core materials -- considerations such as available size, special treatment required and mechanical properties.

Most of the useful core materials must be cold worked to develop their magnetic properties, with a 95% reduction in area being typical. Because of this requirement, some materials are only available in thin strip form or small diameter wire. These materials also require annealing at approximately 600°C and must not be deformed after heat treatment.

A survey of 60 companies was conducted, and the three most likely materials for this application were selected. Remendur 38, P6 Alloy and Vicalloy I were selected for maximum induction over three ranges of demagnetizing fields. Remendur 38 has the largest residual induction of these three materials for demagnetizing fields less than 35 oersteds, while P6 Alloy has the greatest residual induction for demagnetizing fields from 35 to 55 oersteds, and Vicalloy I extends the range to 100 oersteds. The properties of these materials are summarized in Table 3-1, and the demagnetization curves are shown in figure 3-1.

The choice of material for the magnetic core cannot be made without considering the effects of self demagnetization, and the requirements placed on the magnetizing coil by the choice of core material.

### 3.2 Geometry Effects

As pointed out in 2.2, a permanent magnet has a self-demagnetizing field which depends both on the geometry and on the level of induction.

The effect of self-demagnetization is to increase the volume of core material required to achieve a given moment. This will also increase the coil requirements because the magnetizing coil will enclose the volume of core material, so a large core will require a large magnetizing coil.

It is convenient to compare core materials graphically by superimposing contours of constant residual moment per cubed length ( $M/\ell^3$ ) on the B-H curves of the materials. This is possible because equation 2-10 provides a link between the slenderness ratio ( $\ell/D$ ) and the B-H coordinates, while equations 2-5 and 2-6 provide a link between residual induction, core volume, and dipole moment.

Combining 2-5, 2-6 and 2-10 we obtain

$$(3-26) \quad B = 1.024 \times 10^{-4} \frac{p^2}{a} \frac{H^4}{\left(\frac{M}{\ell^3}\right)^3}$$



Table 3-1

	Remdender 38	P6 Alloy	Vicalloy	
Residual Induction ( $B_r$ )	16,500 (min.)	14,000	8,400	Gauss
Coercive Force ( $H_c$ )	$38 \pm 10\%$	$58 \pm 10\%$	240	Oersteds
Magnetizing Force ( $H_m$ )	100	250	1000	Oersteds
$\frac{H_m}{H_c}$	2.6	4.3	4.2	
Fullness $\frac{(BH)_{\max}}{B_r H_c}$	.6	.61	.44	
Density ( $\rho$ )	8.2	8.16	8.2	grams/cm <sup>3</sup>

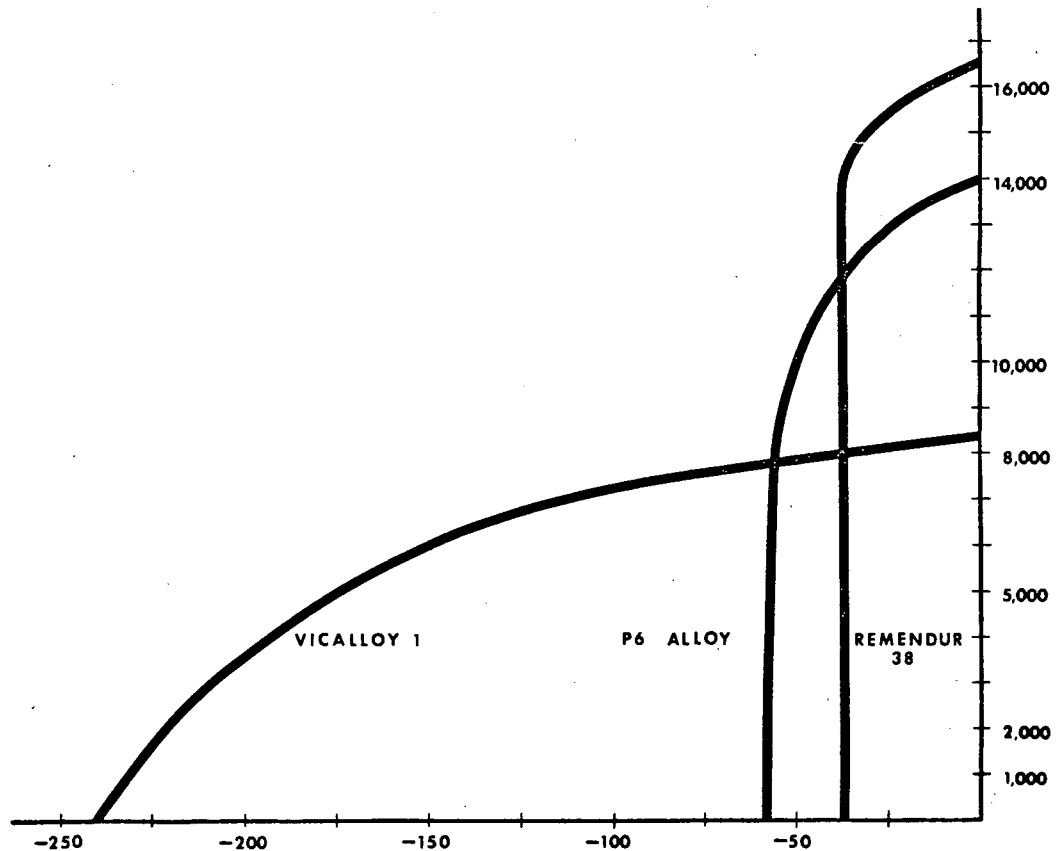


Figure 3-1 Demagnetization Curves for Selected Materials

On substitution of appropriate geometry factors, this becomes

$$(3-27) \quad B = 1.63 \times 10^{-3} \frac{H^4}{\left(\frac{M}{l^3}\right)^3} \quad \text{for a square core cross section}$$

$$(3-28) \quad B = 1.287 \times 10^{-3} \frac{H^4}{\left(\frac{M}{l^3}\right)^3} \quad \text{for a round core cross section}$$

Figure 3-2 shows the B-H curves of 3 materials superimposed on contours of constant  $M/l^3$  from equation 3-27. These curves facilitate the inclusion of self-demagnetization effects when comparing core materials.

To illustrate the use of these curves, assume that a 10,000 p-cm magnet is desired with a maximum core length of 25.4 cm (10 inches). The ratio  $M/l^3$  for this case is .61, so we follow the  $M/l^3 = .6$  contour in figure 3-2 to find that Vicalloy I will require the largest core volume with a residual induction of 8100 gauss, P6 alloy will require an intermediate volume with 11,900 gauss and Remendur 38 will require the smallest volume @ 13,600 gauss. The minimum weight core for this example would be Remendur 38.

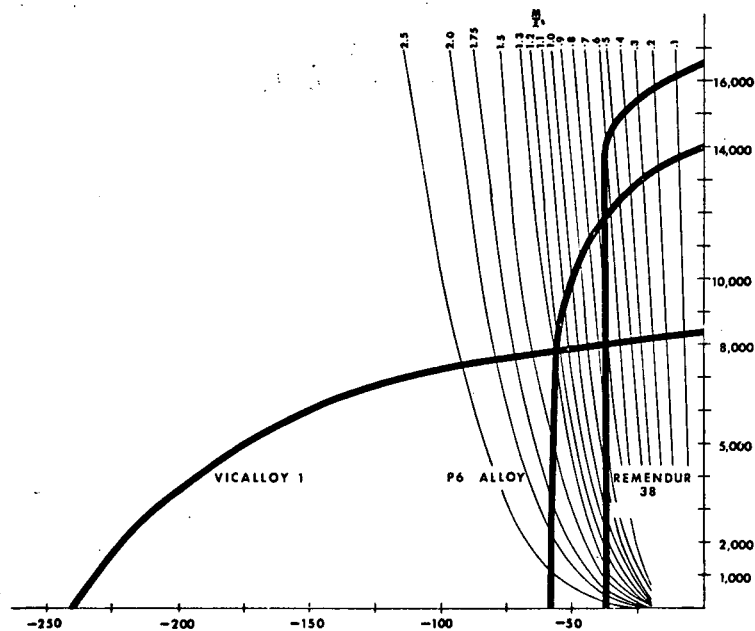


Figure 3-2

### 3.3 Interaction with Magnetizing Coil

The core design will affect the coil requirements in two ways: first, through the relationship between core and coil geometru; and second, by establishing the requirements on magnetizing force.

The core volume will determine the volume which must be supplied with a relatively uniform magnetizing force, so the size and shape of the core will obviously affect the volume of the magnetizing coil which enclose the core. Increasing core length will require more wire to cover the coil, while increasing core diameter will increase the average length of a turn. The magnetizing force which must be supplied by the magnetizing coil consists of the magnetizing force required to overcome self-demagnetizing effects and the net magnetizing force required to saturate the magnet. Once the material and required moment are specified, the total required magnetizing force will be a function of the slenderness ratio.

The interaction between peak coil power, coil weight and magnetizing force is seen by referring to figure 3-3. This figure shows the shape of the coil weight vs. peak coil power curve for a magnetic core of fixed size and material. The form of the equation plotted in Figure 3-3 is

$$\text{coil weight} = \frac{\frac{P}{H^2} C_2}{2 - \frac{P}{H^2} C_2 + C_3}$$

where P is peak power, H is peak magnetizing force and the C's are constants (see section 5.2).

Figure 3-3 shows that there is a threshold coil power for a given core design. Below this minimum coil power, it is not possible to design a coil which will magnetize the core. At large coil power the coil weight can be traded one for one with peak coil power, but at low coil power the increased coil build causes the coil weight to blow up.

Notice also that for a given coil design the peak power varies with the square of the magnetizing force. If the magnetic core is replaced with a material with twice the required magnetizing force, then the same magnetizing coil may be used but the required peak power will increase by a factor of four.

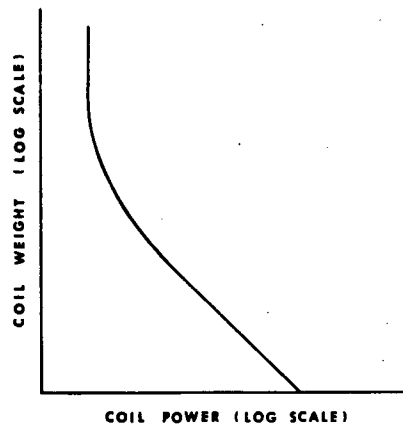


Figure 3-3 Coil Weight vs Peak Power

### 3.4 Scaling

Scaling of magnet designs is useful when it is desired to produce a different magnet size from a given design or when it is desired to evaluate a new design which is an inconvenient size.

It is evident that if a magnet made of homogeneous material has its dimensions scaled by a scale factor  $s$ , then the maximum induction and magnetizing force will remain constant. This is consistent with equation 2-10 which says that self-demagnetization effects depend only on shape and are independent of size.

The spatial variation of magnetic field will have the same shape, but measurement distances must be scaled.

This is consistent with the scaling of all distances and lineal dimensions.

The effective pole separation (effective magnet length) will be scaled by  $s$ , but the effective pole strength will be scaled by  $s^2$ . This comes about because the pole strength is proportional to the cross sectional area of the magnet rather than to the volume of magnetic material.

Finally, the volume and weight of the material, the dipole moment, and the energy required to magnetize the material will all be scaled by  $s^3$  -- which is what would be intuitively expected.

Summarizing these scale factors, we find that:  
all dimensions and distances are scaled by  $s$ ; volume,  
weight, and moment are scaled by  $s^3$ ; and pole  
strength is scaled by  $s^2$ .


**DESCRIPTION:**

P-6 Alloy combines the advantages of a high hysteresis loss and low magnetizing force into one magnetic material. These two important features plus high residual induction and high permeability make P-6 Alloy especially useful for hysteresis motor applications.

This material is supplied in strip or wire form. The strip material is available in widths up to 4.0 inches and thicknesses from .005" to .100". Wire may be obtained in diameters ranging from .005" to .100". Magnetic certification is furnished with each shipment of material.

**CHARACTERISTICS:**
**A. Composition:**

Nickel	6.0%
Vanadium	4.5%
Iron	44.5%
Cobalt	45.0%

**B. Magnetic Properties \*(D.C.):**

Maximum permeability	285
Peak magnetizing force, oersteds	250
Maximum induction, gauss	16,000
Residual induction, gauss	14,000
Maximum energy product ( $B_d H_d$ ), gauss oersteds	550,000
Coercive force, oersteds	60
Hysteresis loss, joules/in <sup>3</sup> /cycle	.37
peak H = 180 ampere turns/inch	$\lambda = .655$

\* At 25°C after age-hardening

**C. Physical Properties:**

Hardness prior to age-hardening	40 R.C.
Hardness after age-hardening	65 R.C.
Specific gravity	8.16
Density, lbs./cu. in.	0.285
Electrical resistivity, microhms-cm	30
Coefficient of expansion, in./in./°C	$11.1 \times 10^6$

**HEAT TREATMENT:**

After stamping or coiling to the desired form, the material should be either vapor degreased or emulsion cleaned prior to final age-hardening heat treatment. The material should then be placed in an electric furnace with hydrogen or cracked gas atmospheres and held at 600°C for two hours. This final heat treatment is necessary to obtain the desired magnetic characteristics of the material.

**DESIGN CONSIDERATIONS:**
**A. General:**

P-6 Alloy is capable of supplying superior hysteresis characteristics in designs where a maximum of 100 oersteds magnetizing force is available.

The high aging temperature of P-6 alloy allows it to be subjected to a much higher operating temperature than the chrome, tungsten and cobalt magnet steels without resulting in subsequent aging. The material is magnetostrictive, however, and laminations should therefore be stacked and contained with a minimum of stress applied to the material. Figures 1, 2 and 3 respectively show the hysteresis loop, energy product and magnetization curves; the hysteresis loss vs. maximum flux density; and the hysteresis loss vs. magnetizing force for fully aged P-6 Alloy.



GENERAL ELECTRIC PERMANENT MAGNETS • THERMISTORS • THYRITE® VARISTORS

PRECEDING PAGE BLANK NOT FILMED

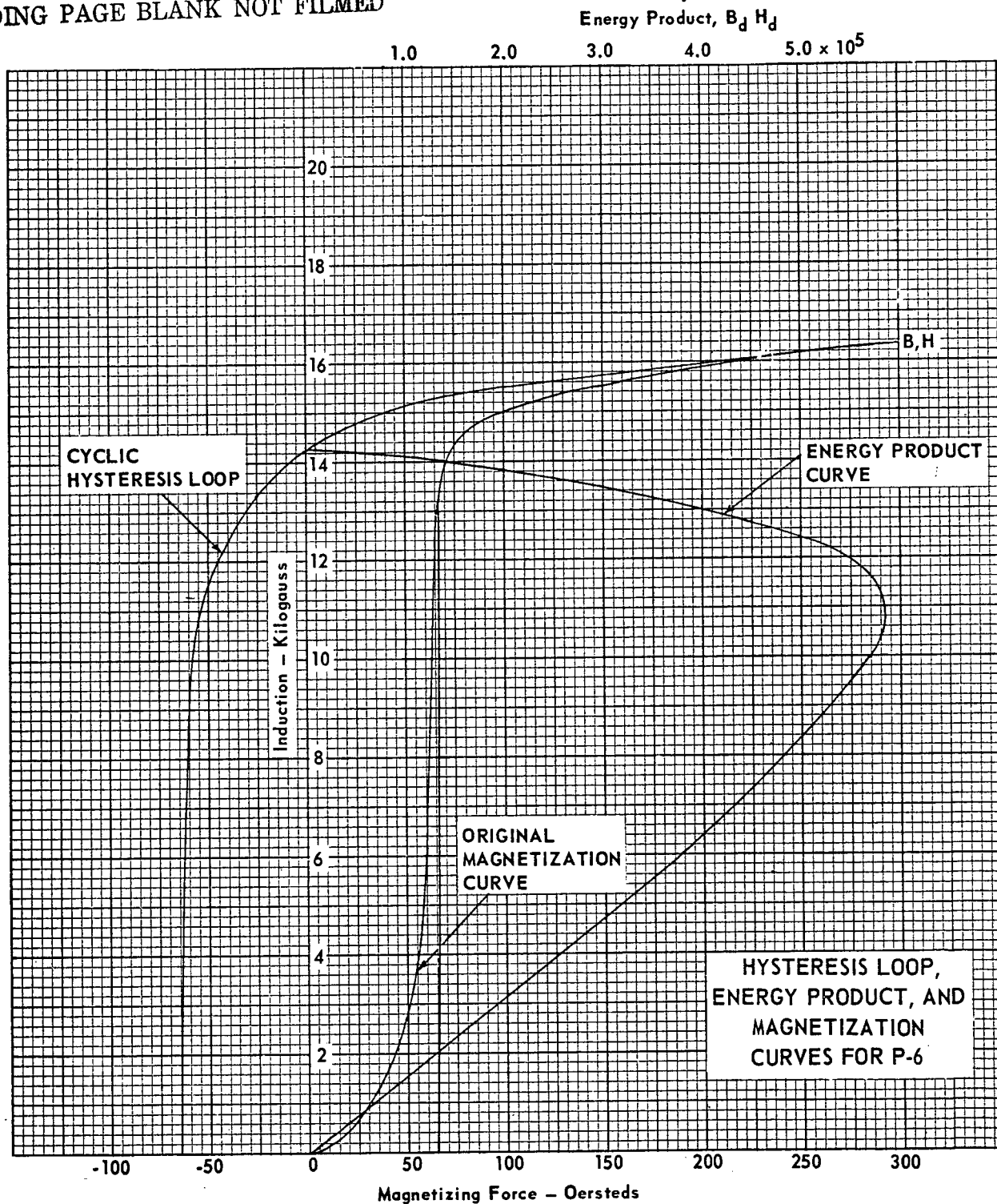


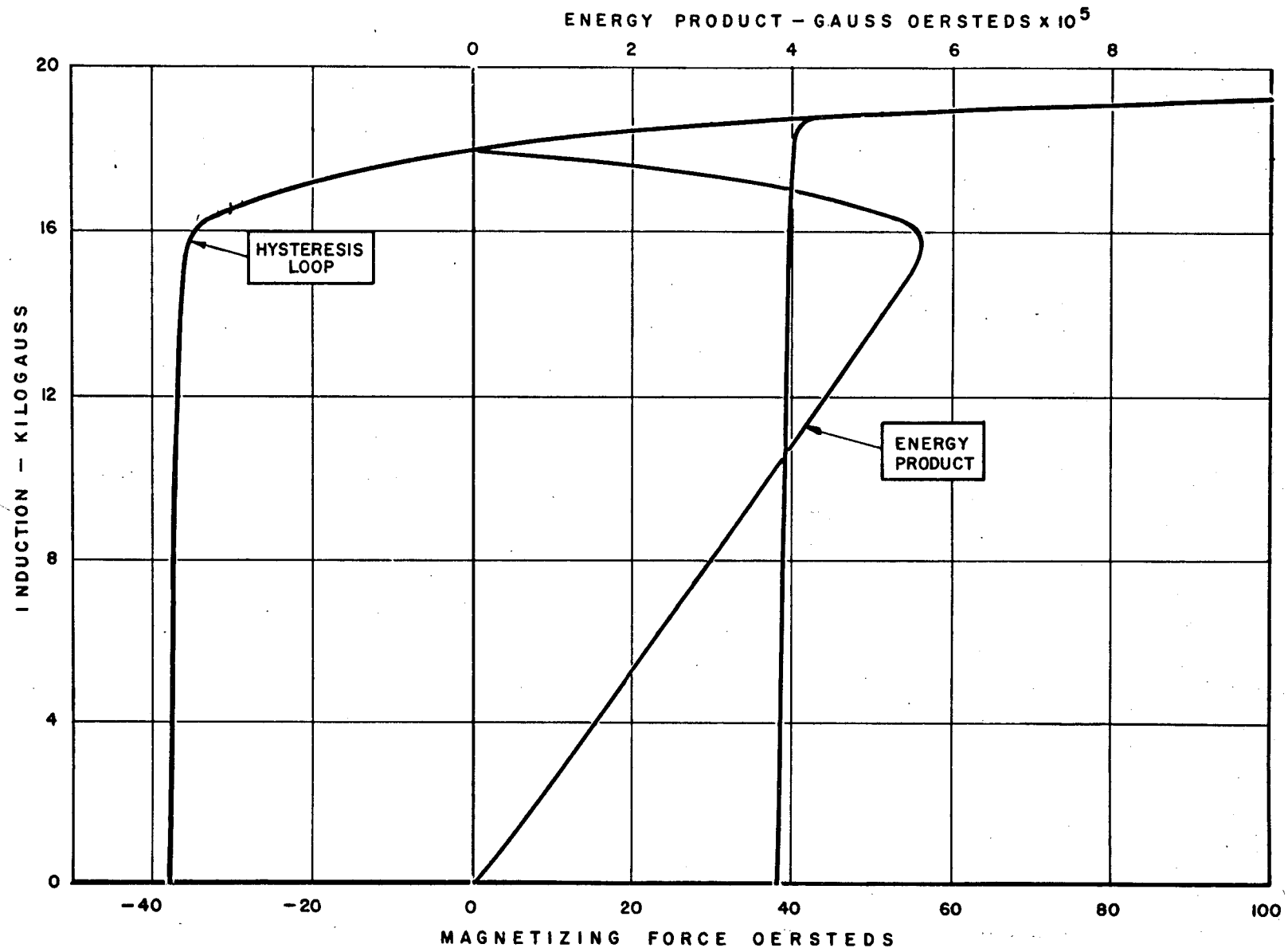
FIGURE 1

MAGNETIC MATERIALS BUSINESS SECTION

GENERAL  ELECTRIC

EDMORE, MICHIGAN

Typical Hysteresis Loop and Energy Product for Remendur 38 Heat Treated at 1100 F for 2 Hours.



4 of 5 blank, NOT FILMED



#### 4.0 MAGNETIZING COIL WEIGHT

In this section we treat the problem of determining the wire weight for a magnetizing coil.

##### 4.1 Derivation of Coil Weight Equations

The resistance of a length of wire in terms of its resistivity and dimensions is given by

$$(4-29) \quad R = \frac{4l_w \rho}{\pi d^2}$$

or the resistance for a specific size and material is given by

$$(4-30) \quad R = r l_w$$

where  $r$  is lineal resistivity - e.g. resistance per thousand feet of wire length. Similarly, the weight of a length of wire in terms of wire dimensions and density is given by

$$(4-31) \quad W_w = l_w \frac{\pi d^2}{4} \delta_w$$

or an expression similar to 4-30 can be written for wire weight.

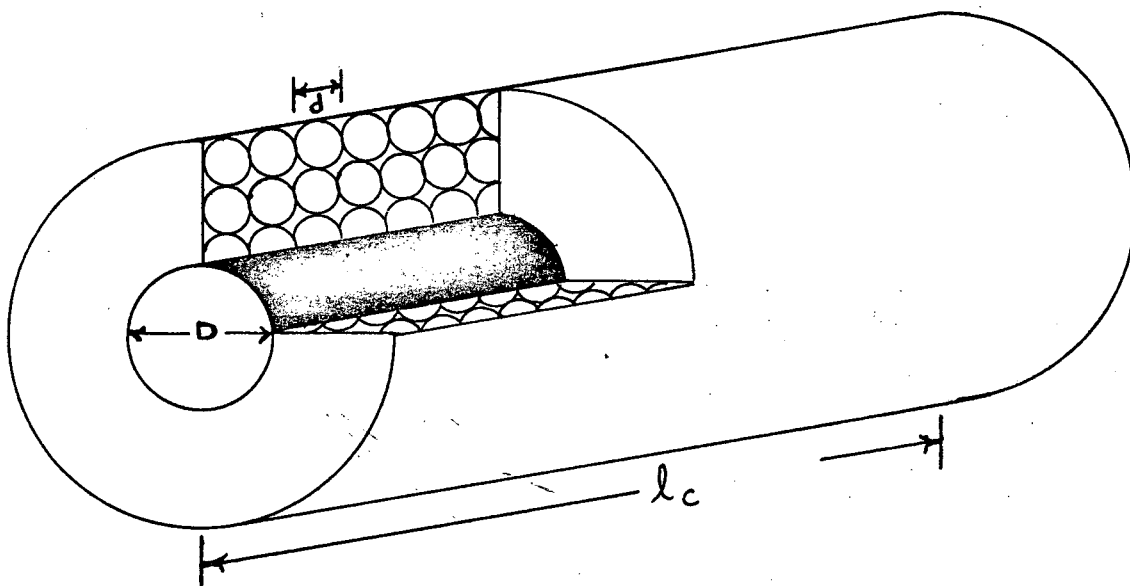


Figure 4-1 Coil Dimensions

The length of wire required to wind a coil as shown in Figure 4-1 can be approximated in three steps. The first order approximation is that wire length equals the product of the perimeter of the cross section and the number of turns.

$$(4-32) \quad \ell_w = (pD) n$$

The second order approximation corrects for the effect of coil build - i.e., for multilayer construction. Because alternate coil layers will have opposite pitch, the diameter of the coil will increase by two wire diameters for each additional layer of wire. The length of one turn in the  $j$ th layer will then be

$$(pD) + 2\pi d \left(j - \frac{1}{2}\right)$$

and the length of all turns in  $\lambda$  layers is approximately

$$(4-33) \quad \ell_w = n (pD) \left[1 + \frac{\pi}{p} \frac{\lambda d}{D}\right]$$

It is of value to note that  $(\pi/p)$  is nearly 1, so the second term in the brackets is nearly the ratio of coil build to coil diameter.

The next refinement is very rarely needed unless the wire diameter approaches the core diameter. The additional wire length due to the pitch of the winding is simply the length of the coil multiplied by the number of coil layers. The expression for the length of wire in a coil of  $\lambda$  layers is

$$(4-34) \quad \ell_w = n (pD) \left[1 + \frac{\pi}{p} \frac{\lambda d}{D}\right] + \lambda \ell_c$$

This has been found to give  $\pm 1\%$  accuracy for carefully wound coils. From this we can compare the amount of wire used for different cross-sectional shapes. For instance, consider two cores with equal cross sectional area. One having square cross section with side  $w$ , and the other being circular with diameter  $D$ .

For the square:

$$L_{w1} = 4nw + n\pi\lambda d$$

For the circle:

$$L_{w2} = nD + n\pi\lambda d$$

Invoking the equal area constraint we have for the ratio of the wire lengths

$$\frac{L_{w1}}{L_{w2}} = \frac{\frac{4}{\pi} \sqrt{\frac{A}{d^2}} + \lambda}{\sqrt{\frac{4A}{\pi d^2}} + \lambda}$$

This ratio is plotted vs  $(A/d^2)$  with  $\lambda$  as a parameter in the graph of Figure 4-2. This shows that the penalty for using a core with square core cross section rather than a round cross section varies from 13% when a single layer of fine wire is wound on a large core to 26% when many layers of heavy wire are wound on a small core.

Included in the figure is a nomograph to convert cross sectional area and wire gauge to  $(A/d^2)$ . The nomograph assumes double formvar insulation, so the diameter used when constructing the nomograph was greater than the bare wire diameter listed in wire tables.

The use of the nomograph is illustrated by taking a core with 0.5 square inch cross sectional area with 10 layers of 24 AWG. The intersection of the 24 AWG line and the 0.5 in<sup>2</sup> line gives an  $(A/d^2)$  of 1005. Following the  $(A/d^2)$  line down to the 10 layer curve, we find the length ratio is 1.160. For this example 16% more wire is needed for a square cross section than for a circular cross section of equal area.

Figure 4-3 facilitates comparison of wire length with circular cross sections when only the wire diameter and the number of layers is changed. If the same core is used, then the periphery ( $\pi D$ ) will not change and if the number of turns is also constant, then the relative wire length is

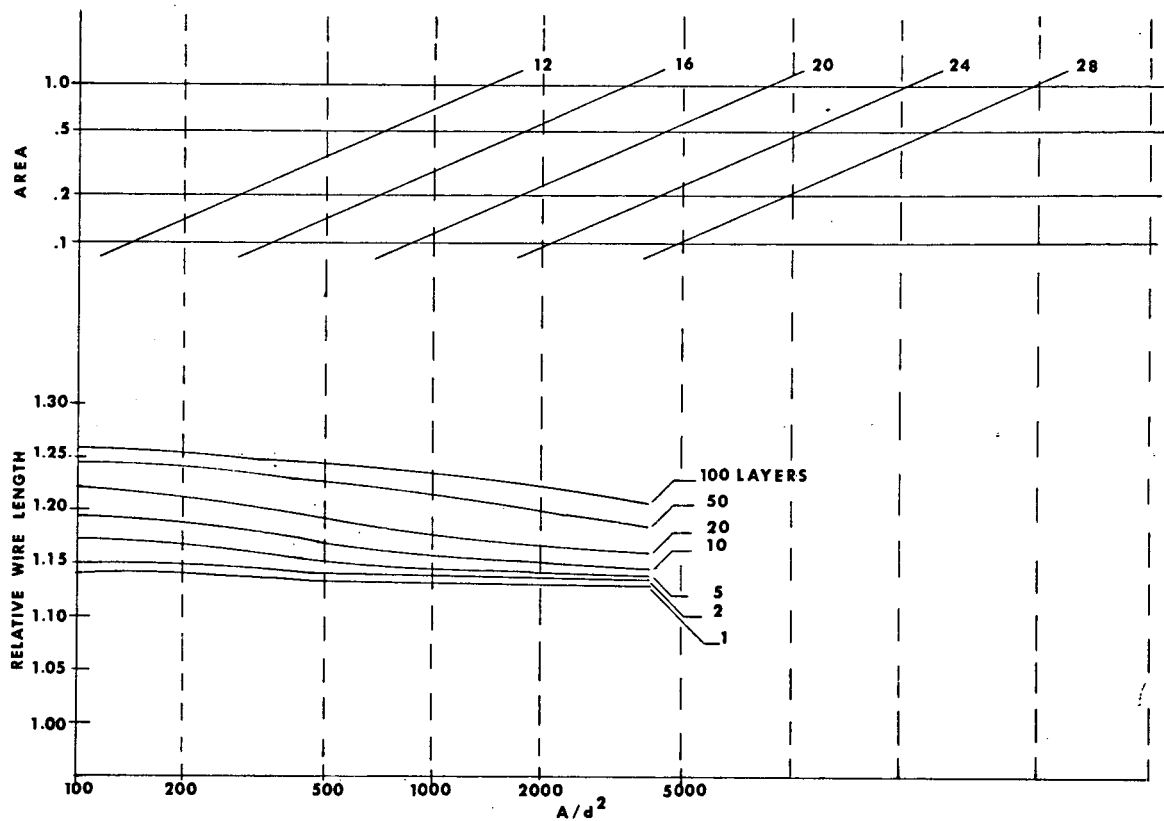


Fig. 4-2 Wire length for Square Core Relative to Wire length for a Circular Core

$$(4-36) \quad \frac{l_w}{npD} = 1 + \frac{\lambda d}{D}$$

from equation 4-33.

To illustrate the use of Figure 4-3, assume that a coil is to be designed with 1000 turns of copper wire and  $5\Omega$  resistance on an 8 inch long by .5 inch diameter round core.

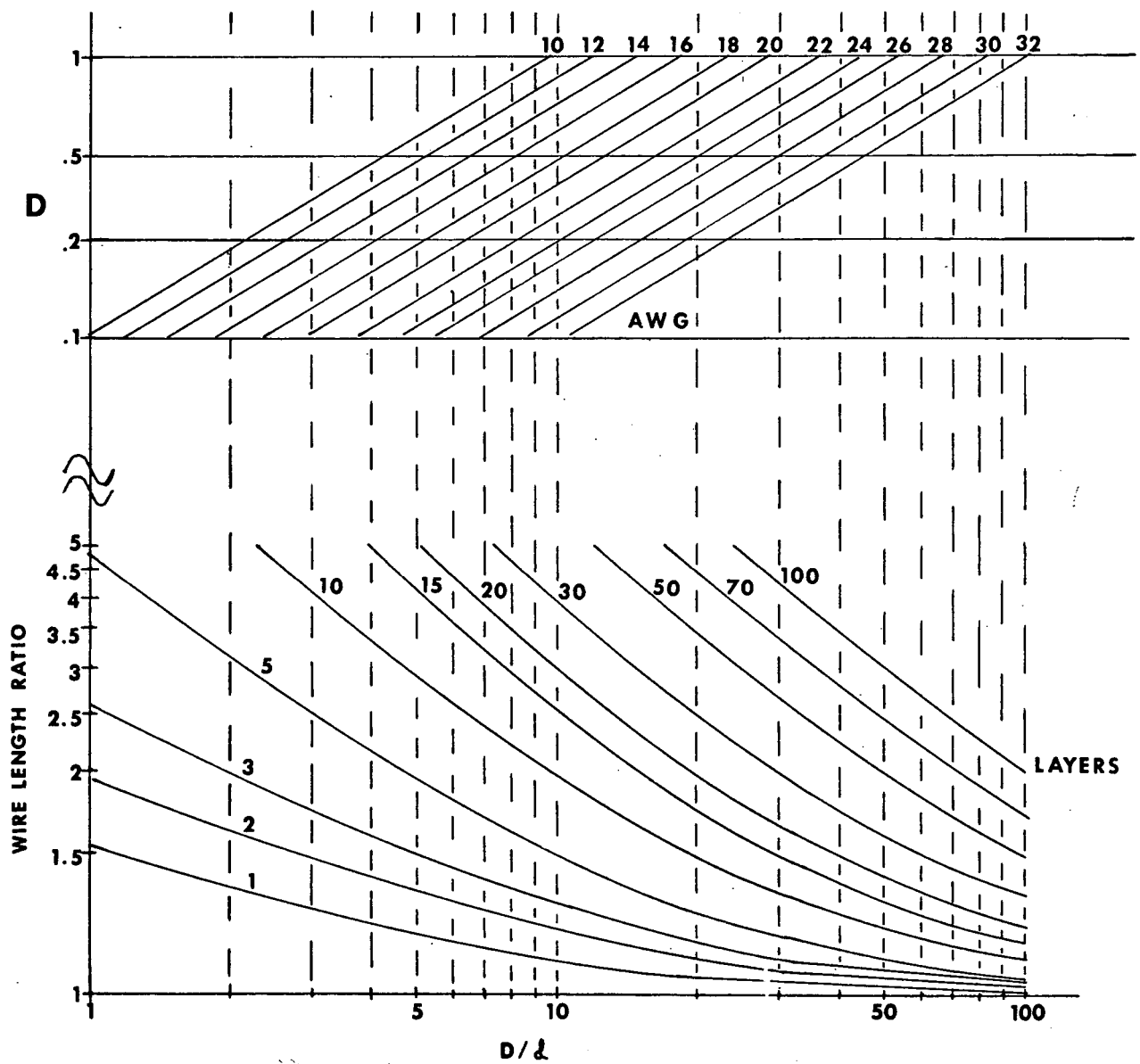


Fig. 4-3 Effect of Coil Build on Wire Length

WIRE TABLE

<u>AWG</u>	<u>Diameter in Inches</u>		<u>Ohms per 1000 feet</u>	
	<u>Bare</u>	<u>Double Formvar</u>	<u>Aluminum</u>	<u>Copper</u>
10	.1019	.1055	1.637	.9989
12	.0808	.0842	2.603	1.588
14	.0641	.0673	4.139	2.525
16	.0508	.0538	6.584	4.016
18	.0403	.0431	10.47	6.385
20	.0320	.0346	16.64	10.15
22	.0253	.0277	26.46	16.14
24	.0201	.0223	42.08	25.67
26	.0159	.0179	66.90	40.81
28	.0126	.0145	106.4	64.90
30	.0100	.0116	169.2	103.2
32	.0080	.0094	269.0	164.1

TABLE 4-1

The periphery of the core is 1.57 inches ( $.5\pi$ ), so 1000 turns will require at least 1570 inches or 131 feet.

The lineal resistivity is then on the order of  $5\Omega$  per 131 feet or  $38\Omega$  per 1000 feet. As we expect to use more than 131 feet of wire because of coil build, we look up the wire size with a slightly lower lineal resistivity in Table 4-1 and find 24 AWG with  $25.67\Omega$  per 1000 feet.

Next we approximate the number of layers by taking the length of a single layer coil (number of turns multiplied by wire diameter) and divide by the desired coil length.

$$\lambda \approx \frac{1000 \text{ turns} \times .0223 \text{ inch/turn}}{8 \text{ inch}}$$

$$\lambda \approx 2.8$$

With the preliminaries completed, we use the wire nomograph at the top of figure 4-3 to find that (D/d) for a .5 inch diameter core and #24 AWG is 22.4.

Next, enter figure 4-3 at (D/d) = 22.4 and 3 layers. The wire length ratio is 1.13, so the wire length is

$$l_w = 1.13 \times 131 \text{ feet}$$

$$l_w = 147 \text{ feet}$$

and the resistance of the coil is

$$R_c = 147 \text{ feet} \times 25.67\Omega/1000 \text{ feet}$$

$$R_c = 3.77\Omega$$

If this coil is wound with full layers rather than allowing the last layer to partially cover the coil, then the coil length will be

$$l_c = \frac{1000 \text{ turns} \times .0223 \text{ inch/turn}}{3 \text{ layers}}$$

$$l_c = 7.43 \text{ inch/layer}$$

Following this procedure we can quickly evaluate alternative wire sizes, wire materials and determine the fraction of the coil length occupied by the last layer.

From Figure 4-2, a considerable savings in wire length results by replacing a square core with one of circular cross section. It is inconvenient to fabricate a magnet with a true circular cross section from stacked laminations, but a circular cross section may be approximated by varying the widths of the laminations.

If many laminations are used, the cross sectional shape may be approximated by a regular polygon of (2N+2) sides - where N is the number of laminations. This accounts for 2N exposed edges of the laminations and the two exposed sides.

This polygonal approximation implies a variation in the thickness of the laminations because the sides of the polygon are not perpendicular to the width of the laminations. The ratio of the minimum thickness to the maximum thickness is

$$\frac{\hat{T}}{\check{T}} = \frac{l \sin \frac{\pi}{N+1}}{l}$$

$\check{T}$  = minimum lamination thickness

$\hat{T}$  = maximum lamination thickness

$l$  = length of a side of the polygon

$N$  = number of laminations

With this limitation in mind we proceed as follows.

The perimeter and area of the polygon are given by

$$\text{Area} = (2N+2) \frac{D^2}{4} \tan \frac{\pi}{2N+2}$$

$$\text{Perimeter} = (2N+2) D \tan \frac{\pi}{2N+2}$$

$D$  = diameter of inscribed circle

$N$  = number of laminations

$2N+2$  = number of sides to polygon

But if  $N$  is greater than 5, then

$$(2N+2) \tan \left( \frac{\pi}{2N+2} \right) = 12 \tan (15^\circ)$$

$$= 1.023\pi$$

So, within 2%, the area and perimeter of the polygon are the same as that of the inscribed circle.

From this we conclude that the advantage in wire length for circular cross section can be gained by stacking as few as five laminations if the widths are cut to approximate a circular cross section.



## 4.2 Conductor Materials

At present, the only practical conductor materials are aluminum and copper, but should another material be considered, some of the most desirable properties are given here.

The conductor characteristics of prime importance are density and resistivity. Quite obviously, the conductor material should be selected for minimum density to minimize coil weight, and should be selected for minimum resistivity to minimize power. Unfortunately, these two characteristics do not necessarily go hand in hand, and the optimum material will depend on the specific application. In the case of a planar air coil with little build, the power and weight may be traded one for one. In this case the product of density and resistivity becomes a meaningful measure of conductor quality. But when the coil build is appreciable, this is no longer a useful guide.

It is possible to predict the crossover point where comparison of the resistivity-density product of two materials will no longer indicate the conductor material for a minimum weight coil, but this must be done for a specific core geometry and specific core material. (See section 4.3)

Should a conductor material other than aluminum or copper be considered, several other properties besides resistivity and density must be considered. Copper and aluminum have well known properties and any other material will require extensive effort to become established. The properties which must be established include flexibility, mechanical stability under winding pressure and tension, susceptibility to creep, effects of impurities, and other odd properties such as the tendency of silver to migrate through dielectric materials or the growth of crystals from the base metal (whiskers).

### 4.3 Coil Power

The magnetizing coil for a given magnetic core may be designed for a wide range of peak magnetizing power, with coil weight decreasing as peak power is increased. The lower limit on coil power is fixed by the magnetic core design and the coil conductor material. These effects are easily demonstrated by taking specific examples.

The minimum power effect is illustrated by examining the effect of adding more layers of wire to the magnet assembly in Figure 4-4 which is a single layer coil wound with wire whose diameter is one tenth the core diameter. The change in coil resistance due to the additional coil layers is proportional to the increase in wire length.

The original layer of wire will have a mean length per turn of  $\pi(d + 10d)$ , and the mean turn length in a second layer will  $\pi d(10 + 3)$ . The mean diameter of subsequent layers will increase by two wire diameters for each additional layer so the mean length of a turn in the  $n$ th layer is  $\pi d(9 + 2n)$ .

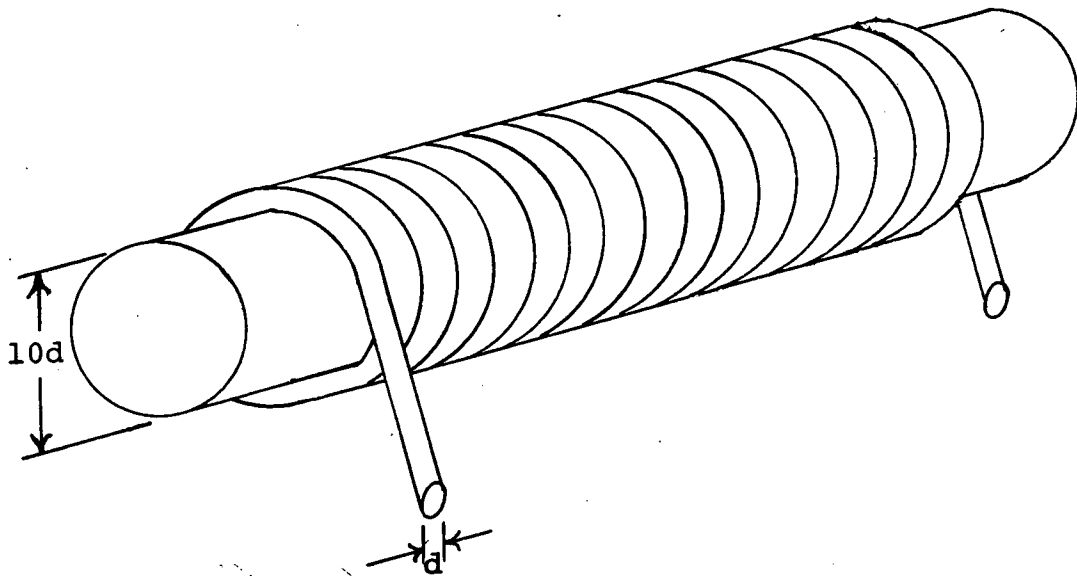


Figure 4-4

Using

$$P = i^2 R$$

and letting subscripts denote the total number of layers, the power in the original coil is given by:

$$P_1 = (i_1)^2 R_1$$

Now when we add a second layer of wire we will have doubled the number of turns so we must halve the current to hold the magnetizing field strength constant.

$$P_2 = \frac{i_1^2}{2} R_2$$

$$= \frac{i_1^2}{2} R_1 \left[ 1 + \frac{\pi d (10+3)}{\pi d (10+1)} \right]$$

$$P_2 = \frac{(i_1)^2 R_1}{2} \times 1.09$$

For a three layer coil we have

$$P_3 = \frac{i_1^2}{3} R_3$$

$$= \frac{i_1^2}{3} R_1 \left[ 1 + \frac{\pi d (10+3)}{\pi d (10+1)} + \frac{\pi d (10+5)}{\pi d (10+1)} \right]$$

$$P_3 = \frac{(i_1)^2 R_1}{3} \times 1.18$$

and for a  $\lambda$  layer coil the power is

$$P_\lambda = \frac{(i_1)^2 R_1}{\lambda} \frac{10+\lambda}{10+1}$$

Now we have obviously reduced the power requirements, but not as rapidly as we have increased the total number of turns. The limiting power with an infinite number of coil turns (and layers) will be given by

$$\lim_{\lambda \rightarrow \infty} P_{\lambda} = (i_1)^2 R_1 \frac{1}{D/d+1}$$

This would seem to indicate that there may be an advantage to using fine wire so that the limiting power would be less. But the actual effect is only to increase the power for a single layer coil so that a greater reduction in power is possible.

Notice in the previous illustration that coil weight increases more rapidly than the number of turns because of the increased length of a turn. By the same line of reasoning used in determining the coil resistance, the coil weight is

$$W_{\lambda} = W_1 \lambda \frac{10+\lambda}{10+1}$$

and the product of coil weight and power becomes

$$P_{\lambda} W_{\lambda} = P_1 W_1 \frac{10+\lambda}{10+1}^2$$

or to give specific examples

$$P_2 W_2 = 1.19 P_1 W_1$$

$$P_3 W_3 = 1.40 P_1 W_1$$

$$P_4 W_4 = 1.62 P_1 W_1$$

Figure 4-5 shows the effect of increasing the number of coil layers on the coil weight, coil power and on the coil weight - power product. These results are not restricted to this specific geometry, but can be generalized to show that the minimum magnetizing power is independent of the wire diameter.

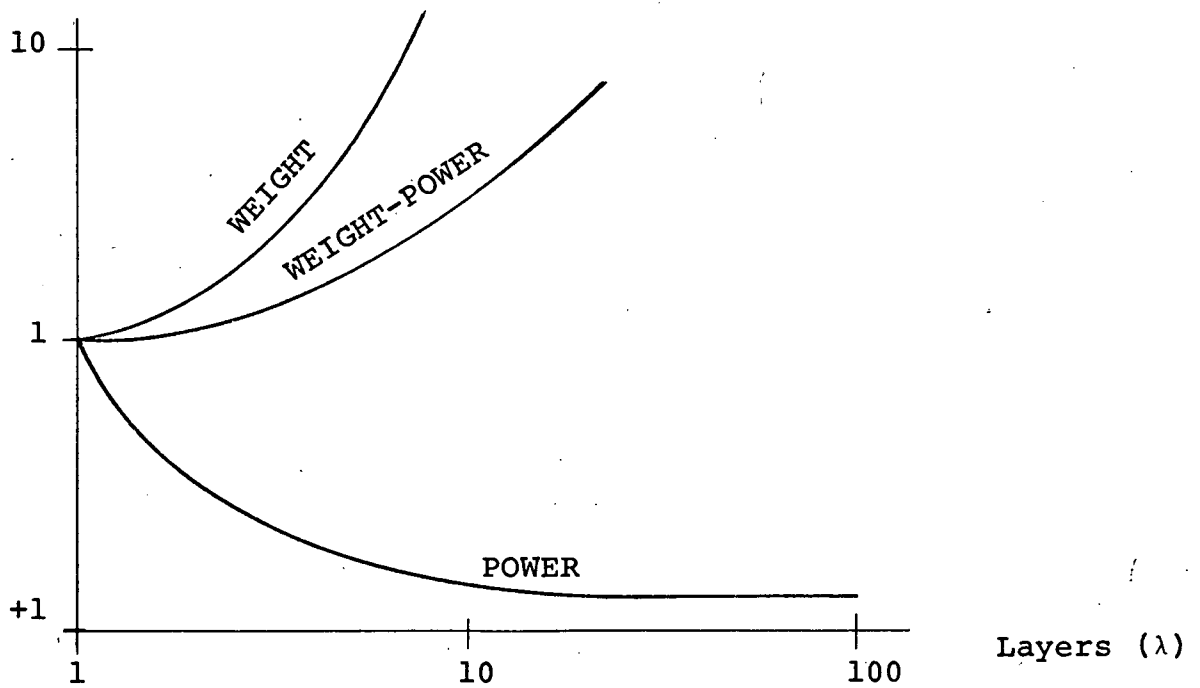


Figure 4-5 Variation of Coil Parameters with Coil Layers

In the limit when extremely large coils are used, the actual shape of the core cross section becomes immaterial, and the limiting power is a function of the magnetic field strength required, the length of the coil and the resistivity of the conductor. By combining equations 2-13, 4-29, 4-31 and 4-33 we may solve for the limiting power with an infinite amount of conductor. The limiting power is given by

$$P_0 = 2.81 H_{pk}^2 \ell c'$$

which for aluminum and copper conductor materials becomes

$$P_{al} = 7.95 \times 10^{-6} H_{pk}^2 \ell c$$

$$P_{cu} = 4.85 \times 10^{-6} H_{pk}^2 \ell c$$

where a reasonable estimate of insulation thickness has been included.

These results point to another effect due to coil build. When a coil is constructed of aluminum and another coil is constructed of copper, with the same wire diameter, number of layers and turns, the aluminum coil has one third the weight because aluminum is less dense. The copper coil requires 60% as much power as the aluminum coil because copper has a greater conductivity. We might therefore expect to be able to construct an aluminum coil that requires the same power as the copper but with less weight. But coil weight and power do not trade one for one, so an aluminum coil is lighter only when the power is above some threshold value.

This threshold power can be determined by setting the weight of two coils equal and solving for the power. The resulting threshold power for materials denoted by subscripts 1 and 2 is approximately

$$P_{1-2} = 2.81 \times H_{pk}^2 \ell c \quad 2 \frac{\frac{1}{\delta_1} - \frac{1}{\delta_2}}{\frac{1}{\rho_1 \delta_1} - \frac{1}{\rho_2 \delta_2}}$$

And this threshold power for the most common choice of aluminum versus copper conductor is

$$P_{\text{al-cu}} = 26 \times 10^{-6} H_{\text{pk}}^2 l_c$$

For a 10,000 p-cm magnet 25 cm long and requiring 150 Oersteds, this threshold power is on the order of fourteen watts.

The peak coil power for a permanent magnet is useful for determining the weight of the magnetizing coil and for determining the circuit requirements for the coil driver. However the peak coil power is not a valid basis for comparing the power of different systems unless the time duration of the power drain is considered.

The charging energy -- or average power during a charging cycle can be shown to be independent of the coil resistance. This can be seen by considering a series RL circuit (Fig. 4-6). When the switch is closed the current will follow the familiar exponential rise as shown in Fig. 4-6.

If the circuit is interrupted when the current reaches some portion of the maximum possible  $\frac{V_o}{R}$ ,

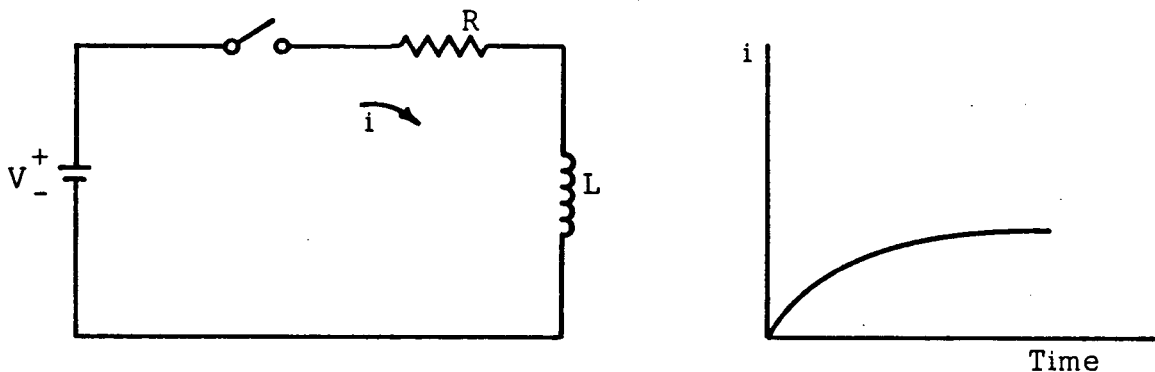


Figure 4-6

then the energy supplied will be the product of the supply voltage and the average current supplied to the circuit. If the resistance is then doubled, the supply voltage must be doubled to maintain the same maximum current. Now, when the switch is closed the current will rise twice as fast because the  $L/R$  time constant has been halved. If the switch is opened at the same current level as before, then the peak current will be the same as before, but the energy supplied to the circuit has not changed.

This same line of reasoning can be extended to show that the energy required to apply a given magnetic field to a given core is independent of the coil parameters. This, of course, assumes that the spatial distribution of the magnetic field is the same for all coils. A very large diameter coil will obviously have more leakage than a small diameter coil of the same length, but when treating relatively small coils the energy required to charge a magnet is independent of coil turns, wire size and conductor resistivity.

#### 4.5 SCALING

When the magnetic core is scaled (see 3.5) to produce a different magnet size from a given design, the coil dimensions must also be scaled. In this section we take a scale factor  $s$ , scale all coil dimensions, and determine the effects of this scaling.

If the coil length and wire diameter are scaled by the same factor, then the number of turns which will fit on one layer will be constant. Similarly, the number of layers is constant when the wire diameter and coil built are scaled by the same scale factor.

The length of a turn in any particular layer is scaled by  $s$ , and consequently the wire length is scaled by  $s$ .

The resistance of the coil varies directly with the wire length and inversely with the square of the wire diameter, so the coil resistance is scaled by  $s^{-1}$ .

For the magnetic field strength to remain constant, the current must be scaled by  $s$ . This can be seen from equation 2-13.

$$H = \frac{.4\pi n_1 i_1}{l_1} = \frac{.4\pi n_2 i_2}{l_2}$$

$$\frac{.4\pi n_1 i_1}{l_1} = \frac{.4\pi n_1 i_2}{s l_1}$$

$$i_2 = s i_1$$



The scale factor for peak power can now be readily determined from

$$P = i^2 R$$

by using the scale factors for current and resistance. The scale factor for peak power is  $s$ . The energy required to charge the magnet is proportional to the volume of the coil and core - e.g. to  $s^3$ . Thus peak power scales by  $s$  and magnetizing time by  $s^2$ .

The last scale factor to consider is for voltage. This is easily found by taking the product of the scale factors for current and resistance, with the result that voltage is unchanged.

Another simple scaling method is possible - the coil dimensions may be scaled by  $s$ , but the wire diameter is unscaled. This method of scaling gives a scale factor of  $s^3$  for coil resistance and wire length. The scale factor for peak power, number of turns per layer and number of layers is  $s$ . The coil voltage is scaled by  $s^2$  and peak current by  $s^{-1}$ . The magnetizing time is scaled by  $s^2$ , and peak power by  $s$  so that magnetizing energy is again scaled by  $s^3$ .

There are two limitations to coil scaling: fine wire usually has relatively heavy insulation; wire diameter is quantized at approximately 20% intervals. Neither of these is a serious objection and only a minor adjustment to a scaled coil design is ever needed in practice.

## 5.0 MAGNET WEIGHT

### 5.1 Core Weight

In section 2.2, it was pointed out that short magnets generate a self-demagnetizing field which partially demagnetizes the magnet in the absence of an externally applied magnetizing force. This geometry effect was used in section 3.2 to find the maximum residual induction in the magnetic core as a function of the moment and core length.

Because the dipole moment, induction and volume of core material are related by equations 2-5 and 2-6, and by assuming 30% leakage, we may write for the core volume

$$(5-37) \quad \text{Volume} = \frac{4 M_r}{0.7 B_r}$$

where  $M_r$  and  $B_r$  are the residual moment and the residual induction respectively. The weight of the magnetic core is simply the product of core volume and the density of the core material, so data points from 3-2 may be used to generate curves of core weight vs residual moment vs core length.

Figure 5-1 gives core weight as a function of core length for a 1000 pole-cm magnet. As might have been expected, these curves flatten out for long magnets where the self-demagnetizing force becomes small.

This curve may be used for other magnet sizes by scaling (see section 3.5 or 5.4). The weight will scale directly with the moment and the length with the cube root of the moment. To illustrate, consider the problem of finding the minimum core weight for a 12,000 pole-cm P6 magnet in 25cm of length. The dipole moment is scaled by a factor of twelve, so the length is scaled by the cube root of twelve or 2.29. The length scaled down to 1000 pole-cm is 10.9cm (25cm divided by 2.29,) so we enter figure 5-1 at 10.9cm. The indicated weight is 12.9 grams for P6 material, which must be scaled by twelve. The minimum weight for a 12,000 pole-cm magnet of P6 material in 25cm of length is 155 grams.

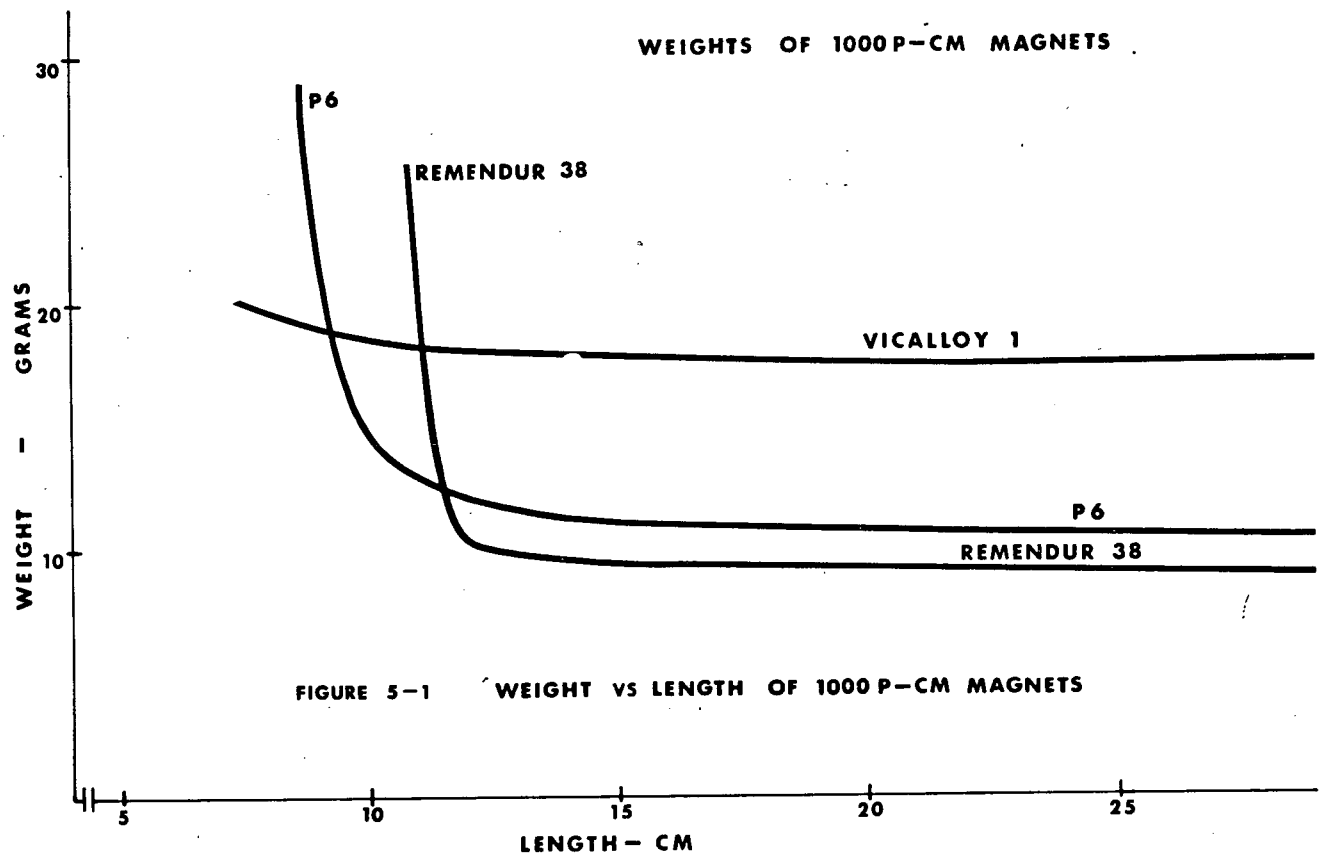


Figure 5-1

## 5.2 Coil Weight

The weight of the magnetizing coil is determined by the magnetic core material, the required dipole moment, magnet length and the peak power.

Specification of the magnetic core material, dipole moment and magnet length will determine the slenderness ratio and the core volume. These in turn determine the peak magnetizing force necessary to satisfy the material requirements and to overcome the self-demagnetizing force (section 2.2). The coil weight is an increasing function of core volume and peak magnetizing force, but is a decreasing function of coil power.

The peak coil power cannot be reduced beyond a threshold power because coil losses increase rapidly with coil size (section 4.3). The minimum coil power is given by

$$(5-38) \quad P_O = 2.81 H_{pk}^2 l_c$$

Several expressions for the coil weight may be derived from the information in chapters 3 and 4. One convenient form giving the coil weight relative to the core weight is

$$(5-39) \quad \frac{W_{wire}}{W_{core}} = \frac{\frac{\phi^2 c}{a} \frac{\delta_{wire}}{\delta_{core}}}{4.437 \frac{P}{P_O} - \frac{80}{9} + 4.452 \frac{P_O}{P}}$$

This equation with the numerator set equal to one is plotted in Figure 5-2. Notice that for large

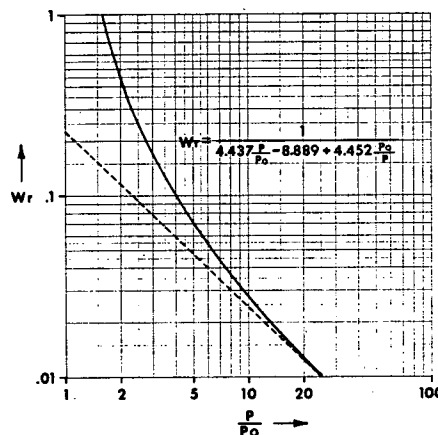


Figure 5-2 Variation of Coil Weight with Peak Power  
peak power the curve is asymptotic to  $(4.437 P/P_O)^{-1}$ .

### 5.3 Magnet Assembly Weight

The weight of the total magnet assembly consists not only of the weight of the core and coil, but also includes the weight of the housing, potting or encapsulation, connector(s), and any internally mounted sensors for temperature, moment, etc.

The sensors will generally be very small, light devices and their weight will be insignificant. But the weight of the housing, potting and connector will depend on the specific circumstances and can be expected to increase the total weight by at least 25%.

In view of the number of variables, it is more convenient to find the weight of the core and the weight of the foil separately as detailed in sections 5.1 and 5.2.

### 5.4 Scaling

When scaling an extant magnet design to obtain a different size, there are two principle limitations. The most troublesome of these is that wire is available only in discrete sizes, so exact coil scaling will not usually be possible.

The second important limitation is the effect of scaling on the magnetic properties of the core materials. As discussed in 3.5, this is not a serious limitation if the magnet core is fabricated of stacked limitations.

Table 5-1 lists most parameters of interest with their scale factors for a magnet with all dimensions scaled by a factor  $s$ . These scale factors are exact for materials whose properties do not change with size - in spite of the heuristic development in sections 3.5 and 4.5.

TABLE 5-1 MAGNET ASSEMBLY SCALE FACTORS

	<u>Fixed Voltage Scaling</u>	<u>Fixed Wire Size Scaling</u>
Moment (M)	$s^3$	$s^3$
Total Weight	$s^3$	$s^3$
Magnetizing Energy	$s^3$	$s^3$
Core length ( )	$s$	$s$
Core diameter (D)	$s$	$s$
Distance for equal remote field (r)	$s$	$s$
Magnetic field strength (H)	$1$	$1$
Magnetic induction (B)	$1$	$1$
core weight	$s^3$	$s^3$
coil length ( c)	$s$	$s$
coil turns ( )	$1$	$s^2$
coil layers ( )	$1$	$s$
turns per layer	$1$	$s$
wire diameter	$s$	$1$
wire length	$s$	$s^3$
coil weight	$s^3$	$s^3$
coil current	$s$	$s^{-1}$
coil resistance	$s^{-1}$	$s^3$
voltage	$1$	$s^2$
power	$s$	$s$

where  $s$  is a dimensionless scale factor.

## 6.0 Magnet Design Curves

The following curves can be utilized to estimate the size, weight, and power of chargeable permanent magnets. The design curves are based on the elliptical geometry described in the next section.

### 6.1 Core Weight and Length

The size and weight of the magnetic core for a wide range of dipole moments can be determined from Figures 1 and 2.

### 6.2 Coil Weight

The weight of the magnet coil will depend on the peak power used to change the magnetic state. By peak power is meant the power required to just saturate the magnet. This dependency can be seen by performing a mental experiment. If half the turns are stripped off the coil, the resistance, wire length, and turns will be approximately halved. If this stripped coil is connected to the same DC voltage as used by the full coil, the current will double but the number of ampere-turns will remain constant. This stripped coil will thus have approximately the same effect on the magnetic core as the full coil but at twice the peak power and half the weight.

Figure 3 shows the tradeoff between coil weight and peak power for several magnet sizes. These curves do not include the effect of insulation on coil weight. Notice that for large peak power, the coil weight and power can be traded one for one (i.e., doubling the coil weight requires half the power), but small peak power results in a considerable weight penalty because of coil build-up effects.

Insulation weight will range from 5% of coil weight for high power coils to 15% for low power coils.

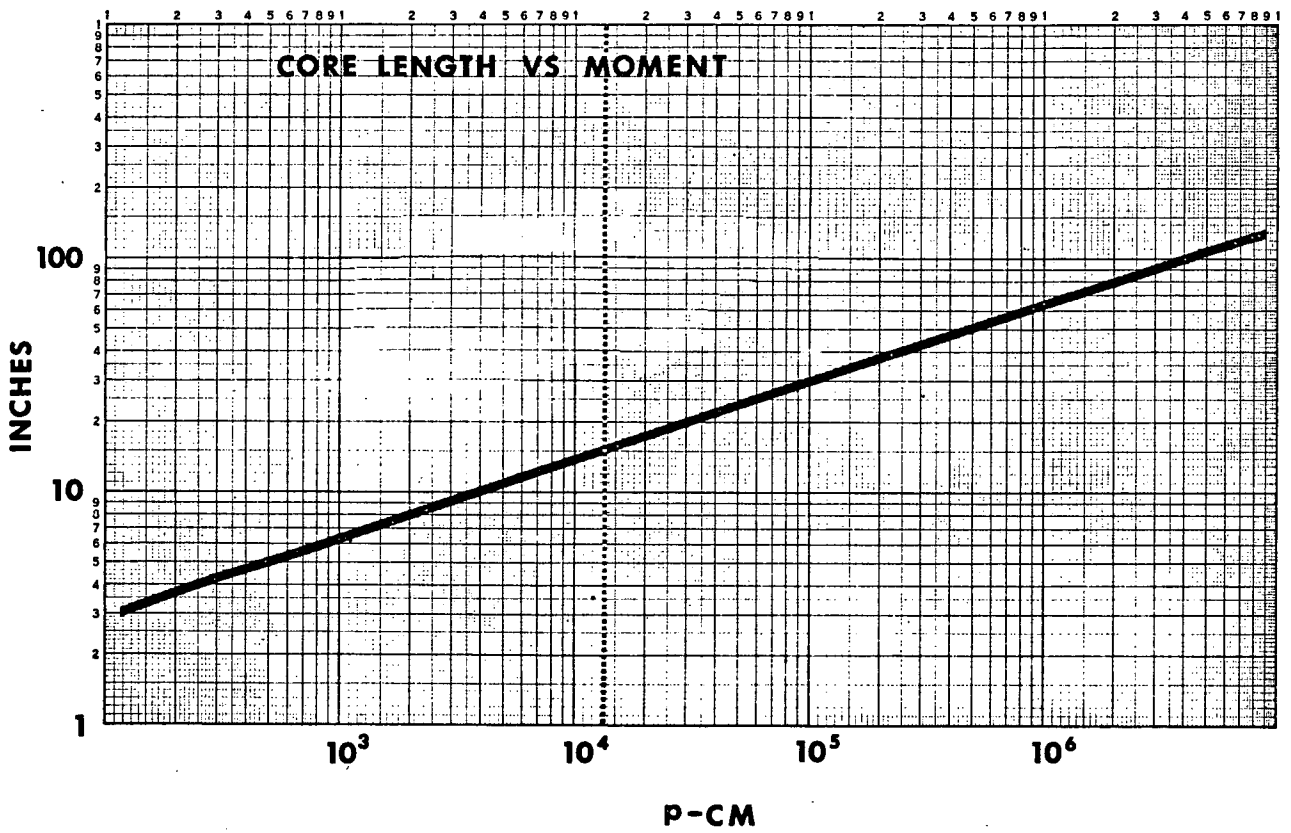


Figure 1. Length of Core vs. Maximum Dipole Moment



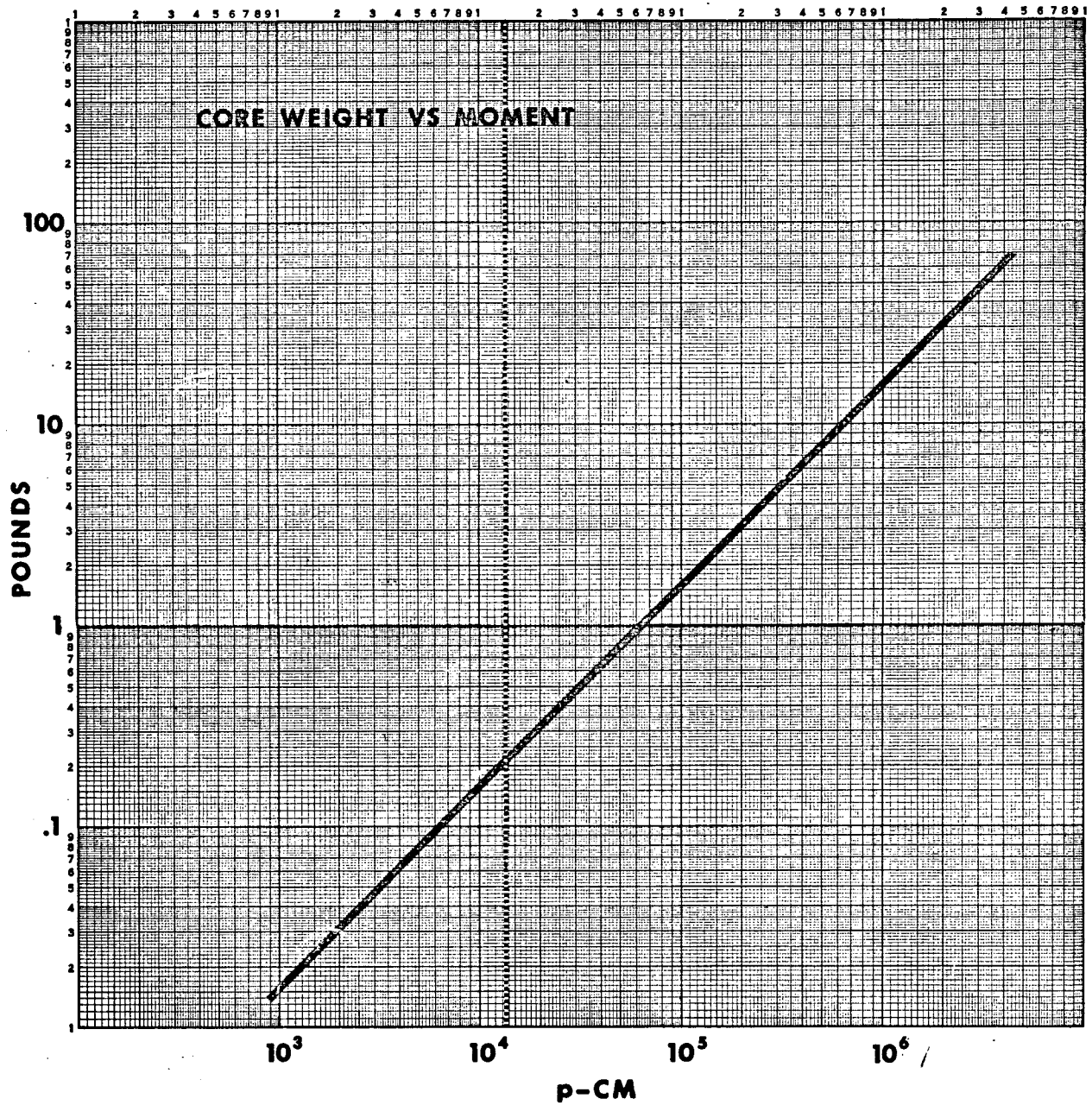


Figure 2. Core Weight vs. Moment

### 6.3 Switching Energy

It is somewhat misleading to talk of power used by variable permanent magnets, as power is consumed only when the dipole moment is changed. A more meaningful concept is the energy used for each change. This energy goes to three sinks in the circuit, but must all come from the satellite power supply.

The first energy sink is the hysteresis of the magnet material. Any change in magnetic state requires energy proportional to the area of the B-H loop traversed. For well designed systems, this is the dominant energy sink. The second sink is  $I^2R$  loss in the coil.

The final sink is the charging circuit. The simplest and most efficient charging technique is to switch the coil directly to the spacecraft power supply line, in which case this loss is essentially zero. For most magnets, assuming there are no severe limits on the peak current available from the power supply, this is by far the preferred technique. It is possible to isolate the spacecraft power supply from these current transients by using either capacitors or rechargeable batteries, but this carries a definite system weight penalty.

Figure 4 can be used to estimate both the time and the total energy required to switch a magnet between its extreme states. This includes core and coil losses. From these curves it is evident that approximately  $6 \times 10^{-5}$  watt sec/pole cm is required to change the state of a magnet, more or less independent of magnet size. Thus a 10,000p-cm magnet can be switched between its extremes ( $M = 20,000$  p-cm) at a cost of 1.2 watt sec of energy.

### 6.4 Example

The following example illustrates how to use these curves to determine the approximate magnet size and weight for a given set of requirements.

Maximum dipole moment required: 12,000 p-cm (12 amp m<sup>2</sup>)

Power supply voltage: 25 V

Peak current allowable: .3 amps

From Figure 2, the weight of the core will be .2 lb.

The length of the magnet assembly as taken from Figure 3 is 15 inches.

To determine the coil weight, we use Figure 4 and estimate the position of the 12,000 p-cm curve. We estimate the coil weight for 7.5 watts and 12,000 p-cm as 0.4 lb.

The magnetizing time for the magnet can be estimated from Figure 5. For a 12,000 p-cm magnet at 7.5 watts this time is approximately .14 seconds.

The estimated parameters are tabulated below for comparison with an actual magnet assembly.

	<u>Estimated</u>	<u>Actual</u>
Maximum Dipole Moment	12,000 p-cm	12,300 p-cm
Core weight	.2 lb	.22 lb.
Coil length	15 inch	15 inch
Coil weight	0.4 lb	0.48 lb

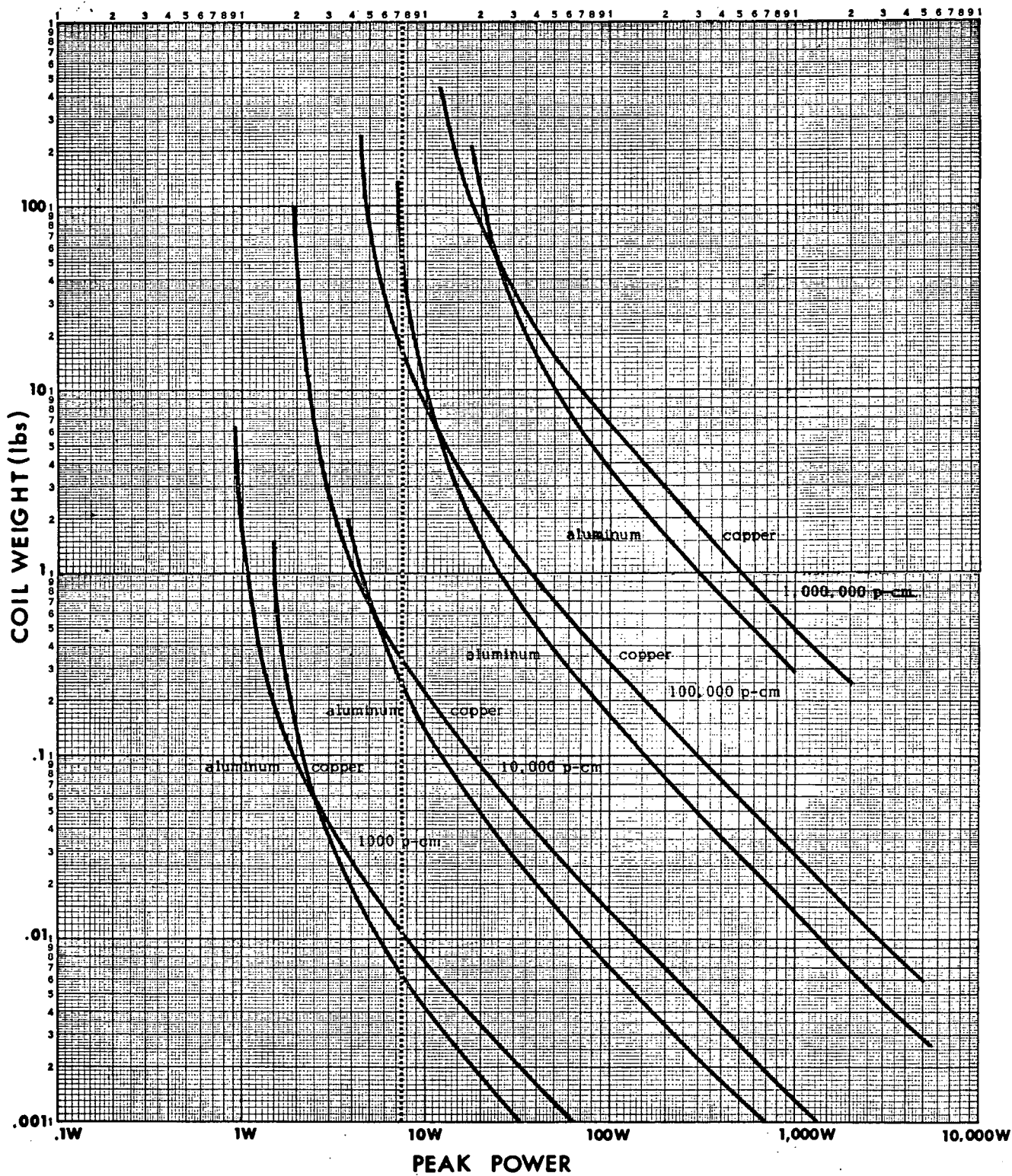
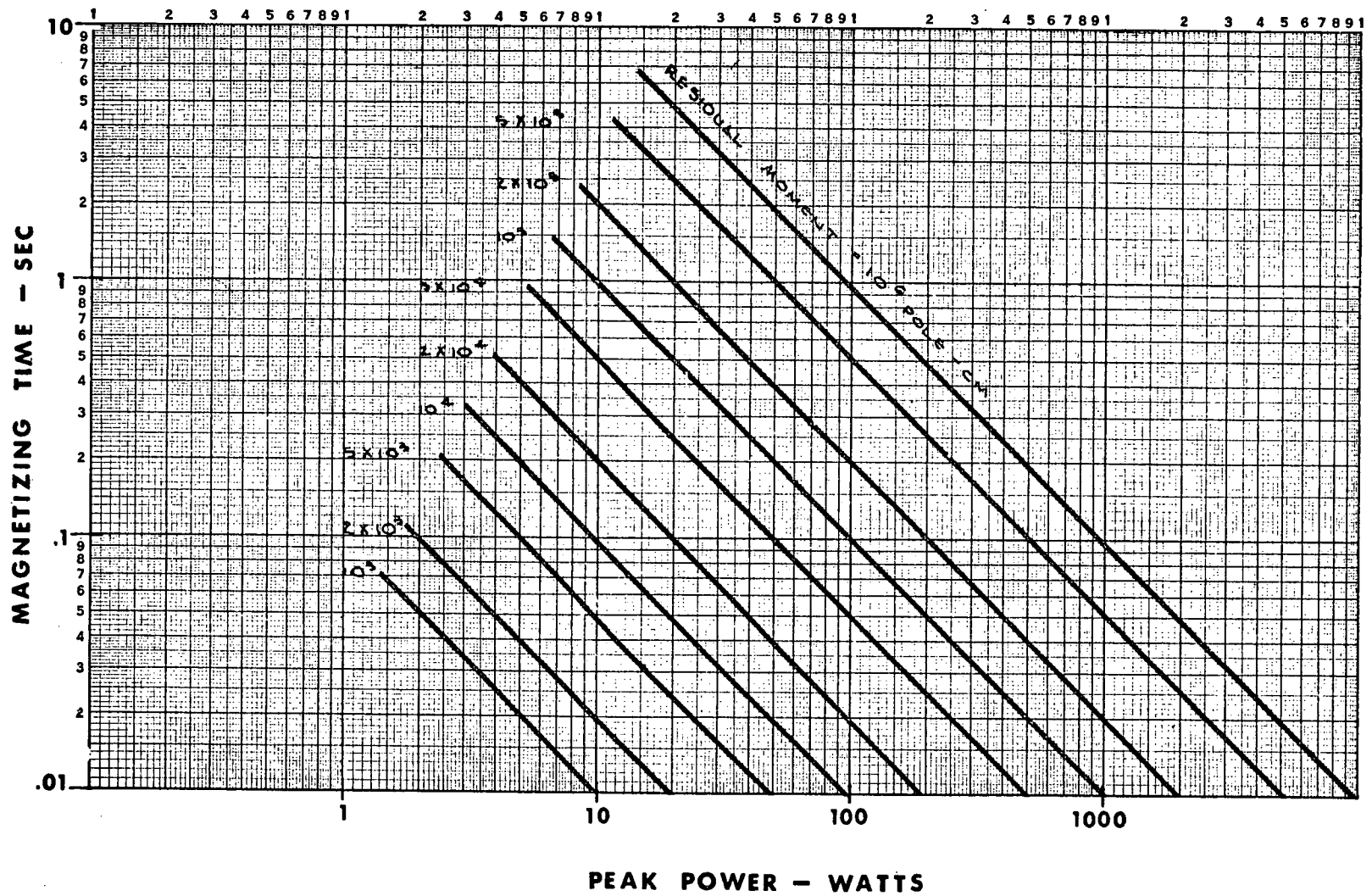


Figure 3. Coil Weight vs. Power

Figure 4. Magnetizing Time vs. Peak Power



## 7.0 Description of Final Magnet Design and Performance

### 7.1 Introduction

This section presents test results and construction details for an elliptical chargeable permanent magnet. The test magnet is in the form of a prolate ellipsoid with integral magnetizing coil.

### 7.2 Sensing

One of the most difficult design problems is the implementation of the sensor for determining the state of the magnet. Such a sensor is desirable in balancing applications for telemetry purposes, and is essential in control applications because there is no way to properly control the state of the magnet without feedback from such a sensor.

The most convenient sensing device is the Hall sensor, which may be attached directly to the magnet. The primary difficulty arises from the fact that the magnetic state in the vicinity of the sensor does not necessarily represent that of the entire magnet. The accuracy of the sensed moment is therefore dependent on magnet history. The optimum configuration of the many that were investigated was for the sensor to be mounted near the end of an elliptical core, with a soft iron pole piece outboard of the sensor. This configuration is described in the drawings, and gives the sensing accuracy described in the accompanying curves.

### 7.3 Test Results

The magnet core is a 14 inch long by 0.34 inch diameter prolate ellipsoid and the weight of the magnet core and magnetizing coil is 0.575 pounds (262 grams).

The maximum residual magnetism for this magnet is 13,400 pole-cm and accuracy of the telemetry is  $\pm 200$  pole-cm ( $\pm 1.5\%$ ). The accuracy increases when the magnet is utilized to less than its maximum moment capability - but a large decrease in moment is accompanied by a small increase in accuracy. These effects can be seen in the sensed moment vs actual moment curves of figures 1 and 2.

5 X 5 TO THE CENTIMETER 46 1612  
18 X 24 CM.  
MADE IN U.S.A.  
KEUFFEL & ESSER CO

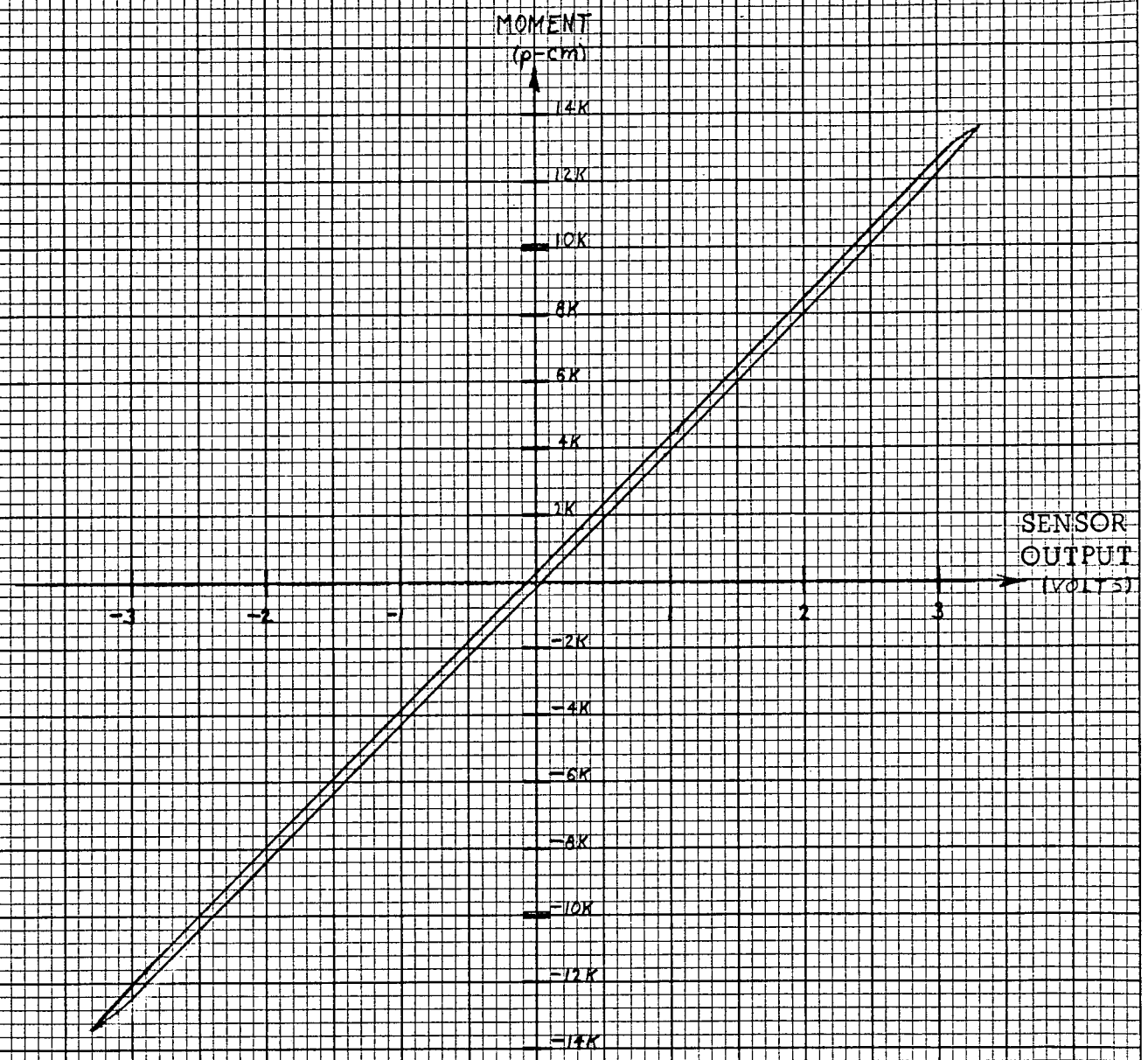


Figure 7-1 MOMENT vs. SENSOR OUTPUT  
Elliptical Magnet s/n 15031

## 7.4 Magnet Construction

The test magnet was fabricated in the same major steps as are all ITHACO magnets. These steps are: fabricating the magnetic core which includes bonding laminations into a stack and grinding to final form; magnet cap assembly; winding the coil; potting and housing the complete magnet.

### 7.4.1 Magnet Core

Construction of magnetic cores begins by cutting Remendur 38 core material to rough size from 0.02 inch strip stock. The rough cut strips are heat treated at 1100°F in an inert atmosphere. After a two hour bake the strips are cooled at 100°F per hour to 900°F and then removed from the oven to cool in ambient air.

The heat treated strips are next bonded together with epoxy to form a rectangular bar and then ground to final shape. This magnet was ground to an elliptical shape with one end cut off square as shown in figure 3a.

### 7.4.2 Magnet Cap

The magnet caps are 3 piece assemblies as shown in sketch SK00224. Part #1 in this sketch is used as a partial coil form on both ends of the magnet. Figure 3b shows parts #1 bonded to the magnet core.

One end of the magnet core is ground flat to provide a flat face for the Hall sensor. The sensor is a small rectangular plate and is bonded to SK00224 part #3. Part #3 is then slid into part #2 with the sensor facing out, the sensor leads are placed in the wire channel and this assembly is slid into part #1. The sensor is then sandwiched between part #3 and the flat end of the magnet core. The final assembly step for the magnet cap is securing the plug part #2 in place with set screws. The end caps and core are now ready for winding the coil.

### 7.4.3 Magnetizing Coil

This magnetizing coil is a conventional solenoid consisting of 3703 turns of #26 AWG copper wire in 5 layers. After winding, the coil was coated with PC22 polyurethane and cured. The magnet assembly is shown in figure 3c before conformal coating.



Magnet initially AC demagnetized,  
then cycled to 3k p-cm, -3k p-cm,  
9k, -9k, 9k, -13k, 13k and finally  
to -13k p-cm.

MOMENT  
(p-cm)

4K

3K

2K

1K

-1K

-2K

-3K

-4K

TLM  
(VOLTS)

Figure 7-2 MOMENT vs. SENSOR OUTPUT

Elliptical Magnet s/n 15031

At this point the magnet assembly is functionally complete. The remaining operations are inserting the magnet into its housing, potting the assembly and painting the housing.

#### 7.4.4 Potting and Housing

The housing selected for the test magnet was a 15 inch length of fiberglass tubing with an inside diameter of 5/8 inch. The space between the magnetizing coil and the tube was filled with PR1524 polyurethane.

This complete magnet assembly is 15 inches long x 3/4 inch diameter and weighs 1.0 pounds including a 6 ft. cable.

#### 7.5 Test Method

The magnet was tested by placing the magnet on a wood table and sensing the remote field of the magnet with a flux gate magnetometer. The magnetometer probe was positioned parallel to the long axis of the magnet at a spacing of 45.5cm. At this spacing the calculated scale factor is 10 milligauss per 1000 pole-cm.

The magnetizing coil was energized for this test by a 1400uf bank of capacitors in the MMCA Test Panel. The MMCA Test Panel also has a polarity reversing switch and a selector switch which connects the capacitor bank to either an external power supply or to the magnetizing coil.

An amplifier was used to increase the output voltage of the Hall sensor to a more convenient level. As shown in figure 4, this consists of a differential amplifier with a gain of 50, which provides an offset adjustment control and also includes a bias network for the Hall sensor.

The entire test was conducted with all equipment on two wood tables. One table was used for the magnet under test and the magnetometer probe while all other equipment sat on the second wood table. This was done to minimize magnetic interference due to ferrous parts in the test equipment.

Reproduced from  
best available copy.

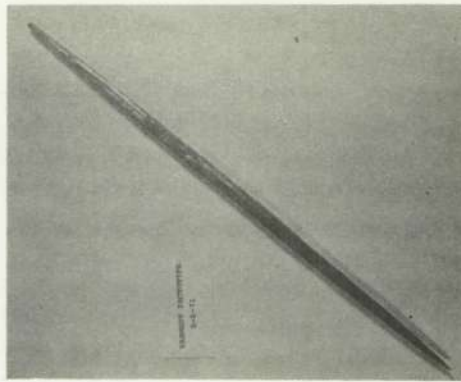


Figure 7-3a

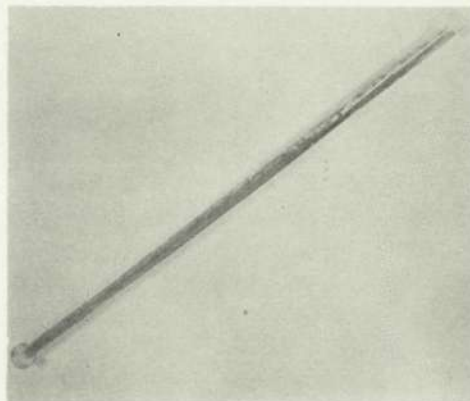


Figure 7-3b

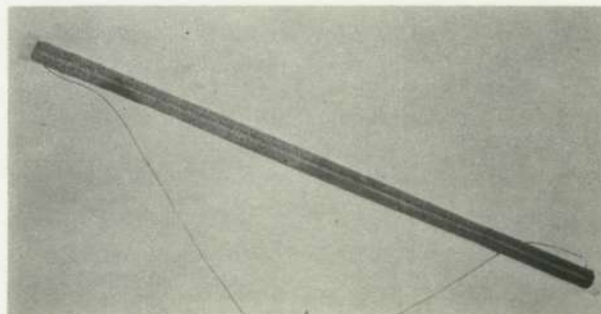


Figure 7-3c

Figure 7-3 Magnet Construction

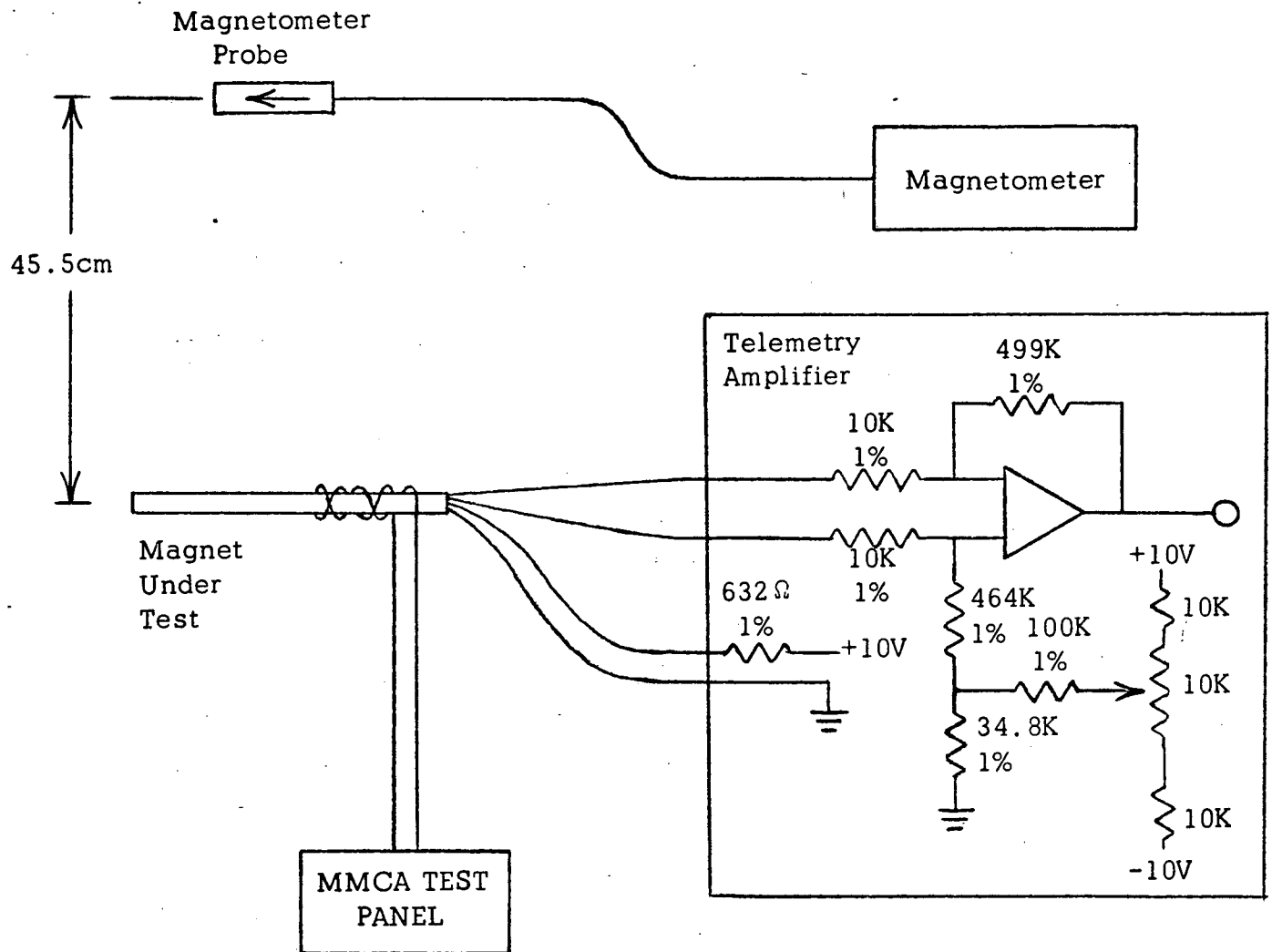


Figure 7-4 Test Set-Up



## II MAGNETIC ACQUISITION SYSTEM IMPLEMENTATION

1.0 Introduction

2.0 Description of Hardware

3.0 Magnetometer Noise Measurements

Appendix - A Magnetic Control System for Attitude Acquisition

## II MAGNETIC ACQUISITION SYSTEM IMPLEMENTATION

### 1.0 Introduction

An automatic attitude acquisition system has been developed under contract NAS5-21649. A description of this system and its performance is given in report no. 90345, which is included as an appendix to this section of this report.

The development of the hardware for this system was done under contract NAS5-21170, and is reported here.

### 2.0 Description of hardware

The hardware required for the magnetic acquisition system includes a 3 axis magnetometer, rate circuits, and 3 magnets. The magnetometer developed under this program is similar to other magnetometers made by Schonstedt Instrument Company, but repackaged for the applications. On the following pages will be found:

- a) A preliminary specification for a three-axis magnetometer.
- b) A Schonstedt control drawing for the magnetometer built to this specification.
- c) Test data on the engineering model magnetometer.
- d) A photograph of the magnetometer probe.

PRELIMINARY

February 10, 1972  
Report No. 90362

SPECIFICATION FOR  
A THREE-AXIS MAGNETOMETER

PREPARED BY:  
ITHACO, Inc.  
735 W. Clinton Street  
Ithaca, New York 14850



ITHACO, Inc.  
735 W. Clinton Street  
Ithaca, New York 14850

Report No. 90362  
February 10, 1972

SPECIFICATION FOR  
A THREE-AXIS MAGNETOMETER

Approved by: \_\_\_\_\_

J. S. Levy  
Project Engineer

Date: \_\_\_\_\_

\_\_\_\_\_  
\_\_\_\_\_

R. R. Fleming  
R&QA Engineer

Date: \_\_\_\_\_

\_\_\_\_\_  
\_\_\_\_\_

D. Sonnabend  
Program Manager

Date: \_\_\_\_\_

\_\_\_\_\_  
\_\_\_\_\_

R. Z. Fowler  
Vice President

Date: \_\_\_\_\_

## TABLE OF CONTENTS

	Page
1.0 SCOPE	1
2.0 APPLICABLE DOCUMENTS	1
2.1 NASA Publications	1
2.2 ITHACO Drawings	1
3.0 SPECIFICATIONS	1
3.1 Electrical Characteristics	1
3.2 Environmental Tests	2
3.3 Operability	3
3.4 Circuit Packaging	4
3.5 Hand Soldering	4
3.6 Selection of Components	4
4.0 PREPARATION FOR DELIVERY	4

## 1.0 SCOPE

This specification establishes the interface requirements and performance of a set of three magnetometers for use in the SATS attitude control system. In addition, this document references documents which pertain to the quality of workmanship and parts to be used.

## 2.0 APPLICABLE DOCUMENTS

The following documents form a part of this specification to the extent specified herein. In the event of a conflict between documents referenced here and the detailed content of this specification, the latter shall take precedence.

### 2.1 NASA Publications

NHB 5300.4 (3A) May 1968	Requirements for Soldered Electrical Connections
PPL-11 Revision A July 1971	GSFC Preferred Parts List

### 2.2 ITHACO Drawings

D41017	Frame, Electronics Univ.
C88135	Printed Circuit Card, Control Drawing

## 3.0 SPECIFICATIONS

### 3.1 Electrical Characteristics

The vendor shall supply three output voltages. Each voltage shall be proportional to one of three orthogonal components of the ambient magnetic field. A signal common shall also be supplied. The following specifications apply over the operating temperature range 0-50°C.

#### 3.1.1 Operating Sources

The magnetometer shall be capable of operating from externally supplied +10VDC and -10VDC  $\pm 1V$ .

#### 3.1.2 Sensitivity

The three components of the magnetic field shall be related to the respective output voltages by the factor 4VDC/Oersted  $\pm 2\%$ .

#### 3.1.3 Bi-polarity

Reversal of the probe direction will cause the output voltage to reverse sign.

3.1.4 Minimum Saturation Levels

The magnetometer shall not saturate when subjected to a magnetic intensity of 1 Oersted along the sensitive axis of the probe.

3.1.5 Null

In the absence of a magnetic field, the output voltage shall not exceed 20mVDC (at +25°C).

3.1.6 Linearity

The magnetometer output shall be linear to within 0.5% of full scale. Full scale shall be defined as 0.80 Oersted.

3.1.7 Ripple Voltage

The maximum allowable ripple voltage at the output of the magnetometer is 20mV peak-to-peak.

3.1.8 Temperature Stability

The change in null output voltage over the ambient range 0°C to 50°C shall be no greater than 30mV.

3.1.9 Noise

After processing by a test circuit, the output noise voltage shall be no greater than 32mV peak-to-peak. The figure is a schematic of the test circuit.

3.1.10 Crosstalk and Sensitivity to Crossfield

With all three magnetometers energized, apply the magnetic field along the mechanical axis of one of the magnetometers. The resultant voltage in each of the other two axes shall be equivalent to not more than 1 degree in misalignment. The null voltage shall be subtracted before performing the calculations.

3.1.11 Power Consumption

Average power shall not exceed 750mV.

3.2 Environmental Tests

The launch and orbit conditions to which flight models of this design will be subjected shall be considered.

- 3.2.1 The satisfactory operation must be maintained over the temperature range from  $-10^{\circ}\text{C}$  to  $+60^{\circ}\text{C}$ . Some degradation in analog relationships is permissible at the temperature extremes, but all operations must function properly.
- 3.2.2 The magnetometer shall be capable of meeting the requirements of Section 3.1 after being vibrated at the following levels with power applied.

#### Sinusoidal Vibration

Frequency Range (Hz)	Amplitude - "g" 0-to-Peak Thrust Axis
5-20	0.5" D.A.D.
20-30	10g
30-85	15g
85-110	37g
110-2000	15g
Transverse Axis	
5-21	0.5" D.A.D.
21-30	16g
30-2000	15g

#### Random Vibration

Direction	Frequency Band (Hz)	Spectral Density ( $\text{g}^2/\text{Hz}$ )	g-RMS
Thrust Axis	20-2000	0.2	20
Transverse Axis	20-2000	0.2	20

The duration of the test shall be 4 minutes in each direction -- 12 minutes total.

### 3.3 Operability

#### 3.3.1 Maintainability

The equipment shall be designed so that maintenance shall not be required during the specified operating and storage period.

### 3.3.2 Shelf Life

The equipment shall be capable of meeting the requirements of Section 3.1 after a two-year storage period, under the following environments:

Temperature	5 to 45°C
Relative Humidity	50% or less

### 3.3.3 Operating Life and Environment

The magnetometer shall be designed to function in the free space environment for a period of three years.

### 3.4 Circuit Packaging

The magnetometer electronics shall be packaged subject to the constraints imposed by the drawings listed in Sec. 2.2.

### 3.5 Probe Packaging

This section will be added later.

### 3.6 Hand Soldering

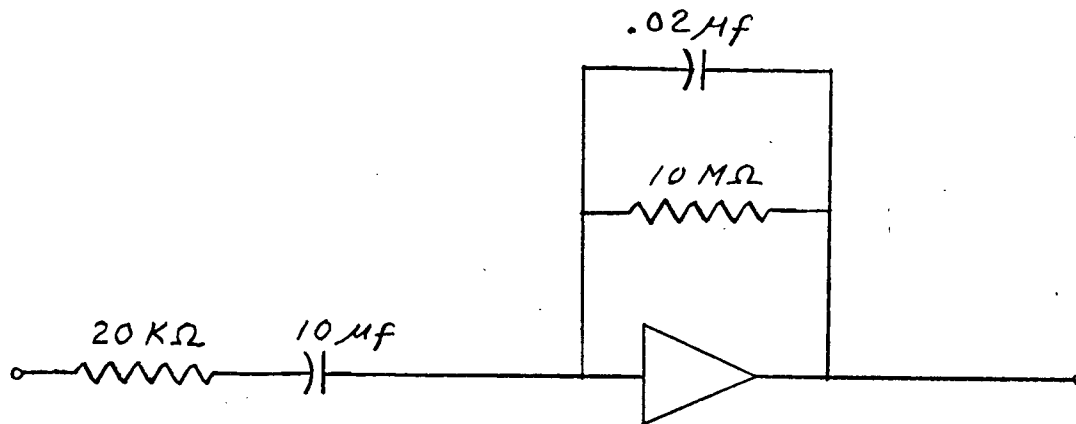
The provisions of NHB 5300.4(3A) shall apply to all hand soldering operations.

### 3.7 Selection of Components

Parts should be chosen from the GSFC Preferred Parts List (PPL-11, Revision A). Parts which are not on the Preferred Parts List shall be approved by ITHACO.

## 4.0 PREPARATION FOR DELIVERY

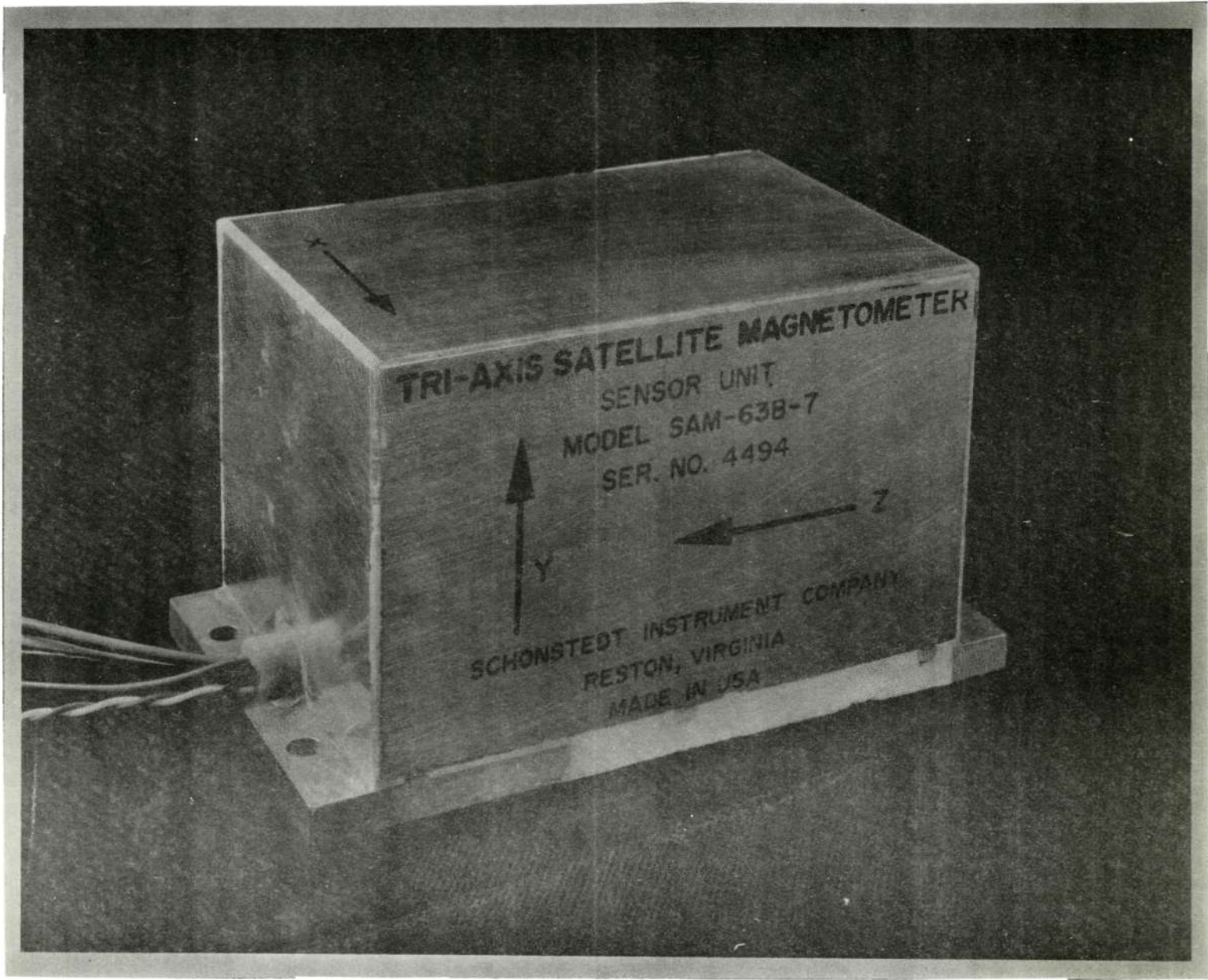
The subcontractor shall package the magnetometer in such a way as to prevent damage or deterioration during shipment. Packaging shall be subject to review and approval by ITHACO. All shipping containers are to be plainly marked with ITHACO purchase order number, name, quantity, serial number and ITHACO specification number.



TEST CIRCUIT FOR SECTION 3.1.9

(Circuit supplied by ITHACO)

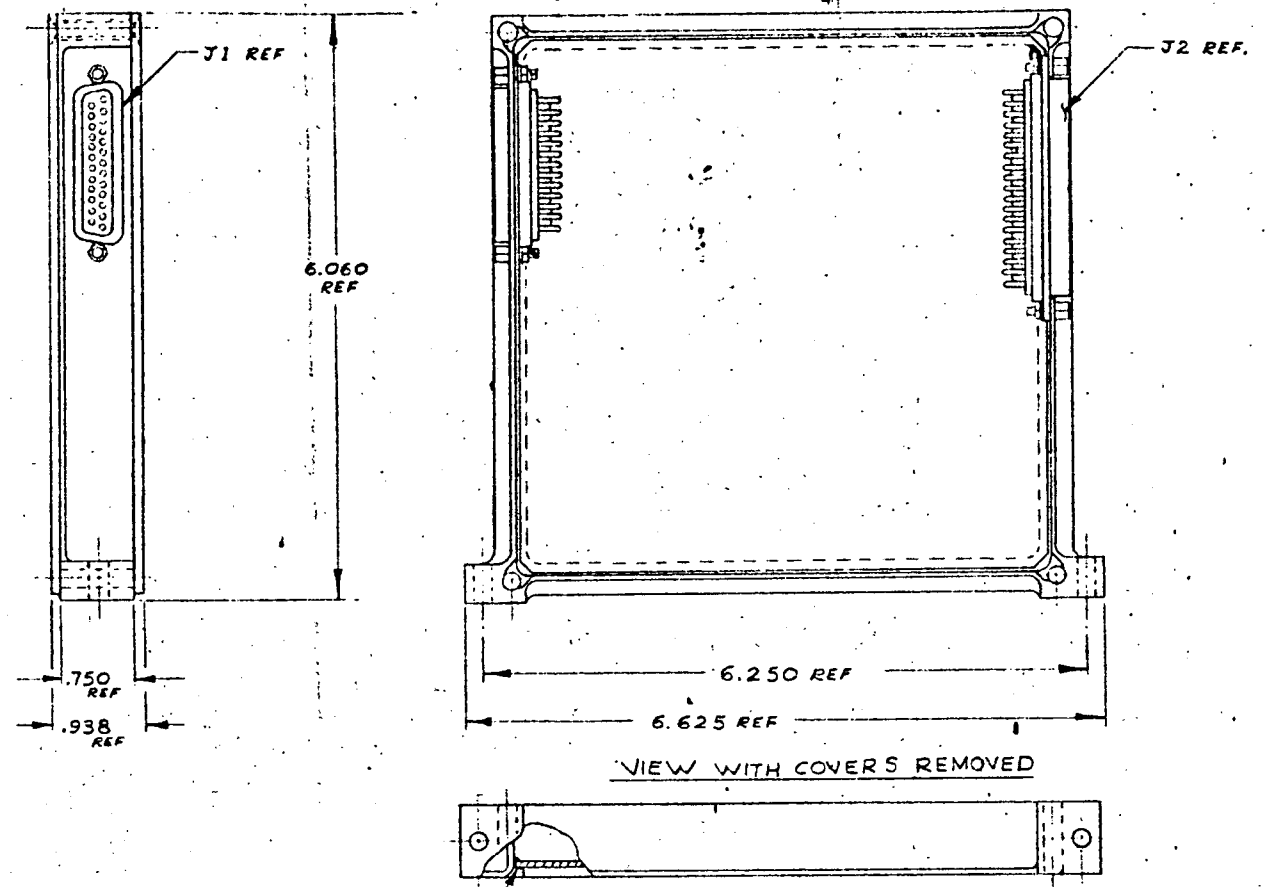
Reproduced from  
best available copy.



Magnetometer Probe



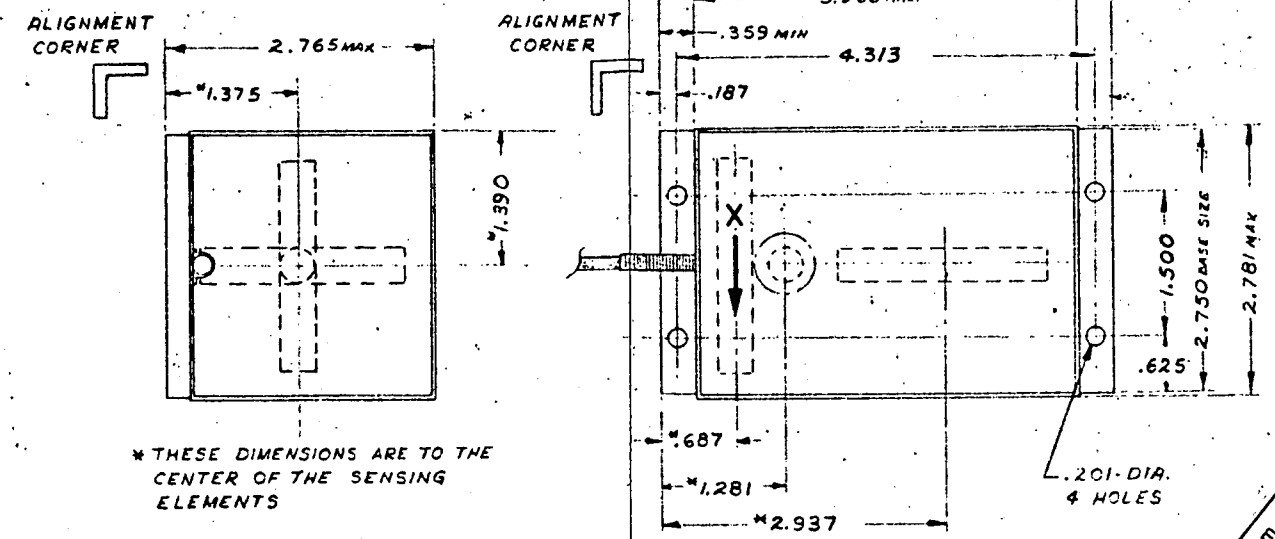
# FOLDOUT FRAME 1



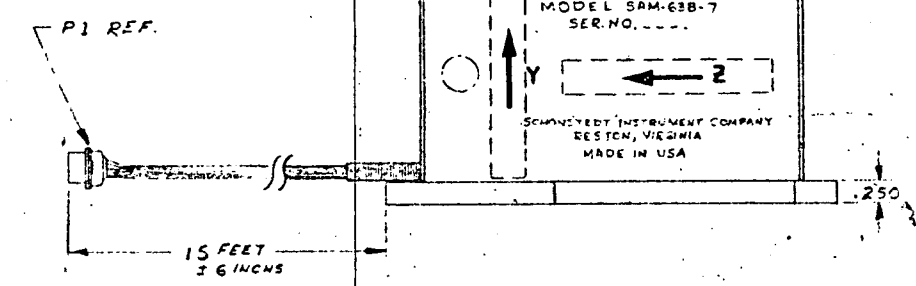
ADHESIVE  
ECCOBOND EC-55  
#9 CATALYST

CANNON CONNECTORS	
P1	DBMM-255-
J1	DBMM-25P-F
J2	DCMM-37P-F
P2	DCMM-37S-

# FOLDOUT FRAME 2



ARROWS INDICATE DIRECTION OF MAGNETIC FIELD FOR OUTPUT SIGNALS GREATER THAN THE BIAS LEVEL



ELECTRONIC UNIT										POWER & TELE.									
EXC	BLU	P1 1	1	EXC	CHASSIS GND	J2 R2 19	19	WHT	CHASSIS GND	WHT	37	37	WHT	CHASSIS GND	WHT	37	37	WHT	CHASSIS GND
EXC	WHT	3	3	EXC	OV	18	18	BLK	SIG OV	BLK	36	36	BLK	SIG OV	BLK	36	36	BLK	SIG OV
X SIG	BLU-BLU	10	10	X SIG IN	SIG OUT	17	17	BLU	Z SIG	BLU	35	35	BLU	Z SIG	BLU	35	35	BLU	Z SIG
Y SIG	ORA-ORA	8	8	Y SIG IN	Y	16	16	YEL	Y SIG	YEL	34	34	YEL	Y SIG	YEL	34	34	YEL	Y SIG
Z SIG	BLK-BLK	6	6	Z SIG IN	X	15	15	VIO	X SIG	VIO	33	33	VIO	X SIG	VIO	33	33	VIO	X SIG
END	GRN	25	25	CHASSIS GND	-10V	14	14	GPA	-10V	GPA	32	32	GPA	-10V	GPA	32	32	GPA	-10V
		13	13		+10V	13	13	RED	+10V	RED	31	31	RED	+10V	RED	31	31	RED	+10V

6ft 16"  
TEST CABLE  
NOT FURNISHED WITH INSTRUMENT

UNLESS OTHERWISE SPECIFIED DIMENSIONS ARE IN INCHES REMOVE BURRS AND SHARP EDGES TOLERANCES ON FRACTIONS ± DECIMALS ± ANGLES ±		APPROVED		19	
DO NOT SCALE THIS DRAWING		MATERIAL:		ELECTRICAL	
FINISH:		MECHANICAL		CHECKED	
SPECIFICATIONS OF LATEST ISSUE APPLY		DRAWN		DATE	
APPLICATION		NEXT ASSY		USED ON	
SLO/555 SAM-63B-7		SCALE		UNIT WT	
JOB ORDER		CUSTOMER REF.		SAM-63B-7	
S.I. CO. DRAWING NUMBER		REV		A	
401284		A			

Reproduced from  
best available copy.

REV A  
401284  
S.I. CO. DRAWING NUMBER

SCHONSTEDT  
INSTRUMENT CO.  
Silver Spring, Maryland

## SCHONSTEDT INSTRUMENT COMPANY

SAM-63B-7

Ithaco P/N C188168

Serial No. 4494TEMP. 25°CInput Voltage: +10  $\pm 0.1$  VDC  
-10  $\pm 1.0$  VDC

FIELD Noe	OUTPUT SIGNAL VDC			LIMITS, VDC	
	X	Y	Z	Min.	Max.
+1000	3.992	3.995	3.982	+4.0 Nominal	
+800	3.197	3.195	3.184	+3.136*	+3.264*
+700	2.797	2.796	2.786	+2.744*	+2.856*
+600	2.398	2.396	2.388	+2.352*	+2.448*
+500	1.999	1.997	1.990	+1.960*	+2.040*
+400	1.599	1.598	1.591	+1.568*	+1.632*
+300	1.199	1.198	1.193	+1.176*	+1.224*
+200	0.800	0.799	0.795	+0.784*	+0.816*
+100	0.400	0.399	0.397	+0.392*	+0.408*
ZERO	0.003	0.000	-0.003	-0.020	+0.020
-100	-0.400	-0.401	-0.401	-0.408*	-0.392*
-200	-0.798	-0.800	-0.800	-0.816*	-0.784*
-300	-1.198	-1.199	-1.198	-1.224*	-1.176*
-400	-1.597	-1.599	-1.596	-1.632*	-1.568*
-500	-1.996	-1.998	-1.994	-2.040*	-1.960*
-600	-2.395	-2.397	-2.393	-2.448*	-2.352*
-700	-2.795	-2.797	-2.791	-2.856*	-2.774*
-800	-3.194	-3.196	-3.189	-3.264*	-3.136*
-1000	-3.994	-3.995	-3.986	-4.0 Nominal	

## SCHONSTEDT INSTRUMENT COMPANY

SAM-63B-7

Ithaco P/N C188168

Serial No. 4494TEMP. 50°CInput Voltage: +10  $\pm 0.1$  VDC  
-10  $\pm 1.0$  VDC

FIELD Moe	OUTPUT SIGNAL VDC			LIMITS, VDC	
	X	Y	Z	Min.	Max.
+1000	3.991	3.986	3.978	+4.0 Nominal	
+800	3.192	3.198	3.182	+3.136*	+3.264*
+700	2.793	2.790	2.784	+2.744*	+2.856*
+600	2.395	2.392	2.386	+2.352*	+2.448*
+500	1.996	1.993	1.988	+1.960*	+2.040*
+400	1.597	1.594	1.591	+1.568*	+1.632*
+300	1.198	1.195	1.193	+1.176*	+1.224*
+200	0.799	0.797	0.795	+0.784*	+0.816*
+100	0.401	0.398	0.397	+0.392*	+0.408*
ZERO	0.001	-0.001	-0.001	-0.020	+0.020
-100	-0.397	-0.401	-0.400	-0.408*	-0.392*
-200	-0.796	-0.799	-0.797	-0.816*	-0.784*
-300	-1.195	-1.197	-1.195	-1.224*	-1.176*
-400	-1.594	-1.596	-1.593	-1.632*	-1.568*
-500	-1.992	-1.995	-1.991	-2.040*	-1.960*
-600	-2.392	-2.394	-2.388	-2.448*	-2.352*
-700	-2.791	-2.792	-2.786	-2.856*	-2.774*
-800	-3.190	-3.191	-3.184	-3.264*	-3.136*
-1000	-3.988	-3.988	-3.980	-4.0 Nominal	

TEMPERATURE TEST

TEST No. \_\_\_\_\_

PS 100292

## SCHONSTEDT INSTRUMENT COMPANY

SAM-63B-7

Ithaco P/N C188168

Serial No. 4494TEMP. 0°CInput Voltage: +10  $\pm 0.1$  VDC  
-10  $\pm 1.0$  VDC

FIELD Moe	OUTPUT SIGNAL VDC			LIMITS, VDC	
	X	Y	Z	Min.	Max.
+1000	3.992	4.014	3.974	+4.0 Nominal	
+800	3.195	3.211	3.176	+3.136*	+3.264*
+700	2.797	2.812	2.778	+2.744*	+2.856*
+600	2.398	2.413	2.379	+2.352*	+2.448*
+500	1.999	2.014	1.981	+1.960*	+2.040*
+400	1.600	1.615	1.582	+1.568*	+1.632*
+300	1.201	1.215	1.183	+1.176*	+1.224*
+200	0.801	0.811	0.784	+0.784*	+0.816*
+100	0.402	0.413	0.385	+0.392*	+0.408*
ZERO	0.003	0.013	-0.005	-0.020	+0.020
-100	-0.397	-0.387	-0.414	-0.408*	-0.392*
-200	-0.795	-0.787	-0.812	-0.816*	-0.784*
-300	-1.195	-1.186	-1.211	-1.224*	-1.176*
-400	-1.594	-1.585	-1.609	-1.632*	-1.568*
-500	-1.993	-1.984	-2.008	-2.040*	-1.960*
-600	-2.392	-2.383	-2.407	-2.448*	-2.352*
-700	-2.791	-2.782	-2.806	-2.856*	-2.774*
-800	-3.190	-3.180	-3.204	-3.264*	-3.136*
-1000	-3.988	-3.977	-3.978	-4.0 Nominal	

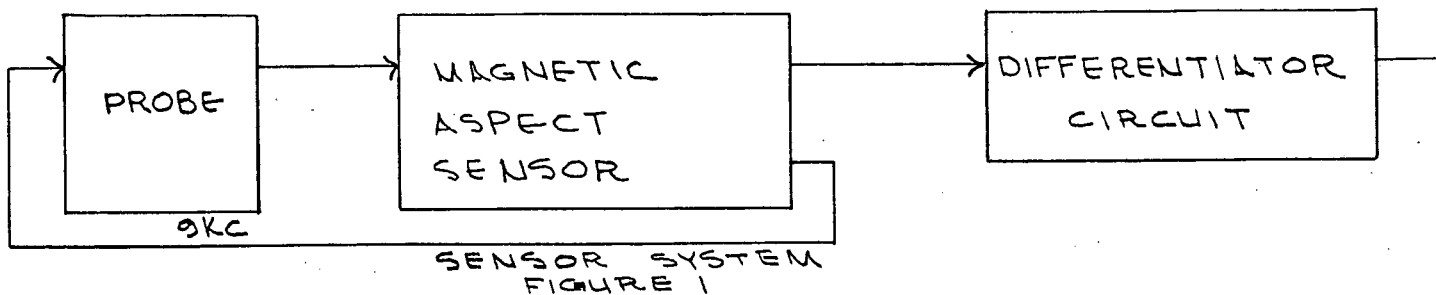
### 3.0 Magnetometer noise measurements

One concern in the designs of this magnetic acquisition system was whether or not available magnetometers have sufficient sensitivity to be able to detect the very low fixed rates required. Three of the Schonstedt RAM5C-NB Magnetometers were purchased and evaluated, using circuitry similar to the differentiators that will be used in the final hardware. The results of these tests are given in the following report no. 90293.

## MAGNETOMETER NOISE MEASUREMENTS

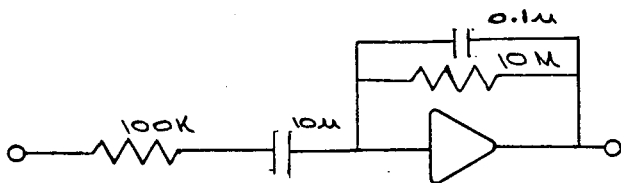
### PURPOSE OF THE STUDY

This study is part of an attempt to detect apparent changes in the earth magnetic field from a satellite during initial attitude acquisition. A system designed to accomplish this (Figure 1) consists of the Schonstedt RAM-5C-NB Magnetometer followed by a differentiator circuit. The output of the differentiator would be fed to a threshold detector of an attitude control system. This report evaluates the noise type and levels present in the magnetometer-differentiator combination.



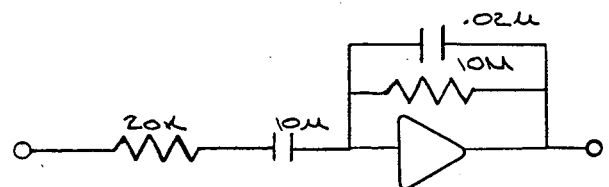
### GENERAL OPERATION OF THE MAGNETOMETER-DIFFERENTIATOR

The proposed magnetic aspect system (Figure 1) is composed of a probe and associated electronics (Magnetic Aspect Sensor) purchased from Schonstedt, and a differentiator circuit. The sensor provides a "d.c." output voltage proportional to the component of the magnetic field coaxial with the probe. The differentiator circuit not only differentiates, but provides attenuation over a range of frequencies outside of the range of vehicle rotation frequencies. Primarily, two circuits were used during the study, one with a corner frequency  $\omega_c$  of 1 radian per second and the other with a corner frequency of 5 radians per second. The approximate equivalent circuits are shown in Figure 2.



DIFFERENTIATOR WITH  $\omega_c = 1$

FIGURE 2a



DIFFERENTIATOR WITH  $\omega_c = 5$

FIGURE 2b

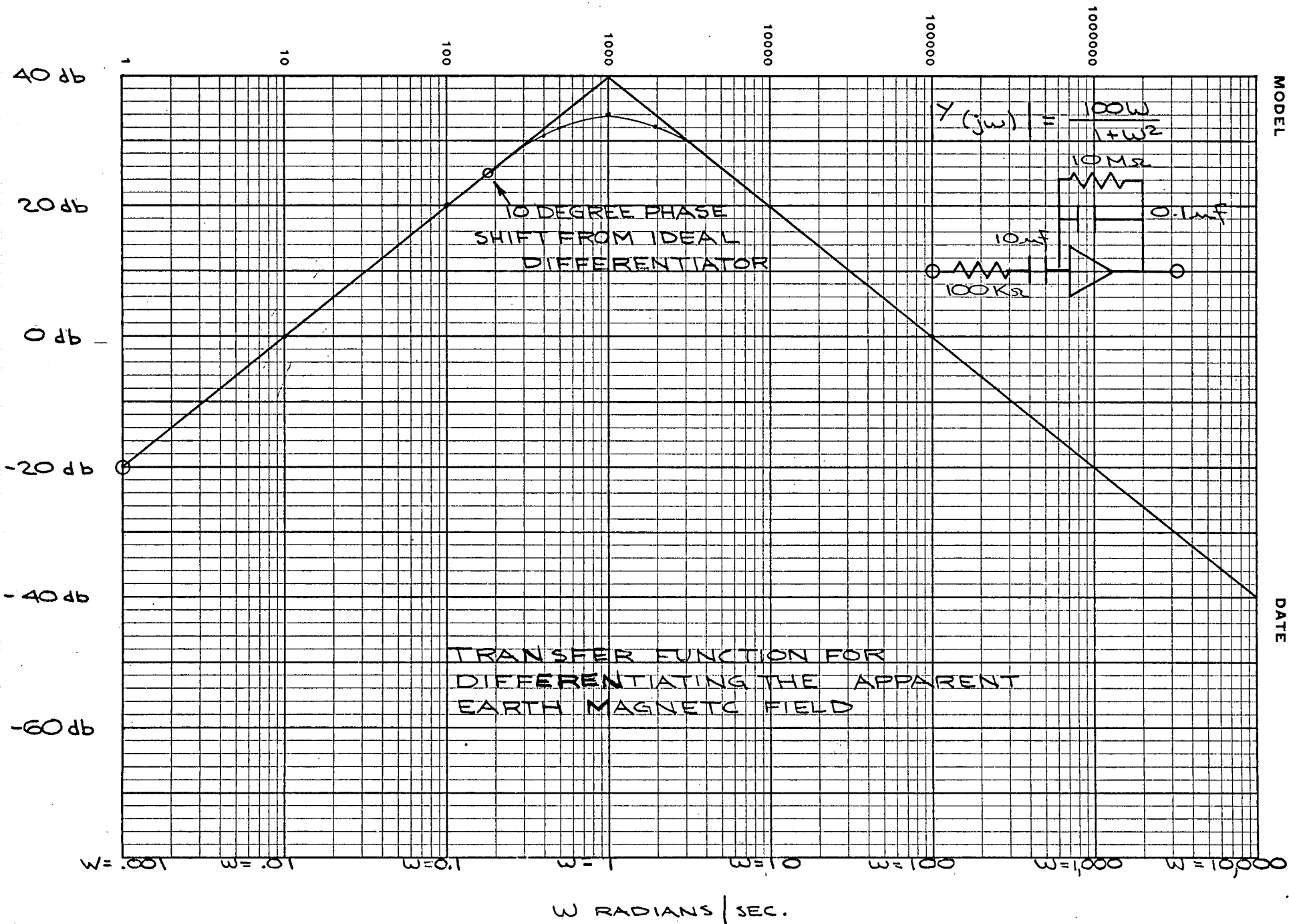


FIGURE 3.

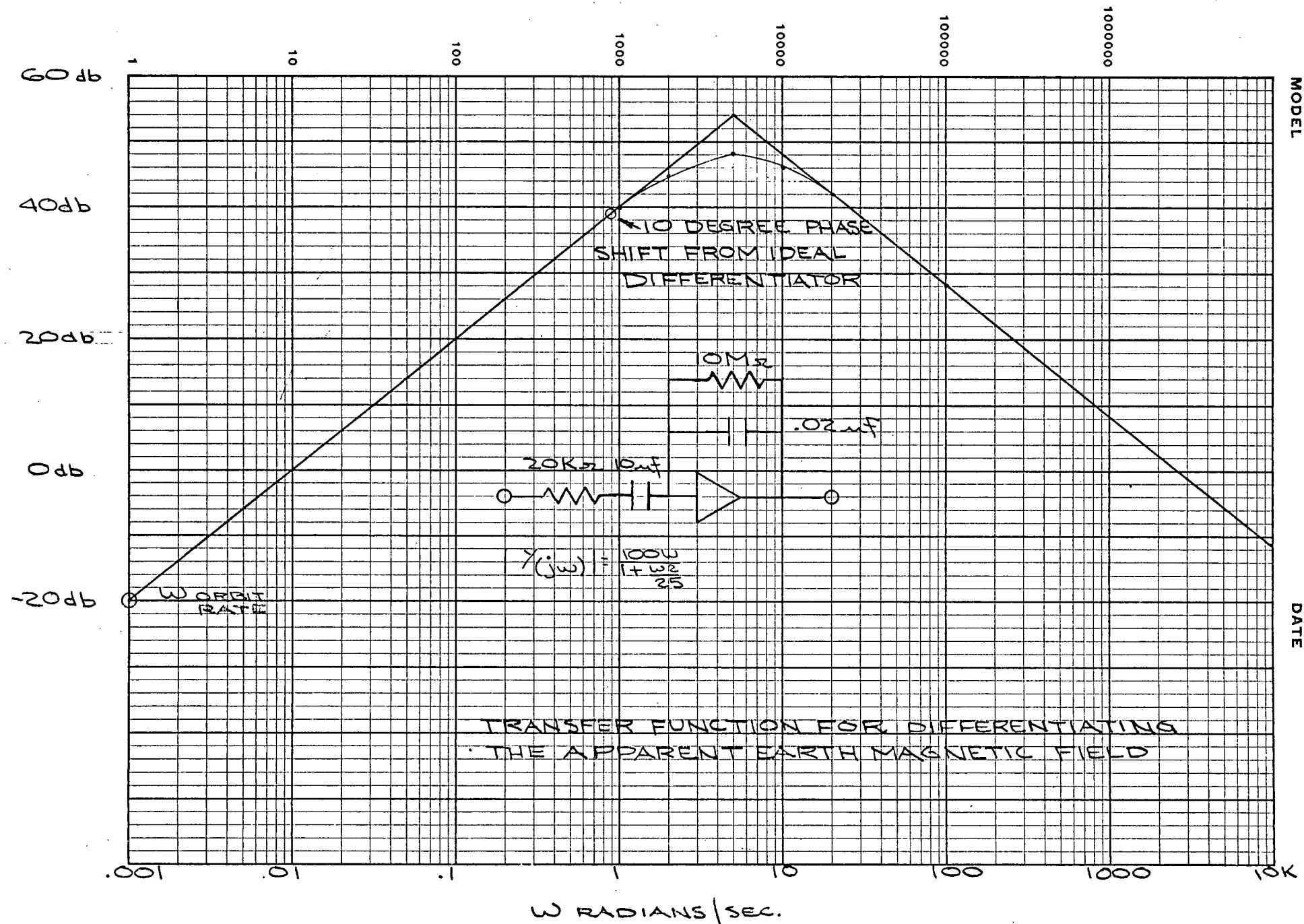


FIGURE 3b



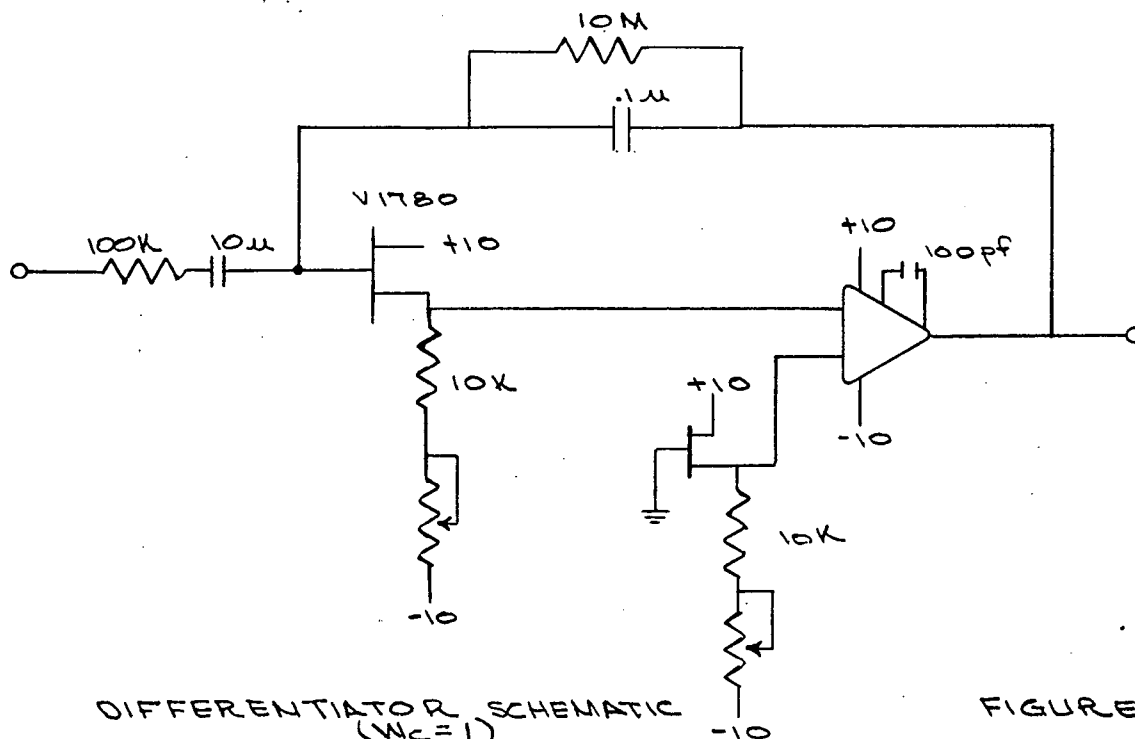
The mathematical representation is

$$Y(jW) = \frac{-j100W}{(1+j\frac{W}{W_C})^2} \quad ; W \text{ is in radians per second}$$

Figures 3a and 3b are the Bode plots corresponding to the circuits of Figures 2a and 2b. Zero db is defined equivalent to unity gain.

#### TEST RESULTS

Figure 4 is the actual circuit configuration of the differentiator with 1 radian/sec. corner frequency. Separate FET's were used. The circuit with a corner frequency of 5 radians/sec. employed the 2N3922 dual FET's.



Three magnetometers SN3881, 3882, and 3883 were used at various times during the testing; but for consistency, 3883 was subjected to each test.

The outputs of the  $W_C=1$  and  $W_C=5$  circuits were measured when these circuits were used in combination with magnetometer 3883. The two tests were not run simultaneously. The magnetometer was centered radially in a wooden cylinder which in turn was centered radially in an iron pipe. The pipe was then closed. A magnet external to the pipe supplied the magnetic field. The magnet produced a 2.3 volt magnetometer output. The output of the differentiators were recorded using a Brush recorder.

The peak to peak values obtained are

8mV for the  $W_C = 1$  circuit,  
80mV for the  $W_C = 5$  circuit.

Figures 5a and 5b are samples of the recordings from which the values were obtained.

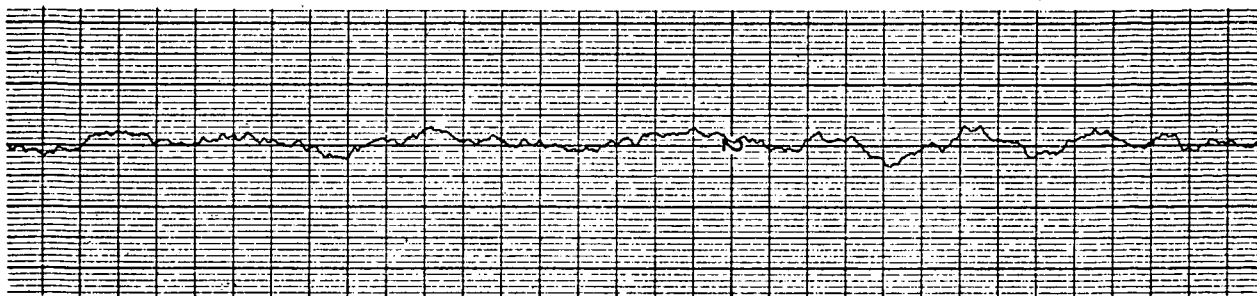
To determine the noise generated by the differentiator circuit, the output was measured with the input shorted. Both circuits were placed in a metal box and the outputs simultaneously measured using the Brush recorder. The peak to peak output was half a millivolt for the  $W_C = 1$  and 2 millivolts for the  $W_C = 5$  circuit.

The magnetometers themselves do not have identical noise characteristics. Figure 6 is a Brush recording showing the noise output from the  $W_C = 5$  circuit fed by each of the three magnetometers. Each of the magnetometers was tested in the pipe with the magnet supplying the same field in each case. A considerable difference between the noise levels of the magnetometers is apparent. Disturbances, some deliberately created, in the laboratory verify that the magnetometers and the differentiator were functioning during the measurements.

Two magnetometers, each in combination with a  $W_C = 1$  differentiator were tested simultaneously to show that spikes which were being observed on the oscioolgraph are not internally generated. Oscillographs obtained during the night hours also tend to confirm that the largest spikes are not internally generated. The night graphs are almost without the large spikes which are common in the data taken during normal working hours.

Oscillographs were run for 1 hour with the  $W_C = 1$  differentiator and then for 1 hour with the  $W_C = 5$  differentiator. These recordings show that noise with a period on the order of minutes is negligible by comparison with the amplitude of the noise envelope.

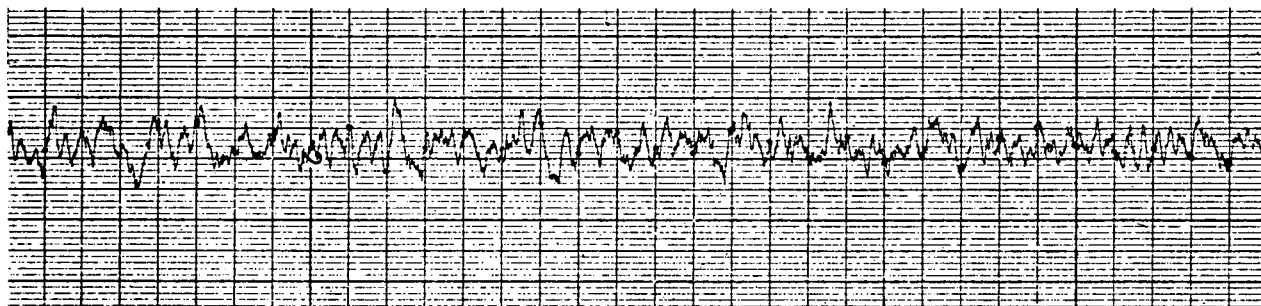
Root-mean-square (RMS) measurements were obtained to indicate the general level of the noise as a function of  $W_C$ . The measurements were obtained graphically from the Brush oscillographs. Three circuits were used in turn with magnetometer 3883. The magnetometer was enclosed in the pipe and the field supplied by a magnet external to the pipe. All three differentiators were of the same mathematical form, all had  $K = 100$ , and all had the same input capacitor and output resistor. With those restrictions, the noise levels may be considered to be a function of  $W_C$ . The equivalent circuits for two of the differentiators are Figures 2a and 2b, the third ( $W_C = 0.5$ ) is shown by Figure 7.



Vertical Scale: 1mV/small div.  
Horizontal Scale: 5mm/sec.

Noise Output of Differentiator with  $W_C = 1$  rad/sec. in  
Combination with Magnetometer SN 3883.

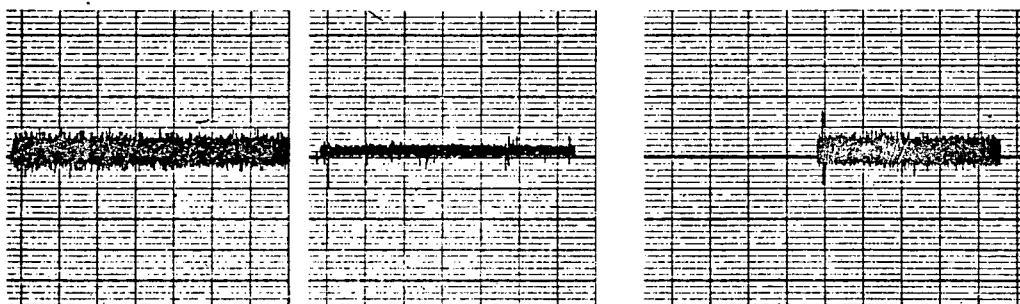
FIGURE 5A



Vertical Scale: 5mV/small div.  
Horizontal Scale: 5mm/sec.

Noise Output of Differentiator with  $W_C = 5$  rad/sec. in  
Combination with Magnetometer SN 3883.

FIGURE 5B



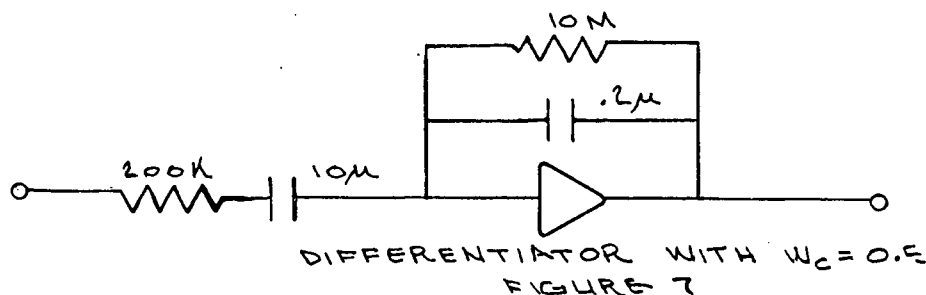
3882

3881

3883

Comparison of Noise Levels from Three Magnetometers.  
Output of Differentiator with  $W_C = 5$  rad/sec.

FIGURE 6



The results of the graphical analysis are given in Table 1.

$W_c$ radian/sec.	Magnetometer 3883 Output Volts d.c.	Differentiator Output Noise Millivolts RMS
0.5	1.6	0.6
1.0	2.3	1.3
5.0	2.3	8.1

TABLE 1

To obtain the RMS voltage graphically, the instantaneous value of the noise voltage is measured at 1 second intervals. The square root of the mean of the square of these measurements is the RMS voltage.

#### MAGNETOMETER OUTPUT CHARACTERISTICS

Tests show that the d.c. output impedance of the magnetometer is 3.6K ohms. The 20K ohm resistance shown in Figure 2b actually includes the 3.6K ohm output impedance.

At a frequency of  $W_c = 0.5$  radian/sec., the impedance of the 10μ farad differentiator input capacitor is 200K ohms, so there is negligible loading from d.c. to  $W = 0.5$  radian/sec.

Discussions with the vendor indicate that no electrical isolation problems exist in connection with the output of the magnetometers.

#### CONCLUSIONS

To get some idea of the feasibility of using the particular magnetometer-differentiator combination studied, some assumptions of physical conditions will be made.

For purposes of this study, a satellite will be assumed in a 500 mile high circular orbit. The RAM-5C magnetometer has a sensitivity of 4 volts per oersted. Assuming a maximum sea level field strength of 580 milligauss in the orbit plane, and an inverse cube variation of field strength with orbit radius; a voltage of  $\approx 1.6$  volts maximum would be present at 500 miles.

The Bode plots, Figure 3, give the voltage gain of the corresponding differentiators as a function of the frequency of a sinusoidal input. For simplicity, assume the satellite to be rotating about an axis which is fixed relative to the earth. Assume we are interested in rotation frequencies from 0.5 radians/sec. down to the orbit rate, and assume the orbit frequency is .001 radian/sec.

According to the Bode plots, a magnetometer signal at the orbit frequency would be attenuated by a minimum of 20db. For the 500 mile orbit, the peak differentiator output would be a maximum of  $\pm 160\text{mV}$ . If the angle between the magnetometer probe and the orbit plane were such as to reduce the field strength by a factor of 0.1, then the signal would be attenuated another 20db and the peak output of the differentiator would be  $\pm 16\text{mV}$ .

Suppose threshold detectors to be at the output of the differentiator. Based on the above discussion, the threshold levels might be set between  $\pm 16\text{mV}$  and  $\pm 160\text{mV}$ . Recall that the peak to peak noise values recorded on the oscillograph were

8mV for the  $W_C = 1$  circuit,  
80mV for the  $W_C = 5$  circuit.

The oscillographs show that the noise level measured at the output of the differentiator is dependent on the d.c. output voltage of the magnetometer. The reason is not known.

The study does not conclusively define the limitations of this particular magnetometer-differentiator combination. However, based on the measurements, the prospects for this combination appear promising.

## MAGNETOMETER NOISE MEASUREMENTS

Addendum to Report No. 90293, Aug. 27, 1971

Report No. 90293 gives the results of noise measurements for the Schonstedt RAM-5C-NB Magnetometer in combination with a differentiator circuit. As mentioned in that report, the noise level measured at the output of the differentiator is dependent on the d.c. output voltage of the magnetometer.

Oscillographs of the noise at the output of the magnetometer itself shows a dependence on the d.c. output voltage of the magnetometer. To obtain this more recent data, magnetometer 3883 was enclosed in the iron pipe and a constant magnetic field supplied by a magnet external to the pipe. The output of the magnetometer was coupled to the preamp of the Brush Recorder through a 10 $\mu$ f capacitor. Samples of these recordings are presented in the Figure.

A close look at the oscillographs show the noise level to be higher for a magnetometer output voltage of -2.4V d.c. than for an output voltage of +2.4V d.c. Since all of the data in Report No. 90293 was obtained for positive output voltages, the following question arises. If data were taken for negative and positive instead of just positive output voltages, might magnetometer 3881 be found to have greater p-p noise than 3883, instead of the other way around. To resolve this doubt, 3881 was tested in combination with the  $W_C = 5$  differentiator; the magnetometer was enclosed in the pipe and the field supplied by a magnet external to the pipe.

The following table shows the p-p differentiator output noise as a function of magnetometer output voltage. The data is only approximate due to the difficulty of defining p-p noise. However, this data clearly shows that the noise levels are well below the 80mV p-p measured with 3883.

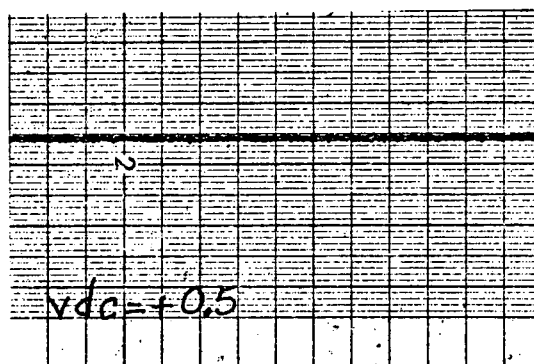
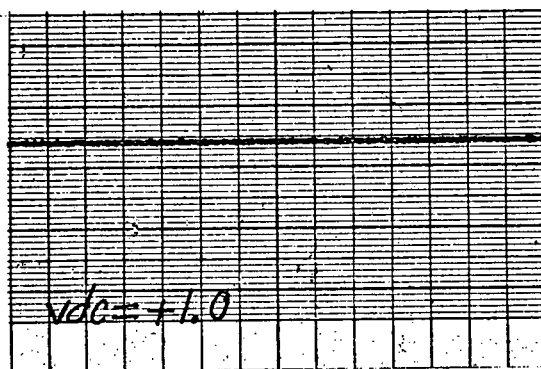
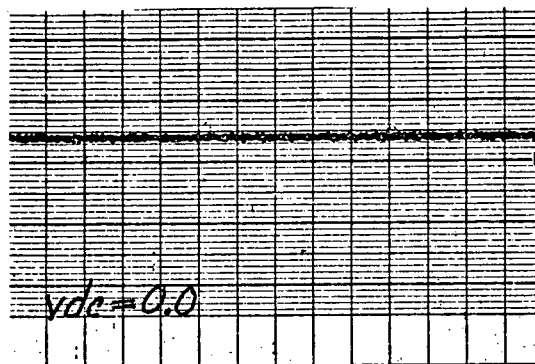
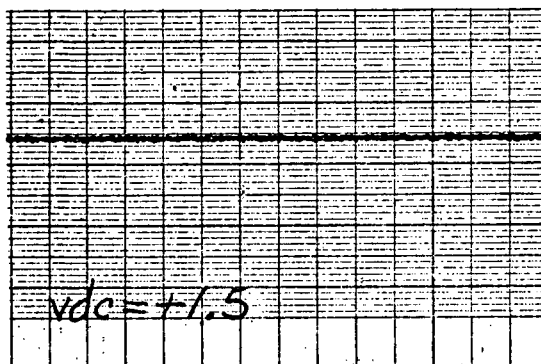
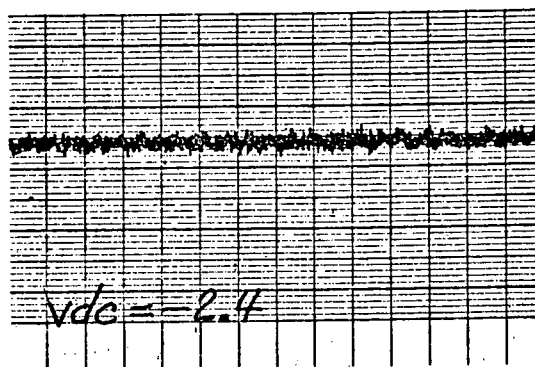
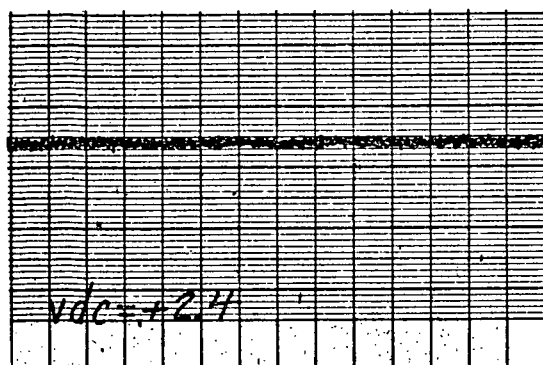
Differentiator Output Noise vs Magnetometer 3881 DC Output

Magnetometer Output Volts DC	$W_C=5$ Differentiator Noise Output Millivolts p-p
-2.4	25
-2.0	25
-1.0	14
0.0	9
+1.0	20
+2.0	19
+2.4	35

## CONCLUSIONS

Noise levels vary from magnetometer to magnetometer. Noise levels also vary with field strength. Finally, and most important, if rates on the order of orbit rates are to be detected, the results of the tests with the  $W_C = 5$  differentiator are inconclusive. Simulation will be needed to provide the answer. However, if a relay were installed to convert the  $W_C = 5$  differentiator to a  $W_C = 1$  differentiator during acquisition, detection at orbit rates should be feasible.

Jay Levy  
ITHACO, Inc.  
735 W. Clinton Street  
Ithaca, New York 14850



horizontal scales:  
20mm/sec.  
vertical scales:  
1mV/small division

Output Noise Voltage for Various DC Output Voltages for  
Magnetometer S/N 3883



Current (Rm Temp)	+	-	
	44ma	25ma	
Orthogonality	X	Y	Z
	27mvp-p	4mvp-p	31mvp-p
Noise	X		
	7mvp-p	8mvp-p	8mvp-p

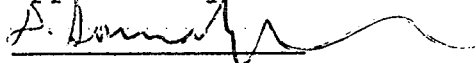
## APPENDIX

### A Magnetic Control System for Attitude Acquisition

A MAGNETIC CONTROL SYSTEM  
FOR ATTITUDE ACQUISITION

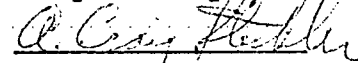
Contract No: NAS5-21649  
Prepared For: Goddard Space Flight Center  
Technical Officer: Marty Lidston (Code 733)

Approved by:



David Sonnabend  
Program Manager

Prepared by:



A. Craig Stickler  
Systems Analyst

ITHACO, Inc.  
735 W. Clinton Street  
Ithaca, New York 14850  
(607) 272-7640  
TWX 510-255-9307

February 22, 1972

Report No. 90345

File No. 10-2460

Approval RF

## ABSTRACT

## A Magnetic Control System for Attitude Acquisition

This report describes a spacecraft magnetic attitude acquisition system that is capable of automatically despinning a satellite from arbitrarily high rates around any axis, and provides terminal orientation that makes capture by conventional fine control attitude control systems routine. The system consists of a 3-axis magnetometer, a set of 3 orthogonal magnets, and appropriate control logic. No earth sensor is required.

Acquisition is treated in two phases. During the despin phase we are concerned with removing the tumbling motion of the satellite. In this phase the performance of the system is unaffected by the presence or absence of a momentum wheel. Phase 2, that of orienting the spacecraft to the desired attitude, requires that a momentum bias wheel be present. In the terminal orientation, the axis of the momentum wheel is substantially perpendicular to the orbit plane (roll and yaw errors near zero) and the pitch rate of the satellite is at twice orbit rate.

This report describes the analysis and simulation that has been done in evaluating the performance of this system. A well-configured system will result in despin times of the order of 5 orbits per RPM for spacecraft in low earth orbits. Following despin, terminal orientation is achieved after another one to three orbits, depending on the capture range of the associated fine control system.

While this report does not describe the physical hardware, the system can be implemented inexpensively with weight less than 5 lbs. and power of about 3 watts.

*A. Craig Fleck*

CAST OF CHARACTERS  
(In Order of Appearance)

$\vec{v}$	A vector (general)
$v$ or $ \vec{v} $	Magnitude of that vector
$v_i$	$i$ th component of $\vec{v}$
$\vec{I}$	Inertia tensor
$I_i$	Moment of inertia about $i$ th coordinate axis
$\vec{\tau}$	Torque
$\vec{H}$	System total angular momentum
$\vec{\omega}$	Angular velocity
$\vec{h}$	System angular momentum contribution from wheels
$T$	Kinetic energy
$\vec{M}$	Magnetic dipole moment
$\vec{B}$	Magnetic flux density
$\omega_0$	Orbital rate
$\vec{e}_n$	Unit vector along the orbit normal
$K, \alpha$	Constants
$\Delta t$	Time intervals
$\vec{P}_0$	Initial spin momentum (not due to wheels)
$T_{sys}$	A parameter
$\Omega$	Angular velocity
$\delta x$	A "small" change in $x$
$I_{3e}$	An equivalent moment of inertia about the 3 axis. Defined by Eq. (C7)
$\alpha_1, \alpha_2$	Defined by Eq. (E10) & (E11)
$A$	A matrix (page E-2 & E-3)
$\vec{x}(t)$	A vector whose components are $\{\delta\omega_1, \delta\omega_2, \delta B_1, \delta B_2\}$
$s$	The Laplace Operator
$\vec{X}(s)$	Laplace transform of $\vec{X}(t)$
$L^{-1}$	Inverse Laplace transform

## TABLE OF CONTENTS

	Page
LIST OF SYMBOLS.....	i
INTRODUCTION.....	1
SIMULATED SATELLITE.....	2
DESCRIPTION OF PROBLEM.....	2
EQUATIONS OF MOTION.....	3
CONTROL THEORY.....	4
TERMINAL ORIENTATION.....	6
STABILITY CONSIDERATIONS.....	7
SYSTEM PERFORMANCE.....	9
RECOMMENDATIONS FOR FURTHER WORK.....	12
BIBLIOGRAPHY.....	13
APPENDIX B.....	PROGRAM LIST
APPENDIX C.....	DUAL SPIN STABILITY
APPENDIX D.....	SYSTEM EQUILIBRIUM POINTS
APPENDIX E.....	SYSTEM STABILITY

## INTRODUCTION

In this report we will be concerned with the description and evaluation of a magnetic acquisition/attitude control system. The work described here has been performed during the last several months, principally by the author, with the assistance and guidance of Messrs. David Sonnabend, and Robert Fowler. This work was done under contract #NAS5-21649, at the behest of the Systems Analysis Branch, GSFC, Greenbelt, Maryland. The original concept of this system was suggested by Seymour Kant, Head, Systems Analysis Branch, GSFC.

The attitude control system described here is designed to "despin" a satellite and then orient it to any preferred Earth referenced attitude. This is done thru interaction with the Earth's magnetic field. An interesting feature of the system is that it requires no Earth sensor.

In this report we will discuss the control law for despinning the satellite and the mechanism thru which some preferred attitude is attained. Then we will discuss stability considerations as they apply to this system. Next, system performance is evaluated in the light of both analytical results and simulation results. We will be concerned with both despin and attitude acquisition performance. Finally, some recommendations for further study are included in case any parties might wish to continue the work discussed here.

Appendix B displays a listing of the FORTRAN program used in the digital simulation. Appendix C reviews some of the dynamic stability theory for dual spin satellites, for convenient reference, but does so in a different fashion than is usually employed. The results obtained are, of course, the same as usual. In Appendix D we analyze the equilibrium points of our system; the stability of these points is briefly treated in Appendix E, using some of the results of Appendix C.

The author wishes to make one further remark before continuing. The (differential) equations describing the behavior of the system discussed herein are nonlinear and otherwise intractable. This being the case, it is not possible to obtain explicit analytical solutions and recourse to simulation must be made. Much of the results presented here were obtained via a digital simulation model. A program, previously written by the author and noted in the references (1), was used to this end. A listing of this program, and an index of computer runs, may be found in the appendices. A brief description of the simulated satellite is contained in the following section.

## SIMULATED SATELLITE

Most of the simulation runs dealt with a satellite with the following characteristics: (1) moments of inertia of  $47.5\text{Kg-m}^2$  ( $35\text{ slug-ft}^2$ ),  $67.9\text{Kg-m}^2$  ( $50\text{ slug-ft}^2$ ), and  $33.9\text{Kg-m}^2$  ( $25\text{ slug-ft}^2$ ) about, respectively, its yaw, roll and pitch axes; (2) a pitch momentum bias of  $0.944\text{ Nt-m-sec}$  ( $0.7\text{ lbf-ft-sec}$ ); and (3) switchable control magnets of  $10^4$  pole-cm strength. There are three such magnets, one each along the yaw, roll and pitch axes. We again note that these are principal axes for the satellite. This satellite is in a circular low altitude orbit with a period of approximately 100 min. We note however, that these parameters of orbit and vehicle are of no special significance, but were chosen merely to implement the digital simulation.

## DESCRIPTION OF PROBLEM

In general, a satellite injected into orbit will be observed to be tumbling about with a certain residual angular velocity. This is so in spite of efforts made to release it "gently". Various devices have been utilized to dissipate this residual motion. In our case, the satellite will be launched by a spin stabilized rocket and hence will be inserted into orbit with an angular velocity of roughly 100 RPM about some (known) axis. A simple mechanism (a yo-yo) will then reduce that spin to the order of 1-10 RPM. However, this rate is, in general, still so high as to prevent the basic attitude control system from locking onto some target (the Earth, sun, stars, etc.). A further spin rate reduction is required, preferably to say 0.1 RPM or less. To this end, such active devices as rate gyros, accelerometers, and magnetometers coupled to gas jet systems, and passive devices such as eddy current and magnetic hysteresis rods have been employed.

Reverting to general terms, then, there are two distinct phases of the attitude acquisition procedure. The first is despin, of which we have just spoken, and the second is an attitude orientation phase which facilitates capture by the basic control system.



## EQUATIONS OF MOTION

The equations describing the rotary motion of a satellite (or any other rigid body) are most conveniently written for a set of body fixed principal axes. They are the well known Euler's Equations of Motion, with terms added to account for momentum wheels. To wit,

$$\bar{\tau} = \frac{d^{SPACE}}{dt}(\bar{H}) = \frac{d^{BODY}}{dt}(\bar{H}) + \bar{\omega} \times \bar{H} \quad (1)$$

$$\text{where } \bar{H} = \bar{I} \cdot \bar{\omega} + \bar{h} \quad (1')$$

or, in scalar form

$$\tau_1 = \dot{h}_1 + I_1 \dot{\omega}_1 + \omega_2 h_3 - \omega_3 h_2 + \omega_2 \omega_3 (I_3 - I_2) \quad (1a)$$

$$\tau_2 = \dot{h}_2 + I_2 \dot{\omega}_2 + \omega_3 h_1 - \omega_1 h_3 + \omega_1 \omega_3 (I_1 - I_3) \quad (1b)$$

$$\tau_3 = \dot{h}_3 + I_3 \dot{\omega}_3 + \omega_1 h_2 - \omega_2 h_1 + \omega_1 \omega_2 (I_2 - I_1) \quad (1c)$$

The reader is cautioned that great care should be exercised if these axes are not right handed. As mentioned above, these axes are principal axes passing thru the center of mass. Here, the  $I_i$  are the moments of inertia about the  $i$ th coordinate axis,  $\bar{\tau}$  is the applied torque, and  $\bar{h}$  is the momentum contribution of the wheels.

# CONTROL THEORY

As noted above, the attitude acquisition system performs two principal functions. The first is despinning the tumbling satellite, and the second consists of providing some preferred orientation. Consider the former.

The rotational kinetic energy of the satellite, not including that of any reaction wheels, is

$$T = \frac{1}{2} \sum_i I_i \omega_i^2 \quad (3)$$

We would like to diminish this quantity.

$$\frac{d}{dt} (T) = \dot{T} = \sum_i I_i \omega_i \dot{\omega}_i = \bar{\tau} \cdot \bar{\omega} \quad (4)$$

where  $\bar{\tau}$  is the external torque acting on the satellite, and  $\bar{\tau} \cdot \bar{\omega}$  is the rate at which work is done on the satellite. For a dipole  $\bar{M}$  in a magnetic field  $\bar{B}$ , the torque exerted by the field on the dipole is

$$\bar{\tau} = \bar{M} \times \bar{B} \quad (5)$$

Combining (4) & (5)

$$\dot{T} = \bar{M} \times \bar{B} \cdot \bar{\omega} = \bar{B} \times \bar{\omega} \cdot \bar{M} \quad (6)$$

Now consider the quantity  $\frac{d^{BODY}}{dt}(\bar{B})$

$$\frac{d^{SPACE}}{dt}(\bar{B}) = \frac{d^{BODY}}{dt}(\bar{B}) + \bar{\omega} \times \bar{B} \quad (7)$$

Suppose  $\frac{d^{SPACE}}{dt}(\bar{B}) = \bar{0}$ . That is, we say that this term is negligible in comparison with the other two terms. Then (7) becomes

$$\frac{d^{BODY}}{dt}(\bar{B}) = \bar{B} \times \bar{\omega} \quad (8)$$

Substituting in (6) we obtain

$$\dot{T} = \dot{\bar{B}} \cdot \bar{M} \quad (9)$$

The desired control scheme is now clear. We must simply measure  $\dot{\bar{B}}$  along any axis in the satellite, and then change the polarity of a magnet lying along that axis, keeping the sense of  $\bar{M}$  opposite that of  $\dot{\bar{B}}$ . This insures  $\dot{T} \leq 0$  and decreasing  $T$ . The limitations of such a

scheme are also clear. Equation (9) is valid only when (8) is valid, that is, if  $\frac{d^{SPACE}(\bar{B})}{dt}$  is truly negligible in comparison with  $\bar{\omega} \times \bar{B}$ . Now,  $\bar{B}$  varies in inertia space as  $\sin 2\omega_0 t$ , where  $\omega_0$  is the orbital frequency. Thus,  $\frac{d^{SPACE}(\bar{B})}{dt}$  is equivalent to a body rate of  $2\omega_0$ , and as long as  $\bar{\omega}$  is, say, an order of magnitude greater than  $2\omega_0$  (about 0.002 rad/sec for low altitude orbits), we may safely neglect  $\frac{d^{SPACE}(\bar{B})}{dt}$ .

For reasons which will become clear later, the chosen control configuration involves three magnets. These lie along the principal axes of the vehicle and are controlled by magnetometers (which measure the field component) along these same axes. The controller operates in a flip-flop manner, switching the magnets' polarity to keep the  $M_i$  opposite in sense to  $\dot{B}_i$ , as measured by magnetometers on board the satellite.

## TERMINAL ORIENTATION

We now consider the second phase of attitude acquisition, orientation. We wish to attain some particular attitude. As long as this preferred orientation is with respect to the Earth, any desired attitude may be attained. In this section we will confine our discussion to a satellite having only a pitch momentum bias. Other momentum wheels, if any, are not yet activated at this point. The arguments advanced below are not as rigorous as might be desired but it is felt that their physical appeal more than compensates for that.

Consider the satellite to be orbiting the Earth at angular rate  $\omega_0$ , and assume also that it has been completely despun. Then it must be that the satellite interprets this situation as though it were spinning backwards at angular velocity  $-2\omega_0\bar{e}_n$ , where  $\bar{e}_n$  is a unit vector normal to the plane of orbit (and whose sense is determined by the direction of orbit). This is because the satellite senses the Earth's magnetic field passing by it twice per orbit. Note that the trajectory yaw and roll axis components of the Earth's field vary as  $\sin 2\theta$ , where  $\theta$  is the angle into orbit from some reference point. Since the system "senses" an angular velocity whose direction is  $-\bar{e}_n$ , it responds with a corrective torque along the direction  $+\bar{e}_n$ . The net result of such a torque must be to gradually align the system momentum bias (which properly lies along the vehicle pitch axis) with the orbit normal. In this way the proper yaw-roll attitude is attained. It is the fact that the satellite is not spinning at  $2\omega_0$  that results in the net torque along  $\bar{e}_n$  which in turn aligns the momentum bias with the orbit normal. But what if it had been spinning at  $2\omega_0$  originally, or in some way reached this state. It is apparent that this could occur in only two ways. That is, the system momentum must be either parallel or antiparallel to  $\bar{e}_n$ . If this is not so, then a component of this momentum lies in the orbit plane and a body fixed torque, also lying in the orbit plane and of the correct magnitude would be required to force the body to rotate about  $\bar{e}_n$  at  $2\omega_0$ . Where is this torque to come from? The author does not believe in its existence and hence concludes that the system momentum bias must lie parallel or antiparallel to  $\bar{e}_n$  if it is to rotate at  $2\omega_0$ . Both of these situations correspond to equilibrium points. We simply note here that the antiparallel situation is not a stable condition.

Our conclusions are then that the satellite will eventually align its momentum bias axis (in our case, the pitch axis) with the orbit normal and thus provide yaw-roll attitude acquisition. If the reader is not completely convinced of this by the rather un-rigorous arguments advanced here, we reassure him by noting that considerable simulation experience is completely in accord with the above analysis. A further discussion concerning the amount of momentum bias required in the above scheme and the effects of more than one momentum wheel, etc., are reserved for later sections. Refer to the section titled "System Performance" and see Appendix C.

## STABILITY CONSIDERATIONS

The desired action of the control law just developed is, of course, to reduce the angular velocity of the satellite to zero. Such a condition is not, properly, an equilibrium point for our system, since no provision has been made, as of yet, for a null state for the magnets. They are always on, having one polarity or the other, and the satellite always has some angular acceleration, hence the system possesses no equilibrium points. It would be easy however, to insert deadzones in the magnet controllers. Provided these deadzones are large enough to prevent magnet activation due to the relatively small term  $\frac{dSPACE(\bar{B})}{dt}$  in

(7) (which the satellite experiences due to its orbital motion and the rotation of the Earth), then, the condition  $\bar{\omega} = 0$ ,  $\bar{B} = \text{any}$ , is an equilibrium point. If this sort of provision is not made, then it would seem that the satellite should behave in some sort of quasi-oscillatory manner, at small angular rates. That this condition would, once attained, persist, seems quite plausible from the analysis above. It is not, however, a simple matter to talk about equilibrium points and stability. The equations describing this system are quite intractable to ordinary stability analysis. For one thing, the control law is binary. Even if we replace it with a linear law (the first term of its describing function) the resulting system equations consist of six first order nonlinear differential equations; three involve quadratic combinations, the other three cubic combinations of the state variables ( $\omega_1$ ,  $\omega_2$ ,  $\omega_3$ ,  $B_1$ ,  $B_2$ ,  $B_3$ ).

We should note here that if the system has either a binary control law with deadzones or a linear control law (that is,  $\dot{M} = -KB$ ), then there are an infinity of proper equilibrium points. These points belong to one of four distinct classes. However, in order to spare the reader, a discussion of these points and their stability is relegated to Appendix D. Suffice it to say that some of these points (other than  $\omega = 0$ ) can be shown, by analysis, to be neutrally stable. Further, simulation results show that in some domain some of the points are stable.

There are other problems too. We are particularly interested in investigating the existence of any so called "psuedo equilibrium points" (PEP's for brevity). Since  $\frac{dSPACE(\bar{B})}{dt} \neq 0$ , and there are various disturbance torques acting on our satellite, and the system equations are nonlinear, there may be points which are not properly equilibrium (stationary) points but near which the system might "hang up". Here we are talking principally about limit cycle behavior, but must also be concerned with various (as yet unknown) forcing functions.

In view of these difficulties, it was decided that digital simulation was the most suitable tool for evaluating this system. A discussion of the results of this simulation work is reserved for the next section and Appendix E.

Although the actual stability analysis is put off until appendices C and E, the conclusions and implications of those analyses are reviewed here. First, we note that, for a vehicle configured as described in the section "Simulated Satellite" (that is to say, the proposed vehicle), the terminal condition (or behavior) corresponds to a stable equilibrium point. This is, of course, most desirable. We again note that the "upside down" orientation (that is, with the pitch axis flipped over) corresponds to an unstable equilibrium state; this too is soothing. Finally we note that, for our vehicle, a spin rate of up to  $27.8 \times 10^{-3}$  radians/sec. about the pitch axis also may be a stable equilibrium state.

This stability conclusion neglects the fact that the direction of  $\vec{B}$  in space changes as the satellite orbits the Earth. This turns out to be a saving grace. Nonetheless, for strong enough magnets, the satellite may "track" the field. During such a period it is possible that the despin rate may be reduced by as much as a factor of fifty. For this reason it might be advisable to insert a mode switch for disabling the despin system for an eighth orbit or so if it seems as though this has occurred. At the end of that time  $\vec{\omega}$  and  $\vec{B}$  would no longer be parallel and hence the despin system will again perform properly.

## SYSTEM PERFORMANCE

Having convinced the reader (hopefully) that our system works, we now attempt to answer the question - how well? As before, we shall first be concerned with the despin phase.

As the system kinetic energy  $\frac{1}{2} \bar{\omega} \cdot \bar{I} \cdot \bar{\omega}$  tends towards zero (this was assured in the section titled "Control Theory"), so must  $\bar{\omega}$  and the system momentum  $\bar{I} \cdot \bar{\omega}$  (this, of course, excludes the wheels' momenta). In fact, the despin process may be looked on as a reduction of the momentum term  $\bar{I} \cdot \bar{\omega}$  to zero. In the very best case this requires a time  $\Delta t_{\text{opt}}$  given by

$$\Delta t_{\text{opt}} = \frac{|\bar{I} \cdot \bar{\omega}|}{\tau_{\text{max}}} = \frac{|\bar{P}_O|}{MB} \quad (10)$$

Here  $\bar{P}_O = \bar{I} \cdot \bar{\omega}_{\text{init}}$  is the initial momentum of the body other than that due to the wheels. It is useful to consider an "efficiency factor"  $\alpha$ ,

$$\alpha = \frac{\Delta t_{\text{opt}}}{\Delta t_{\text{actual}}} \quad (11)$$

where  $\alpha$  of course lies between zero and one.  $\alpha$  is a function of various parameters, such as  $\bar{\omega}_{\text{init}}$ , the inertia configuration of the satellite, and the altitude and inclination of orbit. That  $\alpha$  is less than one is a reflection of the fact that  $\bar{M}$  is not always perpendicular to  $\bar{B}$  and that  $\bar{\tau}$  does not always lie opposite  $\bar{I} \cdot \bar{\omega}$ .

For a given system configuration ( $\bar{I}$  &  $\bar{M}$ ) and a given orbit and initial conditions (determining  $\bar{\omega}$ ,  $\bar{B}$ ) we should be able to determine  $\alpha$  and hence the time for despin. This was the goal of much of our early simulation, in which various orbits, initial conditions and system configurations were evaluated. This simulation shows that  $\alpha$  generally lies in the range 0.55-0.80. For the worst case, a near equatorial orbit with initial spin along the field vector,  $\alpha$  may be as poor as 0.15-0.20.

Another way to look at the performance of this system is from an energy point of view. Consider, for simplicity, rotation about a single axis.

$$T = \frac{1}{2} I \omega^2 \quad (12)$$

$$\dot{T} = I \omega \dot{\omega} = \omega \tau \quad (13)$$

$$\therefore I \dot{\omega} = \tau = \alpha MB \quad (0 < \alpha < 1) \quad (14)$$

The last of these equations says that  $\omega$ , and the angular momentum  $I\omega$ , are always decreasing. The constancy of this rate of decrease depends on the constancy of  $\alpha$ . We are of course assuming that  $\tau$  has the proper sense.

The attitude acquisition part of the problem is more difficult to analyze. If, for example  $h$  approaches 0 we will not acquire. But also if  $h$  approaches infinity we will acquire, but it will take infinite time. Also, if  $M$  approaches 0 or infinity we will not attain the proper attitude. In view of these considerations it would seem that there might be some ratio of momentum bias to magnet torque which would provide optimum performance. By this we mean both minimum time to acquire and minimum roll-yaw error after acquisition. Consider the parameter

$$T_{sys} = \frac{h}{MB} \quad (15)$$

which has the dimensions of time. It is rather difficult to say anything about this problem analytically, but the following is observed from simulation runs.

We first note that there is a certain minimum bias required for terminal attitude acquisition. It is shown in Appendix C, eq. (C10), that

$$h_0 > \Omega \max(I_1, I_2) \quad (C10)$$

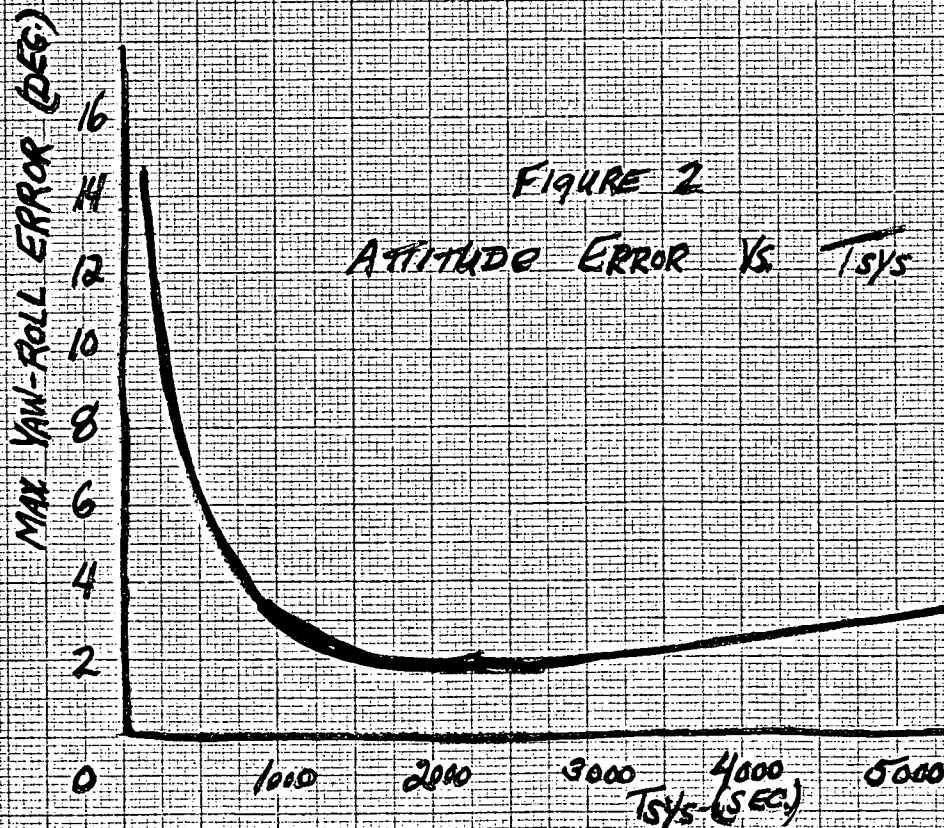
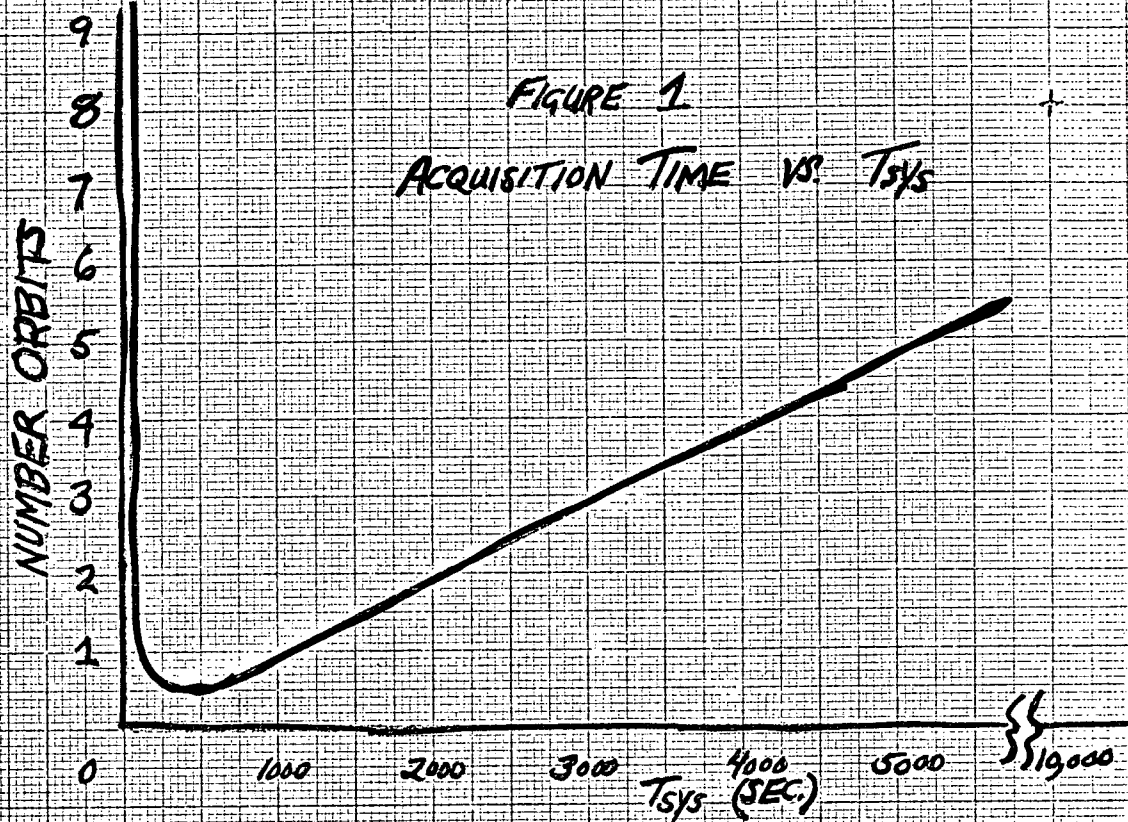
for us,  $h_0 = h + I_3\Omega$  and  $\Omega = 2\omega_0$  (for the terminal condition). Thus (C10) becomes

$$h > 2\omega_0 \{\max(I_1, I_2) - I_3\} \quad (16)$$

For good performance this amount should be exceeded by a factor of four or more. Little is gained by increasing  $h$  beyond this point. If we now choose a particular orbit, the time and quality of acquisition (after despin has been completed) are functions of the magnet strength  $M$ . Acquisition time is also, of course, very much a function of attitude at the conclusion of despin. A (very) qualitative picture of this situation is presented in Figure 1. As pointed out previously, for very weak or very strong magnets we do not attain the desired attitude. The author cannot caution the reader too strongly against taking this curve too literally. Much more work would be needed to get a more exact picture of this phenomena. There are too many variables and too few points on the curve of Figure 1 to let the author rest comfortably. As for the quality of roll-yaw acquisition, it is interesting to note that a curve qualitatively similar to Figure 1 may be used to describe this as well. Figure 2 depicts this situation. Note that the minimum point is shifted to about 2000 secs. (This appears to be significant) and the curve is somewhat flatter. The best that we can do appears to be about  $2^\circ$ . Again, the author cannot over-emphasize the tentative nature of these findings. Considerable work remains to be done in this area.

For a well proportioned system, acquisition times are of the order of one orbit. This being the case, it is expected that optimum performance will generally be defined in terms of quality of roll-yaw acquisition rather than in terms of minimum time to acquire.





## RECOMMENDATIONS FOR FURTHER WORK

The author feels that the work done to date definitely demonstrates the feasibility and desirability of this acquisition control system. Nevertheless, work remains to be done.

There is the matter of system stability. While it seems apparent that there are no stability problems which might interfere with the proper operation of the control system, nonetheless it would be good if we obtained some further analytical results. In particular, an analysis including the effects of the change in  $\bar{B}$  due to orbital motion would be interesting.

As noted, we have not included the effects of disturbance torques on the performance of this system. Their effects on both limit cycle behavior and terminal attitude orientation should be investigated. Their neglect has been justified up to this point by the fact that the magnet torques are at least an order of magnitude greater than the disturbances.

Another area which needs refinement is the magnetic field model used in our simulation. So far, only the simple tilted dipole has been used. The effect of a more accurate field model on terminal attitude orientation needs to be investigated.

More investigation into the effects of deadbands, hysteresis loops, and inhibit controls placed in the magnet control loops would be desirable. There is also the matter of crosstalk between magnets and magnetometers. We must be sure that no unstable loop is set up in which switching magnets trigger magnetometers which in turn cause the magnets to switch again.

One other point which will bear further investigation is the potential of using this acquisition system as a complete attitude pointing system. Used with a pitch reaction wheel scanner and simple pitch control loop we would have complete three axis control. Some studies of pointing accuracies versus various system parameters would be useful in investigating this possibility.

BIBLIOGRAPHY

1. Stickler, A.C., "A General Purpose Digital Program for Solving Problems that Incorporates Euler Homogeneous Parameters", ITHACO Report No. 90288, July 13, 1971.
2. Stickler, A.C., "Variation of the Earth's Magnetic Field as Seen by a Satellite in Circular Orbit", ITHACO Report No. 90295, August 11, 1971.
3. Sonnabend, D., "Satellite Attitude Kinematics", ITHACO Report No. 90290, July 28, 1971.
4. Chen and Haas, Elements of Control Systems Analysis, Prentice-Hall, Englewood Cliffs, New Jersey, 1968.
5. Greenwood, D. P., Principles of Dynamics, Prentice-Hall, Englewood Cliffs, New Jersey, 1965.
6. Velman, J.R., "Attitude Dynamics of Dual Spin Satellites", Hughes Aircraft Company, Space Systems Division, Report No. SSD 60419R, September, 1966.

APPENDIX B

DIGITAL SIMULATION PROGRAM LISTING

This appendix consists of a listing of the digital computer program used to simulate control system/satellite behavior. The program is quite similar to the one discussed in reference 1, and the reader is referred there for a more detailed discussion, flowcharts, etc. Its operation may be briefly summarized as follows.

The main program performs the bookkeeping functions of input/output and maintains overall control. What we are doing here is, essentially, integrating equation (1), specialized for the vehicle described under "Simulated Satellite". This is done through subroutines WDOT and RK4. An additional problem we must deal with here is that the applied torques are functions of the vehicle's attitude. Namely, they are functions of the Earth's magnetic field components as measured in the vehicle. For this reason we must keep track of the vehicle's attitude. This is implemented through the use of Euler Homogeneous parameters in subroutines.EHPQT, NORM, MAT1, and MULVEC. The Earth's magnetic field is first obtained in trajectory axis components (subroutine BFLDS1), and then transferred into body axis components, making use of the direction cosine matrix (subroutine EHPA). Subroutine TORQUE then computes the torques arising from the interaction between this field and the on board magnets. Please note that the subroutine displayed contains neither deadzones nor hysteresis loops, although some subroutines incorporating them have been used at times.

\*JOB

C \*\*\*\*GENERAL PURPOSE KINEMATIC INTEGRATOR PACKAGE USES EULER DAV20001  
 C \*\*\*\*HOMOGENEOUS PARAMETERS IN ORDER TO SOLVE PROBLEMS INVOLVING DAV20002  
 C \*\*\*\*BODY RATE SPECIFIED ROTATION RATES. \*\*\*\*\* DAV20003  
 C \*\*\*\*AUTHOR: ALBERT C. STICKLER DAV20004  
 C \*\*\*\*\* DAV20005  
 C \*\*\*\*MAIN PROGRAM SKELETON. FILL IN DETAILS, PARAMETERS, ETC. \*\*\*\*\* DAV20006  
 C \*\*\*\*ASSEMBLAGE INCLUDES SUBROUTINES NORM, MAT1, RK4, EHPA, DAV20007  
 C \*\*\*\*EHPQT, EANGLE, AND INTERP, AMONG OTHERS \*\*\*\*\* DAV20008  
 C DAV20009

1 REAL I1, I2, I3, QT(4,4), A(3,3), AXIS(3) DAV20010  
 2 REAL\*4 INCLIN, BT(3), BB(3) DAV20011  
 3 COMMON/RK/P(4), W(3), QT, DT, W0 DAV20012  
 4 COMMON/WDOTS/ T(3), COMM(10), C1, C2, C3, C4, C5, C6 DAV20013  
 5 REAL TIME/0.0/, THETA/0.0/, WE/0.41784E-02/ DAV20014  
 6 INTEGER\*4 I/-1/, IHEAD/-1/ DAV20015  
 7 READ(5,90) I1, I2, I3, BIAS, FACTOR DAV20016  
 8 READ(5,90) PRINT, BSTEP DAV20017  
 9 READ(5,90) W DAV20018  
 10 READ(5,90) DT, TRUN DAV20019  
 11 READ(5,90) INCLIN, EARTH, ALT DAV20020  
 12 PERIOD=0.3151263\*SQRT(0.1\*ALT)\*\*3 DAV20021  
 13 WRITE(6,110) I1, I2, I3, BIAS, FACTOR DAV20022  
 14 WRITE(6,111) PRINT, BSTEP DAV20023  
 15 WRITE(6,112) DT, INCLIN, EARTH, ALT, PERIOD DAV20024  
 16 C1=(I2-I3)/I1 DAV20025  
 17 C2=(I3-I1)/I2 DAV20026  
 18 C3=(I1-I2)/I3 DAV20027  
 19 C4=1/I1 DAV20028  
 20 C5=1/I2 DAV20029  
 21 C6=1/I3 DAV20030

C READ AND WRITE INITIAL ATTITUDE DAV20031

22 READ(5,90) P DAV20032  
 23 WRITE(6,91) P DAV20033  
 24 91 FORMAT(/, ' INITIAL EHPS WERE', 4F10.4) DAV20034  
 25 CONST=0.001\*FACTOR DAV20035  
 26 COMM(1)=BIAS\*C4 DAV20036  
 27 COMM(2)=BIAS\*C5 DAV20037  
 28 IBSTEP=BSTEP/360.0\*PERIOD/DT DAV20038  
 29 IPRINT=PRINT DAV20039  
 30 DTHETA=360.0/PERIOD\*DT DAV20040  
 31 CALL BFLDS1(INCLIN, ALT, BT) DAV20041  
 32 CALL BFLDS2(EARTH, THETA, BT) DAV20042  
 33 W0=6.2832/PERIOD DAV20043

34	DTHAF=DT*0.5	
35	50 CALL NORM(P,PMAG)	DAV20044
36	I=I+1	DAV20045
37	IF(I/IPRINT*IPRINT .NE. I) GO TO 75	DAV20046
38	ERROR=PMAG-1.0	DAV20047
39	ENERGY=I1*W(1)*W(1)+I2*W(2)*W(2)+I3*W(3)*W(3)	DAV20048
40	IHEAD=IHEAD+1	DAV20049
41	IF(IHEAD/50*50 .EQ. IHEAD) WRITE(6,101)	DAV20050
42	WRITE(6,100) TIME,W,BB,ERROR,ENERGY,A(1,3),A(2,3)	DAV20051
43	75 TIME=TIME+DT	DAV20052
44	CALL EHPA(P,A)	DAV20053
45	THETA=THETA+DTHETA	DAV20054
46	IF(I/IBSTEP*IBSTEP .EQ. I)CALL BFLDS2(EARTH+WE*TIME,THETA,BT)	DAV20055
47	IF(ENERGY .LT. 0.01) CALL BFLDS3(THETA,BT)	DAV20056
48	CALL MULVEC(A,BT,BB)	DAV20057
49	CALL TORQUE(T,BB,CONST)	DAV20058
		DAV20059
50	CALL RK4	DAV20060
51	IF(TIME .GT. TRUN) STOP	DAV20061
52	GO TO 50	DAV20062
53	90 FORMAT(SF10.3)	DAV20063
54	100 FORMAT(1H ,F6.0, 2X,3(E10.3,1X),3(F6.3,1X), 2E15.5,2F7.3)	DAV20064
55	101 FORMAT(1H1,' TIME OMEGA1 OMEGA2 OMEGA3 B1	BD V20065
	62 B3 ERROR ENERGY +ROLL NEG. YAW')	DAV20066
56	1100FORMAT(///// ,50X,'SYSTEM PARAMETERS ARE',//,60X,'INERTIA(1)=',	DAV20067
	1 F10.2,///,60X,'INERTIA(2)=',F10.2,///,60X,'INERTIA(3)=',F10.2,	DAV20068
	2 ///,60X,'MOMENTUM BIAS=',F10.3,///,60X,'MAGNET STRENGTH FACTOR=',	DAV20069
	3 F10.2)	DAV20070
57	1110FORMAT(///// ,50X,'INTERVALS ARE',//,60X,'PRINT EVERY',F10.0,	DAV20071
	1 ' TIME STEPS',//,25X,'CALCULATE MAGNETIC FIELD EVERY',F10.2,	DAV20072
	2 ' DEGREES OF ORBIT')	DAV20073
58	1120FORMAT(///// ,10X,'INTEGRATION STEP SIZE=',F5.2,' SECONDS.-- RUNG	DAV20074
	1E-KUTTA FOURTH ORDER INTEGRATION WITH EULER HOMOGENEOUS PARAMETERS	DAV20075
	2',///// ,50X,'ORBIT SPECIFICATIONS',//,25X,'INCLINATION ANG.=',F10.2	DAV20076
	3 ' DEGREES',//,25X,'ROTATION OF EARTH MINUS LONGITUDE OF THE	DAV20077
	4 NODES(INITIAL)=' ,F10.2,' DEGREES',//,50X,'ORBIT ALTITUDE (CEN	DAV20078
	STRAL DISTANCE)=' ,F10.0,' KM.',//,25X,'PERIOD FOR THIS ORBIT=',	DAV20079
	6 F10.0,' SECS.',//,25X,'ALL UNITS ARE IN M-K-S SYSTEM UNLESS	DAV20080
	7 OTHERWISE NOTED')	DAV20081
59	END	DAV20082

60	SUBROUTINE EHPA(P,A)	DAV20083
61	REAL*4 P(4), A(3,3)	DAV20084
C	****THIS ROUTINE RETURNS THE ROTATION MATRIX A CORRESPONDING	DAV20085
C	****TO THE EULER HOMOGENEOUS PARAMETERS P SUB I. A*V(OLD)=V(NEW)	DAV20086
62	P12=P(1)*P(1)	DAV20087
63	P22=P(2)*P(2)	DAV20088
64	P32=P(3)*P(3)	DAV20089
65	P42=P(4)*P(4)	DAV20090
66	A(1,1)=P42+P12-P22-P32	DAV20091
67	A(1,2)=2.*(P(1)*P(2)+P(3)*P(4))	DAV20092
68	A(1,3)=2.*(P(1)*P(3)-P(2)*P(4))	DAV20093
69	A(2,1)=2.*(P(1)*P(2)-P(3)*P(4))	DAV20094
70	A(2,2)=P42+P22-P32-P12	DAV20095
71	A(2,3)=2.*(P(2)*P(3)+P(1)*P(4))	DAV20096
72	A(3,1)=2.*(P(1)*P(3)+P(2)*P(4))	DAV20097
73	A(3,2)=2.*(P(2)*P(3)-P(1)*P(4))	DAV20098
74	A(3,3)=P42+P32-P22-P12	DAV20099
75	RETURN	DAV20100
76	END	DAV20101

77	SUBROUTINE EHPQT(P,QT)	DAV20102
78	REAL*4 P(4), QT(4,4)	DAV20103
C	****THIS SUBROUTINE SETS UP THE MATRIX Q TRANSPOSE FOR ANY GIVEN SET	DAV20104
C	****OF EULER'S HOMOGENEOUS PARAMETERS--- THE P SUB I	DAV20105
79	QT(1,1)=P(4)	DAV20106
80	QT(1,2)=-P(3)	DAV20107
81	QT(1,3)=P(2)	DAV20108
82	QT(2,1)=P(3)	DAV20109
83	QT(2,2)=P(4)	DAV20110
84	QT(2,3)=-P(1)	DAV20111
85	QT(3,1)=-P(2)	DAV20112
86	QT(3,2)=P(1)	DAV20113
87	QT(3,3)=P(4)	DAV20114
88	QT(4,1)=-P(1)	DAV20115
89	QT(4,2)=-P(2)	DAV20116
90	QT(4,3)=-P(3)	DAV20117
91	RETURN	DAV20118
92	END	DAV20119



109	SUBROUTINE NORM(P,MAG)	DAV20140
110	REAL*4 P(4),MAG	DAV20141
	C *****THIS ROUTINE NORMALIZES P TO LENGTH = UNITY AND RETURNS ITS	DAV20142
	C *****LENGTH PRIOR TO NORMALIZATION AS A CONVENIENT ERROR MEASURE.	DAV20143
111	MAG=0.	DAV20144
112	DO 1 I=1,4	DAV20145
113	1 MAG=MAG+P(I)*P(I)	DAV20146
114	MAG=SQRT(MAG)	DAV20147
115	DO 2 I=1,4	DAV20148
116	2 P(I)=P(I)/MAG	DAV20149
117	RETURN	DAV20150
118	END	DAV20151

93	SUBROUTINE WDOT(W,WD)	DAV20120
	C EQUATIONS OF MOTION OF OUR BODY	DAV20121
	C WD'S ARE OMEGA DERIVATIVES; T'S ARE TORQUES, C'S AND COMM'S ARE CONST	DAV20122
	C AND MOMENTUM BIASES	DAV20123
94	REAL*4 W(3), WD(3)	DAV20124
95	COMMON/WDOTS/ T(3), COMM(10), C1, C2, C3, C4, C5, C6	DAV20125
96	WD(1)=T(1)*C4+C1*W(2)*W(3) -COMM(1)*W(2)	DAV20126
97	WD(2)=T(2)*C5+C2*W(1)*W(3) +COMM(2)*W(1)	DAV20127
98	WD(3)=T(3)*C6+C3*W(1)*W(2)	DAV20128
99	RETURN	DAV20129
100	END	DAV20130

101	SUBROUTINE MAT1(A,V1,V2)	DAV20131
	C UTILITY MULTIPLICATION-- USED IN RELATING OMEGA'S TO P DOTS	DAV20132
102	REAL*4 A(4,4), V1(3), V2(4)	DAV20133
103	DO 1 I=1,4	DAV20134
104	V2(I)=0.	DAV20135
105	DO 1 J=1,3	DAV20136
106	1 V2(I)=V2(I)+A(I,J)*V1(J)	DAV20137
107	RETURN	DAV20138
108	END	DAV20139

FORM NO 14113 PRINTED IN U.S.A.

119	SUBROUTINE RK4	DAV20152
120	COMMON/RK/ P(4),W(3),QT(4,4),DT,W0	DAV20153
121	REAL*4 PDO(4),D(4)	DAV20154
122	REAL*4 D1(3),D2(3),D3(3),D4(3),S(3),PD1(4),PD2(4),PD3(4),PD4(4)	DAV20155
C	****THIS SUBROUTINE INTEGRATES W (BODY REFERENCED ANGULAR VELOCITY)	DAV20156
C	****AND P (THE EULER HOMOGENEOUS PARAMETERS) FROM TIME T TO T+DT.	DAV20157
C	****TECHNIQUE IS A FOURTH ORDER RUNGE KUTTA SCHEME.	DAV20158
C	*****	DAV20159
C	****REQUIRES SUBROUTINES WDOT (USER SUPPLIED), MAT1, AND ARRAY QT.	DAV20160
123	CALL EHPQT(P,QT)	DAV20161
124	CALL MAT1(QT,W,PD1)	DAV20162
125	CALL WDOT(W,D1)	DAV20163
126	DO 10 I=1,3	DAV20164
127	10 S(I)=W(I)+0.5*DT*D1(I)	DAV20165
128	DO 11 I=1,4	DAV20166
129	11 D(I)=P(I)+0.5*DT*PD1(I)	DAV20167
130	CALL EHPQT(D,QT)	DAV20168
131	CALL MAT1(QT,S,PD2)	DAV20169
132	CALL WDOT(S,D2)	DAV20170
133	DO 20 I=1,3	DAV20171
134	20 S(I)=W(I)+0.5*DT*D2(I)	DAV20172
135	DO 21 I=1,4	DAV20173
136	21 D(I)=P(I)+0.5*DT*PD2(I)	DAV20174
137	CALL EHPQT(D,QT)	DAV20175
138	CALL MAT1(QT,S,PD3)	DAV20176
139	CALL WDOT(S,D3)	DAV20177
140	DO 30 I=1,3	DAV20178
141	30 S(I)=W(I)+ DT*D3(I)	DAV20179
142	DO 31 I=1,4	DAV20180
143	31 D(I)=P(I)+ DT*PD3(I)	DAV20181
144	CALL EHPQT(D,QT)	DAV20182
145	CALL MAT1(QT,S,PD4)	DAV20183
146	CALL WDOT(S,D4)	DAV20184
147	DO 40 I=1,3	DAV20185
148	40 W(I)=W(I)+DT*(D1(I)+2. *(D2(I)+D3(I))+D4(I))/6.	DAV20186
149	PDO(1)=+W0*P(2)	DAV20187
150	PDO(2)=-W0*P(1)	DAV20188
151	PDO(3)=-W0*P(4)	DAV20189
152	PDO(4)=+W0*P(3)	DAV20190
***ERROR***	MO-0	
153	DO 50 I=1,4	DAV20191
154	50 P(I)=P(I)+DT*(PD1(I)+PD4(I)+2. *PD2(I)+2. *PD3(I)+6. *PDO(I))/12.0	DAV20192
155	RETURN	DAV20193
156	END	DAV20194

190	SUBROUTINE TORQUE(T,B,CONST)	DAV20233
	C IDEAL MAGNET SWITCHER	DAV20234
	C SETS MAGNET POLARITIES OPPOSITE IN SIGN TO B DOTS	DAV20235
	C SIGN OF B DOTS IS DETERMINED BY COMPARING PRESENT (B'S) VS. PREVIOUS	DAV20236
	C (BOLD'S) BODY COMPONENTS OF MAGNETIC FIELD	DAV20237
	C THEN, TORQUE= M CROSS B	DAV20238
191	REAL*4 T(3), B(3), M1, M2, M3, B1OLD/0.0/, B2OLD/0.0/, B3OLD/0.0/	DAV20239
192	B1=B(1)	DAV20240
193	B2=B(2)	DAV20241
194	B3=B(3)	DAV20242
195	BD1NEG=B1OLD-B1	DAV20243
196	BD2NEG=B2OLD-B2	DAV20244
197	BD3NEG=B3OLD-B3	DAV20245
198	M1=SIGN(CONST, BD1NEG)	DAV20246
199	M2=SIGN(CONST, BD2NEG)	DAV20247
200	M3=SIGN(CONST, BD3NEG)	DAV20248
201	T(1)=M2*B3-M3*B2	DAV20249
202	T(2)=M3*B1-M1*B3	DAV20250
203	T(3)=M1*B2-M2*B1	DAV20251
204	B1OLD=B1	DAV20252
205	B2OLD=B2	DAV20253
206	B3OLD=B3	DAV20254
207	RETURN	DAV20255
208	END	DAV20256

157	SUBROUTINE MULVEC(A,V1,V2)	DAV20195
158	REAL*4 A(3,3), V1(3), V2(3)	DAV20196
	C MULTIPLIES A*V1=V2	DAV20197
159	DO 1 I=1,3	DAV20198
160	V2(I)=0.0	DAV20199
161	DO 1 K=1,3	DAV20200
162	1 V2(I)=V2(I)+A(I,K)*V1(K)	DAV20201
163	RETURN	DAV20202
164	END	DAV20203

165	SUBROUTINE BFLDS1(INCLIN,A,B)	DAV20204
C	RETURNS MAGNETIC FIELD FOR VARIOUS POSITIONS IN ORBIT-- SEE SEPARATE	DAV20205
C	DOCUMENTATION	DAV20206
166	REAL B(3), INCLIN, PI/3.1416/	DAV20207
167	RADDEG=PI/180.	DAV20208
168	BNOM=1.011E+12/(4.0*PI*A*A*A)	DAV20209
169	SN=0.2026	DAV20210
170	CN=0.980	DAV20211
171	SI=SIN(INCLIN*RADDEG)	DAV20212
172	CI=COS(INCLIN*RADDEG)	DAV20213
173	RETURN	DAV20214
174	ENTRY BFLDS2(EARTH,THETA,B)	DAV20215
C	THETA IS THE ANGLE IN ORBIT FORWARD FROM ASCENDING NODE (DEGREES)	DAV20216
C	EARTH= W(EARTH)*T- LONGITUDE OF THE ASCENDING NODE --(ALSO DEGREES)	DAV20217
175	U=(69.0-EARTH)*RADDEG	DAV20218
176	CU=COS(U)	DAV20219
177	SU=SIN(U)	DAV20220
178	B(3)=BNOM*(CI*CN+SI*SU*SN)	DAV20221
179	C1=-CU*SN	DAV20222
180	C2=CI*SU*SN-SI*CN	DAV20223
181	10 V=THETA*RADDEG	DAV20224
182	CV=COS(V)	DAV20225
183	SV=SIN(V)	DAV20226
184	B(1)=2.0*BNOM*(C1*CV+C2*SV)	DAV20227
185	B(2)=BNOM*(C1*SV-C2*CV)	DAV20228
186	RETURN	DAV20229
187	ENTRY BFLDS3(THETA,B)	DAV20230
188	GO TO 10	DAV20231
189	END	DAV20232

## APPENDIX C

### DUAL SPIN EQUILIBRIUM CONSIDERATIONS

In this appendix we consider the equilibrium and stability of a dual spin configuration. Although this work has been done before (e.g. reference 6), we derive the results here in a simpler way. These results were obtained independently by the author before his acquaintance with reference 6 and are included here for completeness.

Consider a body with a single momentum bias wheel; the wheel spins at constant rate and carries angular momentum  $\bar{h} = \{0, 0, h\}$ . The body is spinning about the same axis as is the rotor; for definiteness this is taken as the "3" axis. Suppose we consider the torque free motion of the body in the "neighborhood" of an equilibrium point, namely

$$\omega_1 = \omega_2 = 0, \quad \omega_3 = \Omega \quad (C1)$$

In the neighborhood of this point

$$\omega_1 = \delta\omega_1, \quad \dot{\omega}_1 = \delta\dot{\omega}_1 \quad (C2,a)$$

$$\omega_2 = \delta\omega_2, \quad \dot{\omega}_2 = \delta\dot{\omega}_2 \quad (C2,b)$$

$$\omega_3 = \Omega + \delta\omega_3, \quad \dot{\omega}_3 = \delta\dot{\omega}_3 \quad (C2,c)$$

Now, the equations of motion, adapted from eq. (1) are

$$I_1\dot{\omega}_1 + \omega_2\{h + \omega_3(I_3 - I_2)\} = 0 \quad (C3,a)$$

$$I_2\dot{\omega}_2 - \omega_1\{h + \omega_3(I_3 - I_1)\} = 0 \quad (C3,b)$$

$$I_3\dot{\omega}_3 + \omega_1\omega_2(I_2 - I_1) = 0 \quad (C3,c)$$

Substituting eq. (C2) into these, and dropping second order terms (involving products of the  $\delta\omega$ 's), we obtain

$$I_1\delta\dot{\omega}_1 + \delta\omega_2\{h + (\Omega + \delta\omega_3)(I_3 - I_2)\} = 0 \quad (C4,a)$$

$$I_2\delta\dot{\omega}_2 - \delta\omega_1\{h + (\Omega + \delta\omega_3)(I_3 - I_1)\} = 0 \quad (C4,b)$$

$$I_3\delta\dot{\omega}_3 = 0 \quad (C4,c)$$

Thus we see immediately  $\delta\omega_3 = 0$ , therefore  $\omega_3 = \Omega = \text{constant}$ . Then, equations a and b can be combined to yield

$$\delta\ddot{\omega}_1 + \frac{\delta\omega_1}{I_1 I_2} \{h + \Omega(I_3 - I_2)\} \{h + \Omega(I_3 - I_2)\} = 0 \quad (C5)$$

What we have obviously obtained here is the equation for a simple harmonic oscillator. Consider one special case first. If  $\Omega$  is "small", then  $\omega_1$  (and  $\omega_2$ , which has the same form of solution) oscillates with circular frequency

$$\lambda_0 = \frac{h}{\sqrt{I_1 I_2}} \quad (C6)$$

If  $\Omega$  is not small, let us define an equivalent inertia

$$I_{3e} = I_3 + h/\Omega \quad (C7)$$

Then eq. (C5) reads

$$\delta \ddot{\omega}_1 + \frac{\delta \omega_1 \Omega^2 (I_{3e} - I_2) (I_{3e} - I_1)}{I_1 I_2} = 0 \quad (C8)$$

It is clear that if either

$$I_{3e} > I_1 \text{ and } I_{3e} > I_2 \quad (C9, a)$$

or

$$I_{3e} < I_1 \text{ and } I_{3e} < I_2 \quad (C9, b)$$

that is, if  $I_{3e}$  is a minimum or maximum inertia, then, our system is stable in the Liapunov sense. On the other hand, if  $I_{3e}$  is an intermediate inertia, the system is unstable. These results are of a physically appealing nature since they are of the same form as the results for spinning rigid bodies. In fact, if in eq. (C7)  $h = 0$ ,  $I_{3e} = I_3$ , and those results are obtained directly.

For non-rigid (i.e., damped) bodies, these requirements are modified somewhat. First, there is generally little damping on the rotor, and that which is present has a destabilizing effect (almost always). Consider then a system with negligible damping on the rotor and a non-negligible amount on the main body. If the spin directions are such that the momenta of rotor and main body add ( $\Omega > 0$ ), it can be shown that it is necessary and sufficient for stability that  $I_{3e}$  be the major principal axis (maximum). Conversely, if the momenta oppose each other ( $\Omega < 0$ ), it is necessary and sufficient that

$$h_0 = h + I_3 \Omega > 0 \quad (C10)$$

$$-\frac{h}{I_3} < \Omega < 0 \quad (C11)$$

There is one additional region of stability for this system, and it exists only if  $I_3$  is a major axis. The region defined by

$$\Omega < \frac{-h}{I_3 - \max(I_1, I_2)} \quad (C12)$$

corresponds to  $I_{3e}$  being a major principal axis while  $\Omega < 0$ . As  $h \rightarrow 0$  the above results reduce to the simple major spin axis requirements.

Definition (C7) may be combined with this observation into a simple rule, to wit

$$h_0 > I\Omega \quad (C10)$$

where  $h_0$  is the system momentum bias (equal to  $h + I_3\Omega$ ), and  $I = \max(I_1, I_2)$ . This same conclusion is obtained in reference 6 (page A-82).

The result (C10) has a direct application to the attitude acquisition phenomena noted under the section "Terminal Orientation". Namely, since the magnets will drive the satellite at  $2\omega_0$  in the terminal orientation, and since we wish the terminal attitude to correspond to a stable condition, it is necessary that (C10) hold for  $\Omega = 2\omega_0$ . For a given orbit (which determines  $\omega_0$ ) and given set of inertias, this requirement then specifies a minimum  $h$ . The validity of this conclusion is supported by a number of simulation runs. In fact, it was observed that for good terminal attitude acquisition performance the left side of (C10) should be at least three or four times the right side.



## APPENDIX D

### SYSTEM EQUILIBRIUM POINTS

Consider the equilibrium states of the acquisition system described in this report under two conditions. (a) The magnetic field is fixed in trajectory axis coordinates, that is

$$\frac{d^{SPACE}(\bar{B})}{dt} = 0 \quad (D1)$$

and (b), the magnet controllers employ a linear law

$$\dot{\bar{M}} = -K\dot{\bar{B}} \quad (D2)$$

where  $\dot{\bar{B}}$  is the time rate of change of  $\bar{B}$  as measured in the vehicle. As mentioned in the body of this report, under the section titled "Stability", this system has no equilibrium points unless some modification is made to the flip-flop magnet control law. Now, let us consider the equilibrium points possible under the two conditions above.

The behavior of our system may be completely characterized by the six state variables  $\omega_1, \omega_2, \omega_3, B_1, B_2, B_3$ . Equilibrium points may be identified by setting the time derivatives of these variables to zero and solving the resulting six equations in six unknowns. That is, we require

$$\dot{\bar{\omega}} = 0 \quad (D3)$$

$$\dot{\bar{B}} = \bar{B} \times \bar{\omega} = 0 \quad \text{eq. (8) = (D4)}$$

Starting with equation (1), we make the following substitutions:  $\bar{\tau} = 0$  (torque free motion),  $\dot{\bar{h}} = 0$  (constant speed wheel), and eq. (1')  $\bar{H} = \bar{I} \cdot \bar{\omega} + \bar{h}$ . We then obtain

$$\bar{I} \cdot \dot{\bar{\omega}} = -\bar{\omega} \times (\bar{I} \cdot \bar{\omega} + \bar{h}) = 0 \quad (D5)$$

The right hand side of (D5) equals zero according to (D3). An equilibrium point must then, by definition, satisfy equations (D4) and (D5). (D4) simply requires that

$$\bar{\omega} = \alpha(t)\bar{B} \quad (D6)$$

where  $\alpha(t)$  may or may not be zero and may or may not be constant. Now, if

$$\bar{h} = \{0, 0, h\} = h \quad (D7)$$

That is, we have a pitch wheel only, then (D5) becomes, in scalar form

$$\omega_2\omega_3(I_3 - I_2) + h\omega_2 = 0 \quad (D8,a)$$

(D5, modified)

$$\omega_1\omega_3(I_1 - I_3) - h\omega_1 = 0 \quad (D8,b)$$

$$\omega_1\omega_2(I_2 - I_1) = 0 \quad (D8,c)$$

From the above discussion we now obtain the following results

- (I)  $\bar{\omega} = \{0, 0, 0\}$ ,  $\bar{B} = \text{any}$ ,  $\alpha = 0$  is an equilibrium point, since it clearly satisfies eq. (D4) & (D8).
- (II)  $\bar{\omega} = \{0, \text{any}, h/(I_2 - I_3)\}$ ,  $\bar{B} \parallel \bar{\omega}$  is an equilibrium point.
- (III)  $\bar{\omega} = \{\text{any}, 0, h/(I_1 - I_3)\}$ ,  $\bar{B} \parallel \bar{\omega}$  is an equilibrium point.
- (IV)  $\bar{\omega} = \{0, 0, \text{any}\}$ ,  $\bar{B} \parallel \bar{\omega}$  is the last equilibrium point.

These four classes contain all the equilibrium points of this system. In passing I note (for the mathematicians among us) that there are an infinity of equilibrium points. Note also that at equilibrium points,  $\dot{\bar{B}} = 0$  so  $\bar{M} = 0$  and so the fact that we set  $\tau = 0$  at the outset does not affect the validity of the results obtained here.

There is, curiously, an alternate method of obtaining these same results. Starting with the equation of motion (1), the control law (D2), and the assumptions (D1) and (D7), we have

$$\tau_1 = I_1 \dot{\omega}_1 + \omega_2 h \quad (D9, a)$$

$$\tau_2 = I_2 \dot{\omega}_2 - \omega_1 h$$

$$\tau_3 = I_3 \dot{\omega}_3$$

where we have dropped the second order terms involving products of the  $\omega$ 's. Using eq. (D2) and (D4), we obtain

$$M_1 = K(\omega_2 B_3 - \omega_3 B_2) \quad (D10, a)$$

$$M_2 = K(\omega_3 B_1 - \omega_1 B_3) \quad (D10, b)$$

$$M_3 = K(\omega_1 B_2 - \omega_2 B_1)$$

Remembering eq. (5)

$$\bar{\tau} = \bar{M} \times \bar{B} \quad (5)$$

and substituting  $\bar{\tau}$  into eq. (D9), we obtain

$$I_1 \dot{\omega}_1 + \omega_2 h = B_3 K(\omega_3 B_1 - \omega_1 B_3) - B_2 K(\omega_1 B_2 - \omega_2 B_1) \quad (D11, a)$$

$$I_2 \dot{\omega}_2 - \omega_1 h = B_1 K(\omega_1 B_2 - \omega_2 B_1) - B_3 K(\omega_2 B_3 - \omega_3 B_2) \quad (D11, b)$$

$$I_3 \dot{\omega}_3 = B_2 K(\omega_2 B_3 - \omega_3 B_2) - B_1 K(\omega_3 B_1 - \omega_1 B_3) \quad (D11, c)$$

Using the definition of equilibrium points

$$\dot{\bar{\omega}} = 0$$

(here we are considering only  $\bar{\omega}$  as a state variable,  
not  $\bar{B}$ )

we obtain three linear homogeneous equations in the three unknowns -  $\omega_1$ ,  $\omega_2$ , and  $\omega_3$ . For a solution to exist, the determinant of the coefficients must equal zero. That is

$$\begin{vmatrix} -(B_2^2 + B_3^2) & (B_1B_2 - h/K) & B_1B_3 \\ (B_1B_2 + h/K) & -(B_1^2 + B_3^2) & B_2B_3 \\ B_1B_3 & B_2B_3 & -(B_1^2 + B_2^2) \end{vmatrix} = 0 \quad (D12)$$

This equation reduces to

$$-\frac{h^2}{K^2}(B_1^2 + B_2^2) = 0 \quad (D12')$$

or

$$\bar{B} = \{0, 0, B_3\} \quad (D13)$$

Substituting this back into eq. (D11) we have

$$I_1\dot{\omega}_1 + \omega_2h = -B_3^2K\omega_1 \quad (D14,a)$$

$$I_2\dot{\omega}_2 - \omega_1h = -B_3^2K\omega_2 \quad (D14,b)$$

$$I_3\dot{\omega}_3 = 0 \quad (D14,c)$$

Since  $\dot{\bar{\omega}} = 0$ , we obtain the following equilibrium condition

$$\omega = \{0, 0, \text{any}\} \quad (D15)$$

This result is not valid if  $\omega_3$  is large, since we neglected  $\omega_3(I_3 - I_2)$  and  $\omega_3(I_3 - I_1)$  in comparison to  $h$  in writing eq. (D9). To the extent that this is valid, (D15) is correct. Note that (D15) is the same as condition (IV) identified previously, and that (I) is a special case of (IV).

The only special thing about this alternate derivation is that we did not assume  $\dot{\bar{B}} = 0$  at the outset. We were considering cases where  $\bar{\omega} = 0$  but  $\dot{\bar{B}}$  and hence  $\bar{\tau}$  not necessarily equal to zero. Note that, in retrospect, we now have  $\bar{B} = \{0, 0, B_3\}$ , so  $\dot{B}_1 = \dot{B}_2 = M_1 = M_2 = 0$ . The result is then that  $\bar{\tau} = 0$  anyway.

In the next section we consider the stability of the equilibrium points enumerated here.

## APPENDIX E

### STABILITY OF EQUILIBRIUM POINTS

In this appendix we investigate the stability of a particular equilibrium point, namely point IV of Appendix D. This stability investigation is carried out by linearizing the system equations about the equilibrium point and then forming the characteristic equation. A study of the roots of this equation then determines the stability of the system near the equilibrium point. This does not rule out the possibility of limit cycle like behavior but is nonetheless a useful technique. From the analysis that follows, certain conclusions may be drawn. These conclusions and their consequences are discussed at the end of this appendix.

Consider perturbations about the equilibrium point

$$\bar{\omega} = \{0, 0, \Omega\} \quad (E1)$$

$$\bar{B} = \{0, 0, B\}$$

Then

$$\bar{\omega} = \{\delta\omega_1, \delta\omega_2, \Omega + \delta\omega_3\} \quad (E2)$$

$$\bar{B} = \{\delta B_1, \delta B_2, B + \delta B_3\}$$

The following equations then apply

$$\dot{\bar{B}} = \bar{B} \times \bar{\omega} \quad (8)$$

$$\delta\dot{B}_1 = \Omega\delta B_2 - B\delta\omega_2$$

$$\delta\dot{B}_2 = B\delta\omega_1 - \Omega\delta B_1 \quad (E3)$$

$$\delta\dot{B}_3 = 0$$

where we have dropped second order terms in eq. (E3). Now, assuming a linear control law, i.e.,

$$\bar{M} = -K\dot{\bar{B}} \quad (E4)$$

$$M_1 = K(B\delta\omega_2 - \Omega\delta B_2) \quad (E5)$$

$$M_2 = K(\Omega\delta B_1 - B\delta\omega_1)$$

$$M_3 = 0$$

Then, since

$$\bar{\tau} = \bar{M} \times \bar{B} \quad (5)$$

We obtain

$$\tau_1 = KB(\Omega\delta B_1 - B\delta\omega_1) \quad (E6)$$

$$\tau_2 = KB(\Omega\delta B_2 - B\delta\omega_2)$$

$$\tau_3 = 0$$

Similarly, we may start with eq. (1), substitute from (E2) and drop second order terms in the result. Thus we obtain the linearized equations of motion about the equilibrium point

$$I_1 \dot{\delta\omega}_1 = \tau_1 - \delta\omega_2 (h + \Omega(I_3 - I_2)) \quad (E7)$$

$$I_2 \dot{\delta\omega}_2 = \tau_2 + \delta\omega_1 (h + \Omega(I_3 - I_1))$$

$$I_3 \dot{\delta\omega}_3 = \tau_3$$

These may be written in a way that makes them easier to interpret by using the following shorthand notation:

$$I_{3e} = \frac{h}{\Omega} + I_3 \quad (E8)$$

$$I_{3e}\Omega = h + I_3\Omega = h_0 \quad (E9)$$

$$h + \Omega(I_3 - I_2) = \Omega(I_{3e} - I_2) = \alpha_1 \quad (E10)$$

$$h + \Omega(I_3 - I_1) = \Omega(I_{3e} - I_1) = \alpha_2 \quad (E11)$$

Using this notation and substituting for the  $\tau_i$  from (E6) we obtain

$$\dot{\delta\omega}_1 = -\frac{KB^2}{I_1}\delta\omega_1 - \frac{\alpha_1}{I_1}\delta\omega_2 + \frac{KB\Omega}{I_1}\delta B_1 + 0\delta B_2$$

$$\dot{\delta\omega}_2 = \frac{\alpha_2}{I_2}\delta\omega_1 - \frac{KB^2}{I_2}\delta\omega_2 + 0\delta B_1 + \frac{KB\Omega}{I_2}\delta B_2 \quad (E12)$$

$$\dot{\delta B}_1 = +0\delta\omega_1 - B\delta\omega_2 + 0\delta B_1 + \Omega\delta B_2$$

$$\dot{\delta B}_2 = B\delta\omega_1 + 0\delta\omega_2 - \Omega\delta B_1 + 0\delta B_2$$

The last two equations are from (E3). Note that the last equations in (E3) and (E7) immediately yield

$$\dot{\delta B}_3 = 0, \delta B_3 = \text{const} = 0, B_3 = B \quad (E13)$$

$$\dot{\delta\omega}_3 = 0, \delta\omega_3 = \text{const} = 0, \omega_3 = \Omega$$

Equations (E12) constitute four first order ordinary linear differential equations in four unknowns. They are of the form

$$\dot{\bar{X}} = A \bar{X} \quad (E12,a)$$

where A is a square matrix with constant coefficients.

Now, if A is negative (positive) definite it may be immediately shown that the system described by (E12,a) is asymptotically stable (unstable) by applying Liapunov's (Chetayev's) stability theorem to the function  $v = \bar{x} \cdot \bar{x}$ . Unfortunately, for our problem, as for many others, A is sign indefinite and the theorems noted are not so easily applied.

Instead, we Laplace transform (E12,a)

$$s\bar{X}(s) - \bar{x}_0 = A\bar{X}(s) \quad (E14)$$

Thus

$$\bar{X}(s) = (A - Is)^{-1}(-\bar{x}_0) \quad (E15)$$

and

$$\bar{x}(t) = L^{-1}\{(A - Is)^{-1}(-\bar{x}_0)\} \quad (E16)$$

Note that, as shown by E15, all the components of  $\bar{X}(s)$  (remember,  $\bar{x}(t)$  and  $\bar{X}(s)$  are column vectors) have a denominator  $D(s)$  and

$$D(s) = \text{Determinant}(A - Is) \quad (E17)$$

Now,  $D(s)$  may also be written as

$$D(s) = (s - s_1)(s - s_2) \cdots (s - s_n) \quad (E18)$$

where the  $s_i$  are the roots of  $D(s) = 0$  or  $\text{Det}(A - Is) = 0$ . Alternately, the  $s_i$  are the eigenvalues of the matrix A. Obviously, for stability, it is necessary and sufficient that the real parts of the  $s_i$  be less than zero.

To determine the  $s_i$  we expand

$$D(s) = \text{Det}(A - Is) = 0 \quad (E19)$$

obtaining the (linearized system) characteristic equation in terms of the various system parameters. The matrix A from (E12) is

$$A = \begin{bmatrix} -KB^2/I_1 & -\alpha_1/I_1 & KB\Omega/I_1 & 0 \\ \alpha_2/I_2 & -KB^2/I_2 & 0 & KB\Omega/I_2 \\ 0 & \alpha B & 0 & \Omega \\ B & 0 & -\Omega & 0 \end{bmatrix} \quad (E20)$$

and the expansion (E19) yields, after a little algebra

$$I_1 I_2 s^4 + (I_1 + I_2) KB^2 s^3 + (I_1 I_2 \Omega^2 + \alpha_1 \alpha_2 + K^2 B^4) s^2 + KB^2 \Omega (\alpha_1 + \alpha_2) s + \alpha_1 \alpha_2 \Omega^2 = 0 \quad (E21)$$



We require, for stability, that all the solutions of (E21) lie in the left half-plane. We may attack (E21) either numerically or analytically. Consider the analytical approach first.

If we apply Routh's Criterion to (E21) we obtain, as the necessary and sufficient conditions for stability, that the following quantities must be greater than zero if  $a_1$  is

$$I_1 I_2 > 0 \quad (a1)$$

$$(I_1 + I_2) K B^2 > 0 \quad (a2)$$

$$\phi_1 = I_1 I_2 \Omega^2 + \alpha_1 \alpha_2 + K^2 B^4 - \frac{I_1 I_2 \Omega (\alpha_1 + \alpha_2)}{I_1 + I_2} > 0 \quad (a3)$$

$$\phi_2 = K B^2 \Omega (\alpha_1 + \alpha_2) - K B^2 \Omega^2 \alpha_1 \alpha_2 (I_1 + I_2) / \phi_1 > 0 \quad (a4)$$

$$\alpha_1 \alpha_2 \Omega^2 > 0 \quad (a5)$$

Requirement (a1) is trivial, and so is (a2) as long as  $K > 0$ . (a5) is satisfied as long as the body is dynamically stable (see appendix C) without the control system. We must address ourselves to (a3) and (a4). We first note, en passant, that if we set  $K = 0$  in (E21) we obtain the characteristic equation for the system without control torques. This situation was examined in appendix C. Equation (E21) becomes

$$s^4 + a s^2 + b = 0 \quad (E22)$$

where

$$b = \frac{\alpha_1 \alpha_2 \Omega^2}{I_1 I_2}$$

and

$$a = \Omega^2 + \frac{\alpha_1 \alpha_2}{I_1 I_2} + K^2 B^4$$

It is trivial to show that the requirements for stability of (E22) are that  $a > 0$ ,  $b > 0$ . Obviously  $b > 0$  is the stronger condition; we obtain the requirement

$$\alpha_1 \alpha_2 > 0 \quad (E23)$$

and this is always satisfied if the system is stable without the control system.

We return now to conditions (a3) and (a4).  $\phi_1$  can always be made greater than zero for sufficiently large gain K. For  $K = 0$ , (a3) may be written as

$$2(I_1 + I_2) + \frac{(I_1 + I_2)(I_{3e} - I_2)(I_{3e} - I_1)}{I_1 I_2} > 2I_{3e} \quad (E24)$$

Various cases of this can now be considered. If  $\Omega$  is small and less than zero (opposite in sense to  $\bar{h}$ ), (E24) is easily satisfied. If  $\Omega$  is small and positive this relation is always satisfied. For large values of  $\Omega$  (either sign)  $I_{3e} \rightarrow I_3$ . If  $I_3$  is a major or minor axis (E24) is always satisfied. If  $I_3$  is an intermediate axis, (E24) may fail (for  $K = 0$ ) for sufficiently large  $\Omega$  (which is required to make  $I_{3e} \rightarrow I_3$ ). Before this happens the criterion (a5) will fail, so we need not concern ourselves with (a3) except perhaps for some intermediate values of  $\Omega$ , such that neither  $I_{3e} > I_1, I_2$  nor  $I_{3e} \rightarrow I_3$ . If we make some simplifying assumptions- namely  $I_1 = I_2 = I$ , and  $I_{3e} = nI$ , (E24) reduces to

$$(n - 1)^2 > (n - 2) \quad (E25)$$

which holds for all values of  $n$ , positive and negative. It would seem that except for a rather oddly configured satellite that  $\phi_1 > 0$ , and (a3) presents no problems. In fact, unless the ratio between  $I_1$  and  $I_2$  is greater than 5:1, a3 must be satisfied. Additionally, for  $K > 0$ ,  $\phi_1$  increases and (a3) presents even fewer problems. On the basis of this analysis we turn our attention to condition (a4).

$$\phi_2 = KB^2\Omega(\alpha_1 + \alpha_2) - KB^2\Omega^2\alpha_1\alpha_2(I_1 + I_2)/\phi_1 > 0 \quad (a4)$$

$$\phi_2 = KB^2\Omega^2[(2I_{3e} - I_1 - I_2) - \Omega^2(I_1 + I_2)(I_{3e} - I_1)(I_{3e} - I_2)/\phi_1] > 0 \quad (E26)$$

Now, from condition (a5) we see that the second term of (E26) is less than zero. Thus, if the first term is less than zero, this system is unstable. It is a requirement then, for stability, that  $I_{3e}$  be the major principal axis of the satellite (ie,  $I_{3e} > \max(I_1, I_2)$ ).

Now, for our system,  $I_3$  is a minor axis, and for large values of  $\Omega$ ,  $I_{3e} \rightarrow I_3$ , so the system is unstable. For  $\Omega > 0$ , in fact,  $I_{3e}$  is always a minor axis (if  $I_3$  is). The only stable values for operation are positive values not "large". In examining this problem we now turn to a numerical study.

For a numerical evaluation, the following values are substituted in conditions (a3), (a4) and (a5).

$$I_1 = 35 \text{ slug-ft}^2 \quad (47.5 \text{ Kg-m}^2)$$

$$I_2 = 50 \text{ slug-ft}^2 \quad (67.9 \text{ Kg-m}^2)$$

$$I_3 = 25 \text{ slug-ft}^2 \quad (33.9 \text{ Kg-m}^2)$$

$$B = 0.5 \text{ Gauss}$$

$$h = 0.7 \text{ lbf-ft-sec} \quad (0.944 \text{ Nt-m-sec})$$

$$K = 10^4 \text{ pole-cm}/(5 \times 10^{-4} \text{ Gauss/sec}) = 2 \times 10^{-8} \text{ Nt-m}/(\text{Tesla}^2/\text{sec})$$

K is chosen by calculating the describing function for a flip-flop control law and a system oscillation amplitude of about  $\omega_0$ . Note that K decreases as  $\omega$  grows and hence the system becomes less stable. Now, (a3) becomes

$$\phi_1 = 5019\Omega^2 - 97.7\Omega + 0.89 + K^2B^4 > 0 \quad (E27)$$

(E27) has no real zeros even for the worst case ( $K = 0$ ), so we need not concern ourselves with it further. We next look at (a5) and determine the maximum value of  $\Omega$  for which  $I_{3e}$  is a major axis (recalling that this is required by  $\phi_2$ )

$$\frac{h}{\Omega} + I_3 > \max(I_1, I_2) \quad (E28)$$

The result is  $\Omega_{\max} = 0.0278$  rad/sec.

Finally, we examine  $\phi_2$  (expression a4):

$$\frac{\phi_2}{KB^2} = \frac{-53315\Omega^4}{\phi_1} + \frac{5185\Omega^3}{\phi_1} - (47.6 + \frac{102.7}{\phi_1})\Omega^2 + 1.89\Omega \quad (E29)$$

We are interested in determining whether  $\phi_2 > 0$  for  $0.0278 > \Omega > 0$ . This is required if we are to have any stable region of operation at all. This task is somewhat simplified by first examining  $\phi_1$ . We see that  $\phi_1$  is relatively constant for this range of  $\Omega$ . In fact, for  $K = 0$ ,

$$(\phi_1 = 5015\Omega^2 - 97.7\Omega + 0.89) \quad (E30)$$

$$\phi_1(0) = 0.89$$

$$\phi_1(.01) = 0.515$$

$$\phi_1(.02) = 0.94$$

$$\phi_1(.0278) = 2.05$$

and

$$\phi_{1\min} = 0.418 \text{ at } \Omega = 0.00973$$

$K = 0$  is surely the worst possible case, since as K increases, so does  $\phi_1$  and thus  $\phi_2$  will increase if we are in the range  $0 < \Omega < 0.0278$ .

Now, (E29) has only two real roots. One is obviously at  $\Omega = 0$ , the other lies at about  $\Omega = 0.05$ . Between these roots  $\phi_2 > 0$ . Thus we have ensured a stable region of operation for

$$0.0278 > \Omega > 0.0 \quad (E31)$$

One may convince oneself of the truth of this result by returning to equation (E21), substituting values for the coefficients and then solving the resulting equation numerically for the roots  $s_i$ . It is, of course, a necessary and sufficient condition for stability that all the  $s_i$  lie in the left half plane.

Substituting into (E21) we obtain

$$3225s^4 + 57.7s^3 + (3687\Omega^2 - 45\Omega + 1.14)s^2 + (-23.8\Omega^2 + 0.944\Omega)s + (462\Omega^4 - 45\Omega^3 + 0.89\Omega^2) = 0 \quad (E32)$$

Numerical solutions for the roots of (E32) confirm the results (E31) obtained thru the Routhian analysis.

All of the results obtained in this appendix, up to this point, are only valid in a rigorous sense, for motion in the "neighborhood" of the equilibrium point. Otherwise the linearizations made in obtaining the system equations (E12) are not allowable. Nonetheless, considerable digital simulation experience indicates that the results obtained in this section are in fact applicable to the real (non-linear) system. Let us consider then the significance of these results. First of all, they indicate that the terminal attitude of the satellite must be such that the momentum bias points along the orbit normal, rather than opposite it. We remember that in the terminal condition the satellite has an angular velocity  $2\omega_0\mathbf{e}_n$ . If the satellite were to acquire "backwards", then the angular velocity  $2\omega_0\mathbf{e}_n$  would correspond to  $\Omega < 0$ , and we have seen that this equilibrium point is an unstable one. We have seen that there are no stable equilibrium points with very high angular velocities; the greatest being  $\Omega = 0.0278$  rad/sec. This means that, with the exception of possible limit cycle difficulties, this system should be well behaved and the control theory developed in the main body of this report provides for the positive despin of the vehicle. The author also wishes to note that he has observed no limit cycle behavior during extensive digital simulation of this system.

The reader is probably asking, at this point, "How about the equilibrium points II and III enumerated in Appendix D". The answer is that the author has not yet had time to perform a rigorous stability analysis for these points. However, on the basis of digital simulation it appears that they are not stable points unless  $\omega_1 = \omega_2 = 0$ , which is of course the case treated here.

Finally, we note that even the stable equilibrium states determined here present no real despin problems. The investigations here dealt, for simplicity, with a fixed external magnetic field. In fact, even in the worst case (an Equatorial orbit with the pitch wheel along the orbit normal) the Earth's field appears to cone about with a half angle of  $11.7^\circ$ . If the satellite is to remain in the equilibrium state, it too must cone about the orbit normal at frequency  $\omega_0$ . The control torques maintaining the equilibrium state (i.e. damping out disturbances - which is how the coning of the  $\mathbf{B}$  field appears to the system) are essentially dissipative in nature, since they oppose sensed velocities. The final result is then that even the small residual spin  $\Omega < .0278$  rad/sec along the momentum bias will be eliminated due to this previously unconsidered effect.

DISTRIBUTION:

Gerry Burdett

Robert Fowler

Henry Hoffman

Peter Hui

Seymor Kant

Jerry Langemaier

Jay Levy

Marty Lidston

Edward Mitchell

Helen Neumann

Harry Press

Henry Price

Moe Schneebaum

Dave Sonnabend

Stan Weiland

*Also, Wilson ✓*

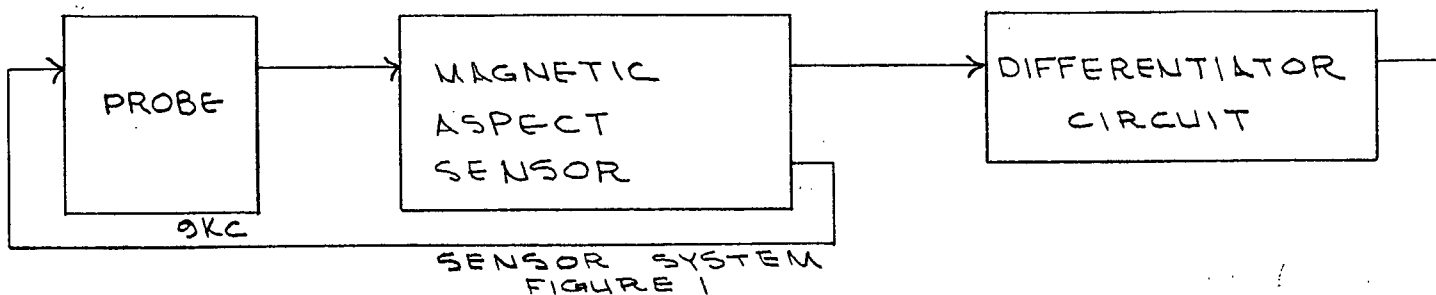
*3 copies North American ✓*

*Alfriend ✓*

## MAGNETOMETER NOISE MEASUREMENTS

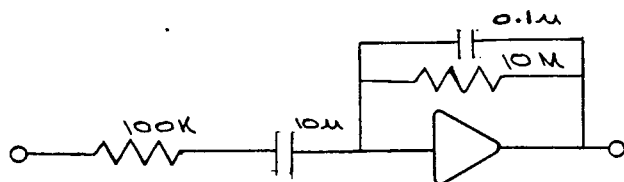
### PURPOSE OF THE STUDY

This study is part of an attempt to detect apparent changes in the earth magnetic field from a satellite during initial attitude acquisition. A system designed to accomplish this (Figure 1) consists of the Schonstedt RAM-5C-NB Magnetometer followed by a differentiator circuit. The output of the differentiator would be fed to a threshold detector of an attitude control system. This report evaluates the noise type and levels present in the magnetometer-differentiator combination.



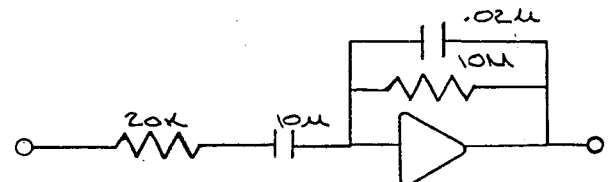
### GENERAL OPERATION OF THE MAGNETOMETER-DIFFERENTIATOR

The proposed magnetic aspect system (Figure 1) is composed of a probe and associated electronics (Magnetic Aspect Sensor) purchased from Schonstedt, and a differentiator circuit. The sensor provides a "d.c." output voltage proportional to the component of the magnetic field coaxial with the probe. The differentiator circuit not only differentiates, but provides attenuation over a range of frequencies outside of the range of vehicle rotation frequencies. Primarily, two circuits were used during the study, one with a corner frequency  $\omega_c$  of 1 radian per second and the other with a corner frequency of 5 radians per second. The approximate equivalent circuits are shown in Figure 2.



DIFFERENTIATOR WITH  $\omega_c = 1$

FIGURE 2a



DIFFERENTIATOR WITH  $\omega_c = 5$

FIGURE 2b

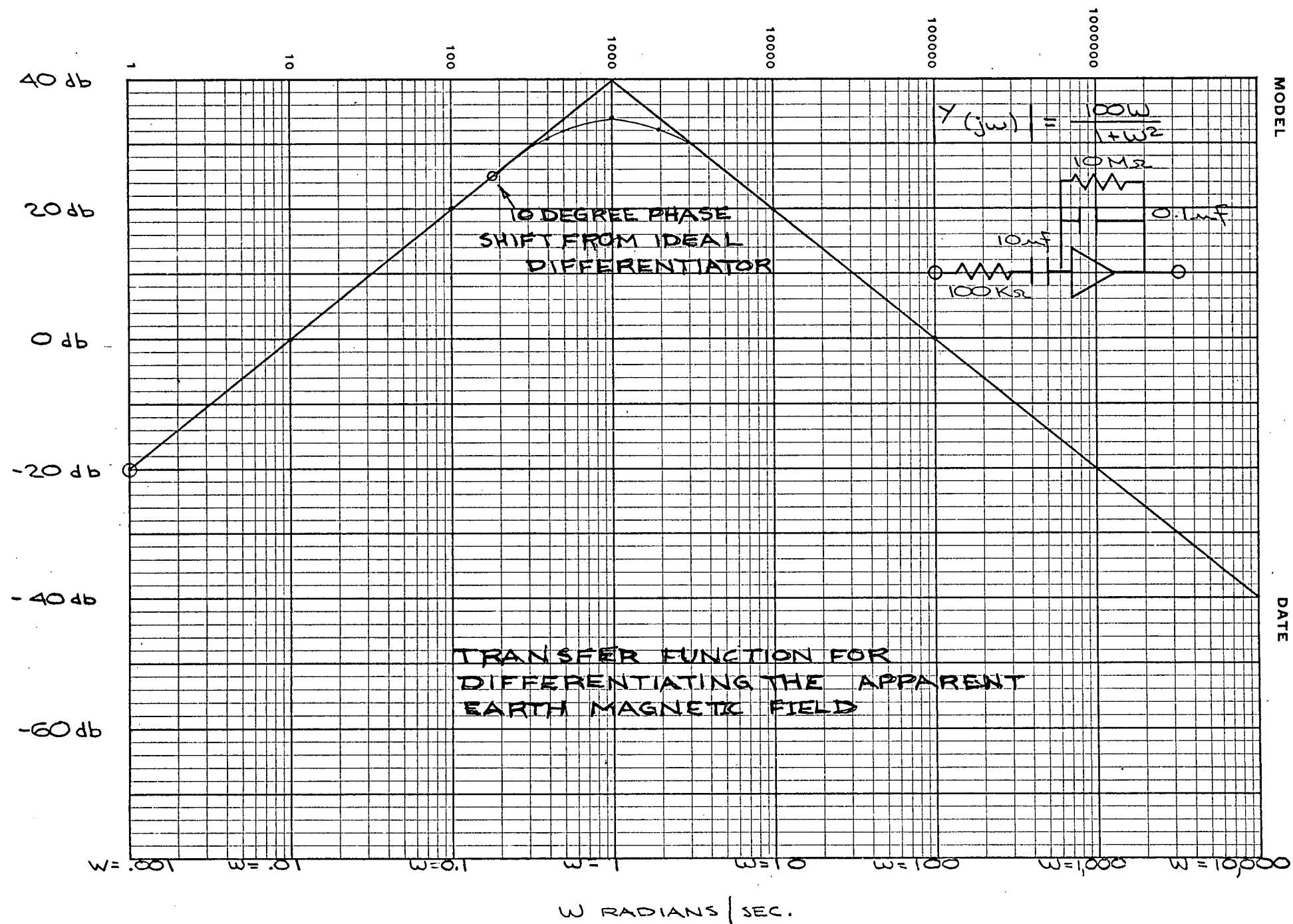


FIGURE 3

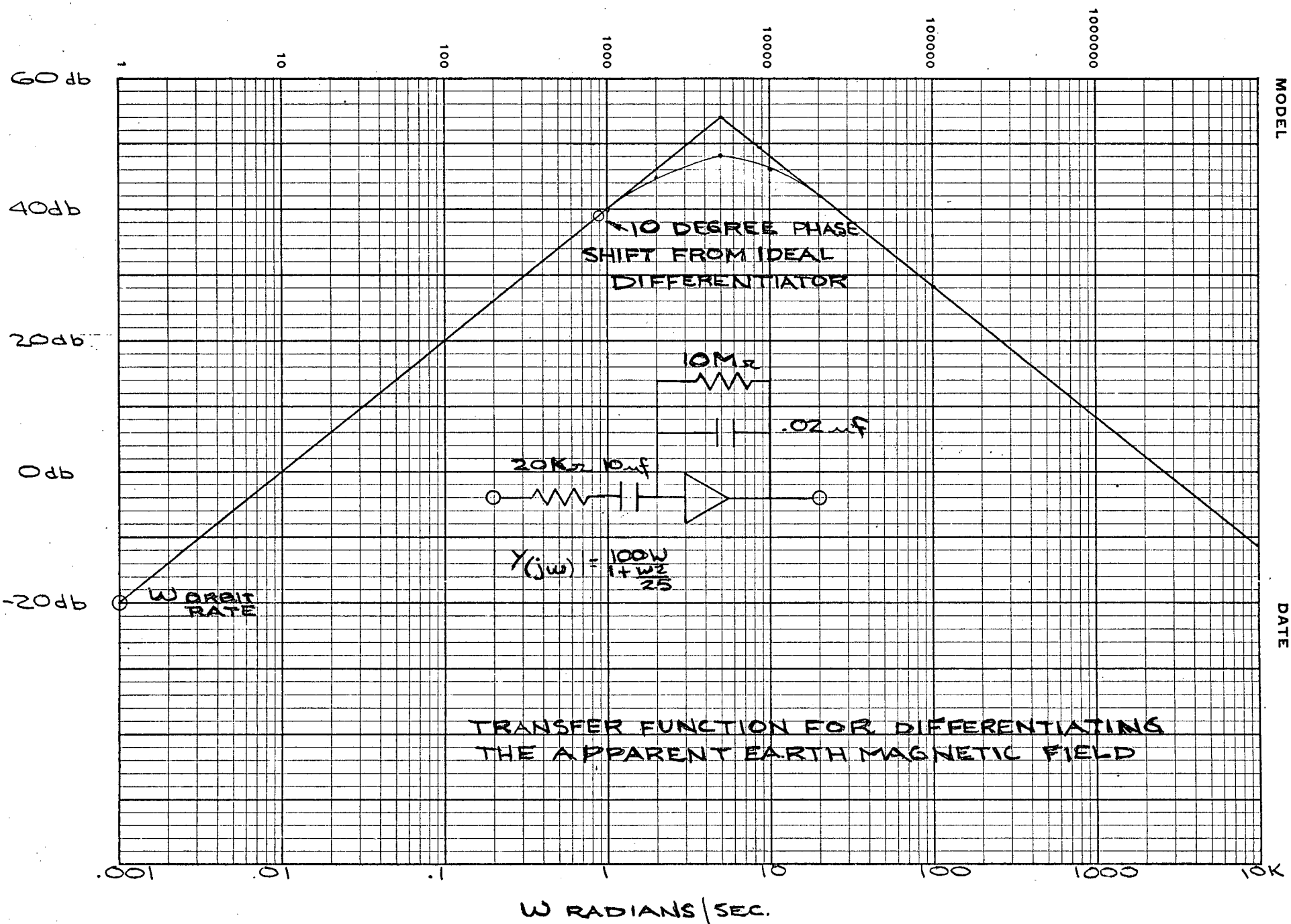


FIGURE 3b



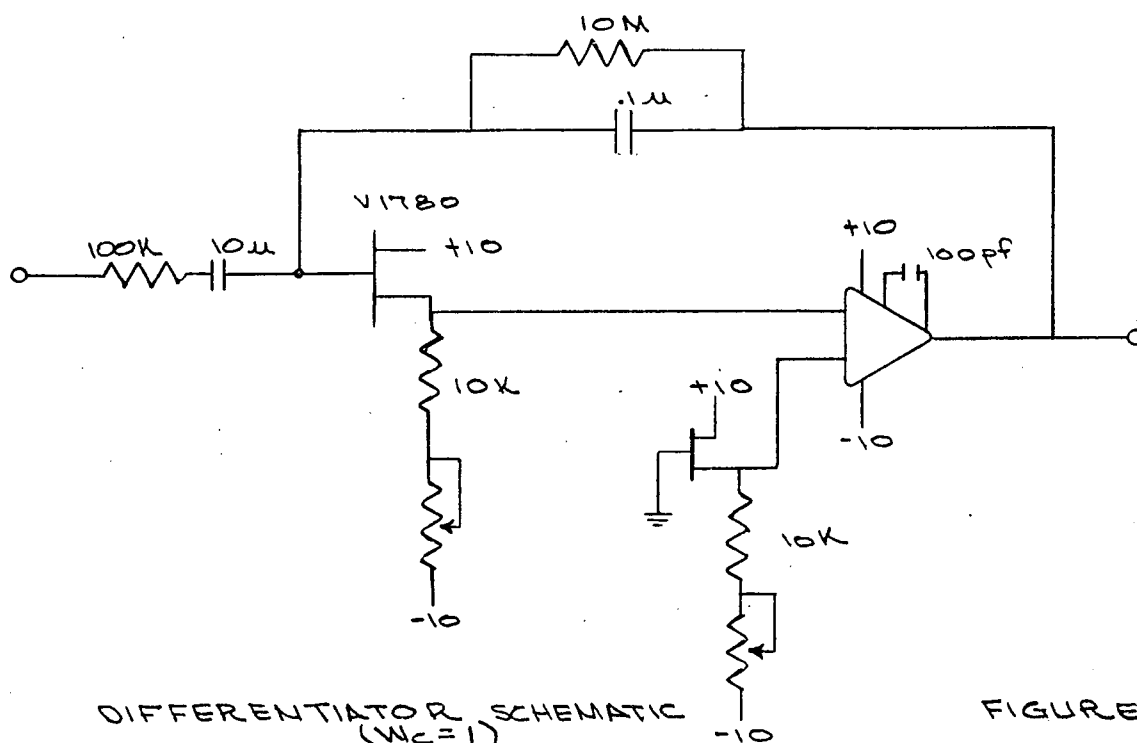
The mathematical representation is

$$Y(jW) = \frac{-j100W}{(1+j\frac{W}{W_c})^2} \quad ; W \text{ is in radians per second}$$

Figures 3a and 3b are the Bode plots corresponding to the circuits of Figures 2a and 2b. Zero db is defined equivalent to unity gain.

#### TEST RESULTS

Figure 4 is the actual circuit configuration of the differentiator with 1 radian/sec. corner frequency. Separate FET's were used. The circuit with a corner frequency of 5 radians/sec. employed the 2N3922 dual FET's.



Three magnetometers SN3881, 3882, and 3883 were used at various times during the testing; but for consistency, 3883 was subjected to each test.

The outputs of the  $W_c=1$  and  $W_c=5$  circuits were measured when these circuits were used in combination with magnetometer 3883. The two tests were not run simultaneously. The magnetometer was centered radially in a wooden cylinder which in turn was centered radially in an iron pipe. The pipe was then closed. A magnet external to the pipe supplied the magnetic field. The magnet produced a 2.3 volt magnetometer output. The output of the differentiators were recorded using a Brush recorder.

The peak to peak values obtained are

8mV for the  $W_C = 1$  circuit,  
80mV for the  $W_C = 5$  circuit.

Figures 5a and 5b are samples of the recordings from which the values were obtained.

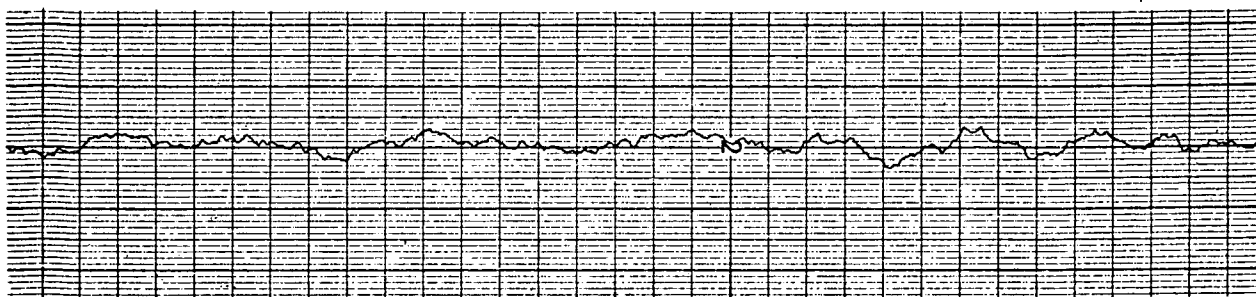
To determine the noise generated by the differentiator circuit, the output was measured with the input shorted. Both circuits were placed in a metal box and the outputs simultaneously measured using the Brush recorder. The peak to peak output was half a millivolt for the  $W_C = 1$  and 2 millivolts for the  $W_C = 5$  circuit.

The magnetometers themselves do not have identical noise characteristics. Figure 6 is a Brush recording showing the noise output from the  $W_C = 5$  circuit fed by each of the three magnetometers. Each of the magnetometers was tested in the pipe with the magnet supplying the same field in each case. A considerable difference between the noise levels of the magnetometers is apparent. Disturbances, some deliberately created, in the laboratory verify that the magnetometers and the differentiator were functioning during the measurements.

Two magnetometers, each in combination with a  $W_C = 1$  differentiator were tested simultaneously to show that spikes which were being observed on the oscioolgraph are not internally generated. Oscillographs obtained during the night hours also tend to confirm that the largest spikes are not internally generated. The night graphs are almost without the large spikes which are common in the data taken during normal working hours.

Oscillographs were run for 1 hour with the  $W_C = 1$  differentiator and then for 1 hour with the  $W_C = 5$  differentiator. These recordings show that noise with a period on the order of minutes is negligible by comparison with the amplitude of the noise envelope.

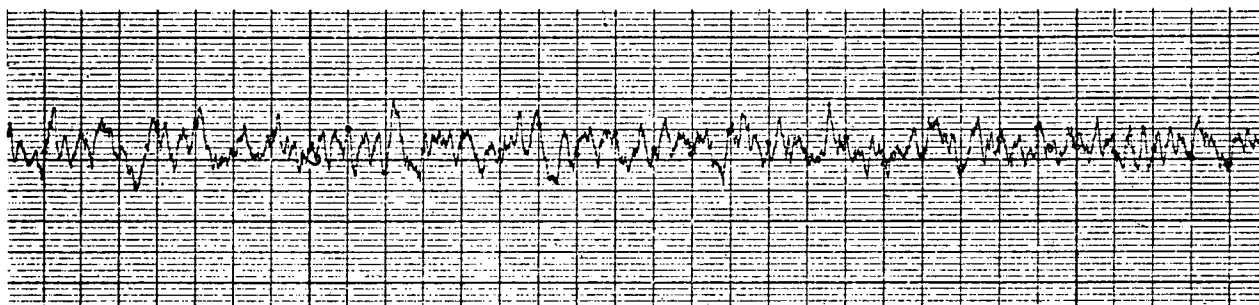
Root-mean-square (RMS) measurements were obtained to indicate the general level of the noise as a function of  $W_C$ . The measurements were obtained graphically from the Brush oscillographs. Three circuits were used in turn with magnetometer 3883. The magnetometer was enclosed in the pipe and the field supplied by a magnet external to the pipe. All three differentiators were of the same mathematical form, all had  $K = 100$ , and all had the same input capacitor and output resistor. With those restrictions, the noise levels may be considered to be a function of  $W_C$ . The equivalent circuits for two of the differentiators are Figures 2a and 2b, the third ( $W_C = 0.5$ ) is shown by Figure 7.



Vertical Scale: 1mV/small div.  
Horizontal Scale: 5mm/sec.

Noise Output of Differentiator with  $W_C = 1$  rad/sec. in  
Combination with Magnetometer SN 3883.

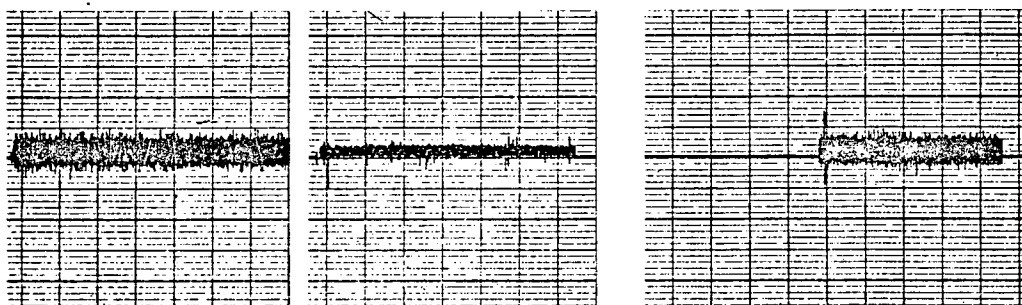
FIGURE 5A



Vertical Scale: 5mV/small div.  
Horizontal Scale: 5mm/sec.

Noise Output of Differentiator with  $W_C = 5$  rad/sec. in  
Combination with Magnetometer SN 3883.

FIGURE 5B



3882

3881

3883

Comparison of Noise Levels from Three Magnetometers.  
Output of Differentiator with  $W_C = 5$  rad/sec.

FIGURE 6

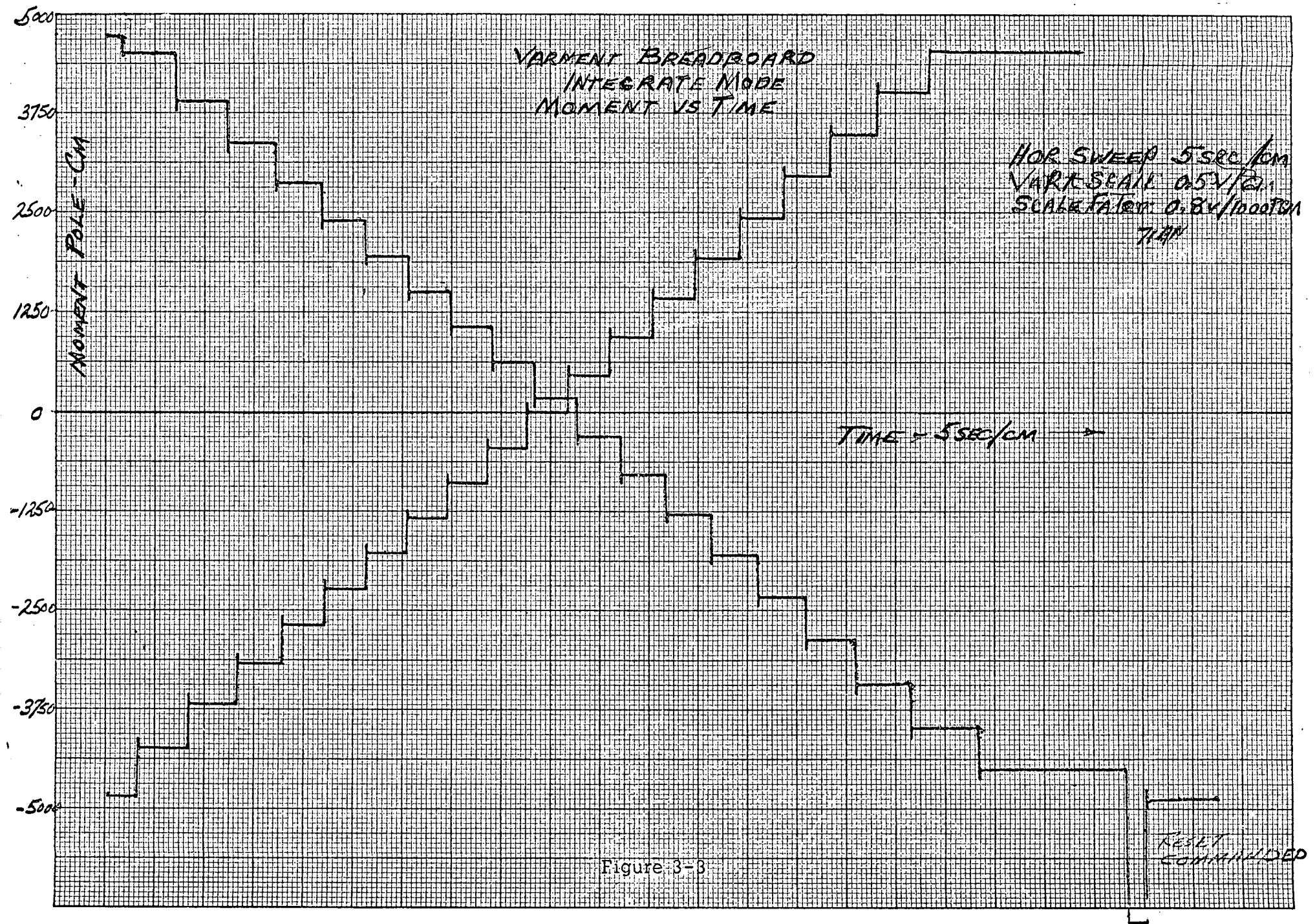
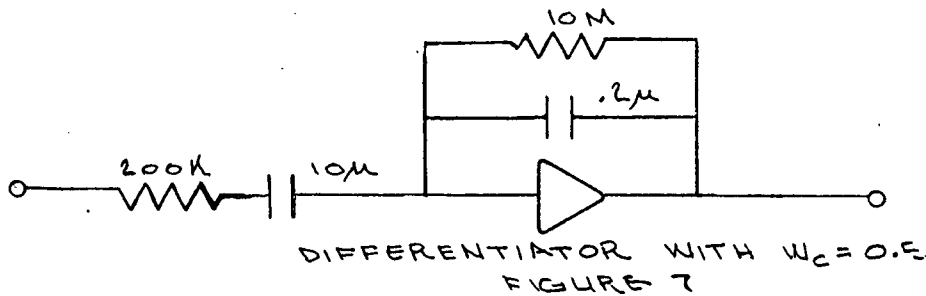


Figure 3-3



The results of the graphical analysis are given in Table 1.

$W_c$ radian/sec.	Magnetometer 3883 Output Volts d.c.	Differentiator Output Noise Millivolts RMS
0.5	1.6	0.6
1.0	2.3	1.3
5.0	2.3	8.1

TABLE 1

To obtain the RMS voltage graphically, the instantaneous value of the noise voltage is measured at 1 second intervals. The square root of the mean of the square of these measurements is the RMS voltage.

#### MAGNETOMETER OUTPUT CHARACTERISTICS

Tests show that the d.c. output impedance of the magnetometer is 3.6K ohms. The 20K ohm resistance shown in Figure 2b actually includes the 3.6K ohm output impedance.

At a frequency of  $W_c = 0.5$  radian/sec., the impedance of the  $10\mu$  farad differentiator input capacitor is 200K ohms, so there is negligible loading from d.c. to  $W = 0.5$  radian/sec.

Discussions with the vendor indicate that no electrical isolation problems exist in connection with the output of the magnetometers.

#### CONCLUSIONS

To get some idea of the feasibility of using the particular magnetometer-differentiator combination studied, some assumptions of physical conditions will be made.

For purposes of this study, a satellite will be assumed in a 500 mile high circular orbit. The RAM-5C magnetometer has a sensitivity of 4 volts per oersted. Assuming a maximum sea level field strength of 580 milliguass in the orbit plane, and an inverse cube variation of field strength with orbit radius; a voltage of  $\approx 1.6$  volts maximum would be present at 500 miles.

The Bode plots, Figure 3, give the voltage gain of the corresponding differentiators as a function of the frequency of a sinusoidal input. For simplicity, assume the satellite to be rotating about an axis which is fixed relative to the earth. Assume we are interested in rotation frequencies from 0.5 radians/sec. down to the orbit rate, and assume the orbit frequency is .001 radian/sec.

According to the Bode plots, a magnetometer signal at the orbit frequency would be attenuated by a minimum of 20db. For the 500 mile orbit, the peak differentiator output would be a maximum of  $\pm 160\text{mV}$ . If the angle between the magnetometer probe and the orbit plane were such as to reduce the field strength by a factor of 0.1, then the signal would be attenuated another 20db and the peak output of the differentiator would be  $\pm 16\text{mV}$ .

Suppose threshold detectors to be at the output of the differentiator. Based on the above discussion, the threshold levels might be set between  $\pm 16\text{mV}$  and  $\pm 160\text{mV}$ . Recall that the peak to peak noise values recorded on the oscillograph were

8mV for the  $W_C = 1$  circuit,  
80mV for the  $W_C = 5$  circuit.

The oscillographs show that the noise level measured at the output of the differentiator is dependent on the d.c. output voltage of the magnetometer. The reason is not known.

The study does not conclusively define the limitations of this particular magnetometer-differentiator combination. However, based on the measurements, the prospects for this combination appear promising.

# MAGNETOMETER NOISE MEASUREMENTS

Addendum to Report No. 90293, Aug. 27, 1971

Report No. 90293 gives the results of noise measurements for the Schonstedt RAM-5C-NB Magnetometer in combination with a differentiator circuit. As mentioned in that report, the noise level measured at the output of the differentiator is dependent on the d.c. output voltage of the magnetometer.

Oscillographs of the noise at the output of the magnetometer itself shows a dependence on the d.c. output voltage of the magnetometer. To obtain this more recent data, magnetometer 3883 was enclosed in the iron pipe and a constant magnetic field supplied by a magnet external to the pipe. The output of the magnetometer was coupled to the preamp of the Brush Recorder through a 10 $\mu$ f capacitor. Samples of these recordings are presented in the Figure.

A close look at the oscillographs show the noise level to be higher for a magnetometer output voltage of -2.4V d.c. than for an output voltage of +2.4V d.c. Since all of the data in Report No. 90293 was obtained for positive output voltages, the following question arises. If data were taken for negative and positive instead of just positive output voltages, might magnetometer 3881 be found to have greater p-p noise than 3883, instead of the other way around. To resolve this doubt, 3881 was tested in combination with the  $W_C = 5$  differentiator; the magnetometer was enclosed in the pipe and the field supplied by a magnet external to the pipe.

The following table shows the p-p differentiator output noise as a function of magnetometer output voltage. The data is only approximate due to the difficulty of defining p-p noise. However, this data clearly shows that the noise levels are well below the 80mV p-p measured with 3883.

## Differentiator Output Noise vs Magnetometer 3881 DC Output

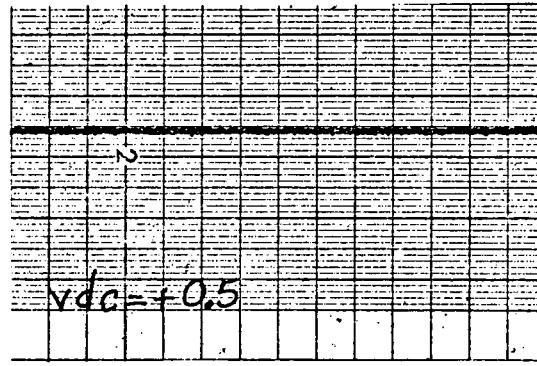
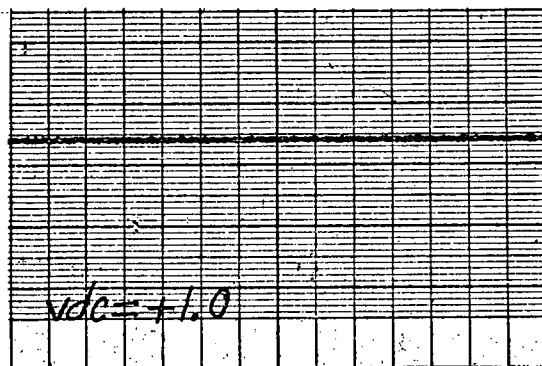
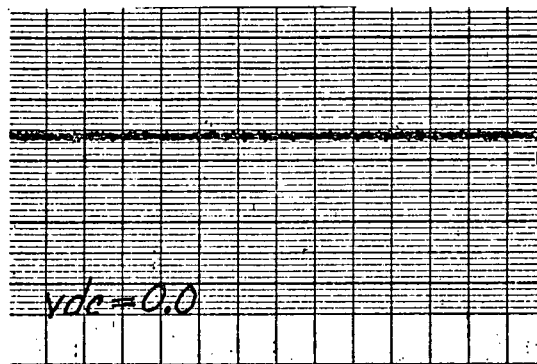
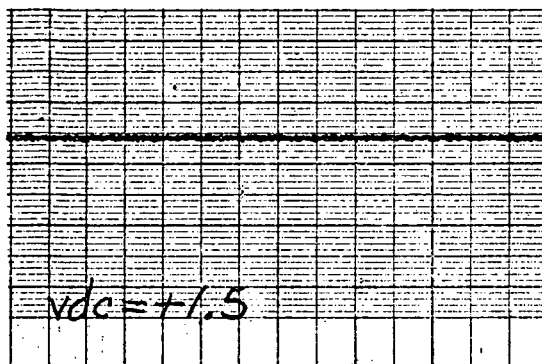
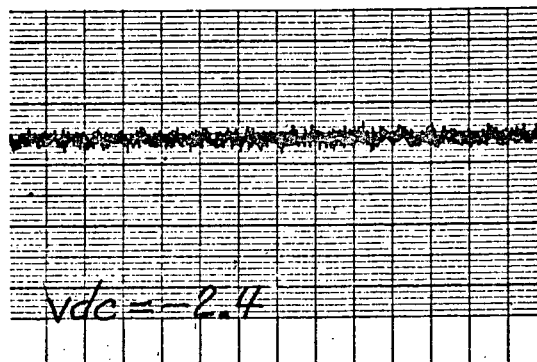
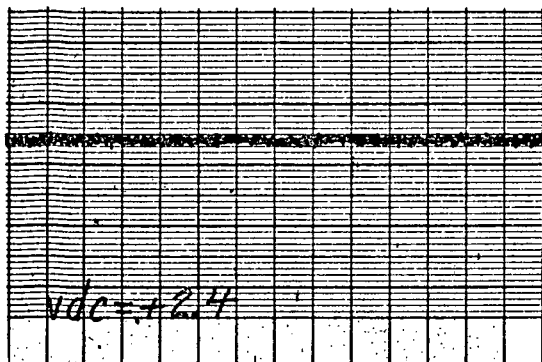
Magnetometer Output Volts DC	$W_C=5$ Differentiator Noise Output Millivolts p-p
-2.4	25
-2.0	25
-1.0	14
0.0	9
+1.0	20
+2.0	19
+2.4	35

## CONCLUSIONS

Noise levels vary from magnetometer to magnetometer. Noise levels also vary with field strength. Finally, and most important, if rates on the order of orbit rates are to be detected, the results of the tests with the  $W_C = 5$  differentiator are inconclusive. Simulation will be needed to provide the answer. However, if a relay were installed to convert the  $W_C = 5$  differentiator to a  $W_C = 1$  differentiator during acquisition, detection at orbit rates should be feasible.

Jay Levy  
ITHACO, Inc.  
735 W. Clinton Street  
Ithaca, New York 14850





horizontal scales:  
20mm/sec.  
vertical scales:  
1mV/small division

Output Noise Voltage for Various DC Output Voltages for  
Magnetometer S/N 3883

### III Electronics for Control of Variable Permanent Magnets

1.0 Introduction

2.0 Control Electronics

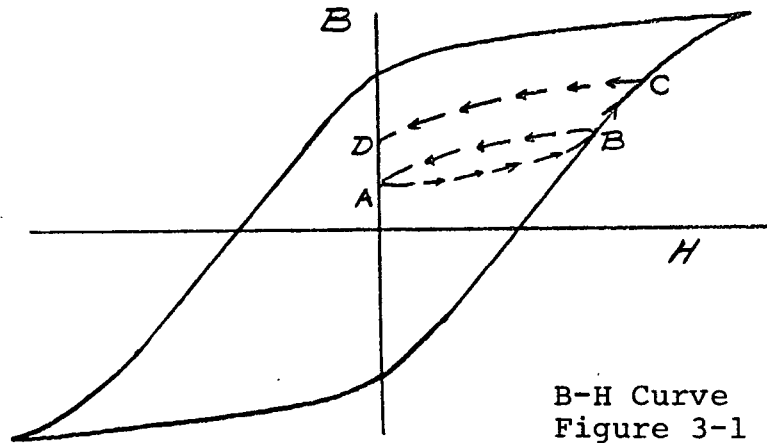
3.0 Variable Permanent Magnet Breadboard Controller

### III Electronics For Control of Variable Permanent Magnets

#### 1.0 Introduction

In this section the circuitry is described for controlling the state of a variable permanent magnet as a linear function of an input variable. The input variable can be either a control voltage, (for control applications) or a time interval (for magnetic balancing applications).

The control circuitry consists of a Hall sensor that senses the state of the magnet, and in a feedback loop compares it with the input voltage. The high gain feedback loop forces the sensed moment to agree with the input voltage. Small deadbands are used so that once the correct moment is achieved the magnet drive is automatically turned off. The circuitry and accuracy of this method are the subject of this section.



The B-H curve in Figure 3-1 illustrates the inter-relationship between a permanent bar magnet and an external field.

In changing the permanent induction of the bar from A to D the path ABCD must be traversed. An external H field corresponding to point C must be applied and when removed the induction level in the bar will relax to point D. The continuous application of an external field less than that associated with point B, once the magnet has been cyclically magnetized, will not alter the permanent induction. The minor loop AB is designated the recoil energy and the slope the recoil slope.

The average slope of the recoil permeability is constant for a cyclically magnetized bar up to approximately 80% of the saturated induction level and thereafter extremely non-linear.

For a bar magnet wound with a suitable coil to permit varying the induction level it is possible to predict the residual induction which will result after removing the magnetizing current. In the Varment system this is accomplished by sensing the magnetizing coil current and scaling it to cancel the recoil induction as measured by the Hall sensor.

## 2.0 Control Electronics

The Control Electronics for setting the state of the variable permanent magnet consists of a bipolar power bridge circuit, which supplies the necessary current with the proper polarity to the magnet coil, operated by one of two threshold circuits. See the Block Diagram (Figure 3-2).

Thresholding is achieved by two separate modes of operation designated Analog and Integrate Mode. In either mode the magnet state is continuously monitored by a Hall sensor and the current in the magnetizing coil is sensed for both magnitude and direction. The Analog Mode, which is the most straight forward, permits setting the state of the magnet in reference to an input analog voltage.

The analog input, Hall output and the current correction voltage are summed, properly scaled, and the output of this summing amplifier operates the threshold circuits which have built in hysteresis.

The amount of hysteresis does not affect the resolution but does limit the minimum incremental moment that may be obtained. Thus far the obtainable resolution has been found to be 2% of the maximum moment if the final desired moment is approached from the same direction each time. For random approaches the resolution has been found to be approximately 4%. Therefore in order to assure that the desired commanded moment will yield a differential output between the Hall voltage, the analog input and the recoil correction that is within the deadband of the thresholding circuit it is necessary to insert hysteresis

greater than 4% of the maximum capability. Otherwise the system could continuously switch the current on and off in a futile attempt to make the Hall voltage agree with the commanded analog voltage.

In the integrate mode the Hall voltage is summed with a D.C. voltage utilizing an operational amplifier with several seconds lag. It is only necessary that the D.C. voltage exceed the threshold to operate the magnet but the amplitude and time lag determine the ultimate accuracy with which any desired moment can be attained.

Upon commanding the system to the integrate mode and energizing the magnet driver the magnet state is automatically changed a fixed amount equal to the threshold in fixed increments of time until the maximum moment is reached. Should the desired moment fall between any two increments it would be necessary to command a momentary set voltage into the system that exceeds the threshold. When removed the magnet would then be driven to the desired state. To maintain this state it would then be necessary to de-energize the driver prior to the next incremental state change.

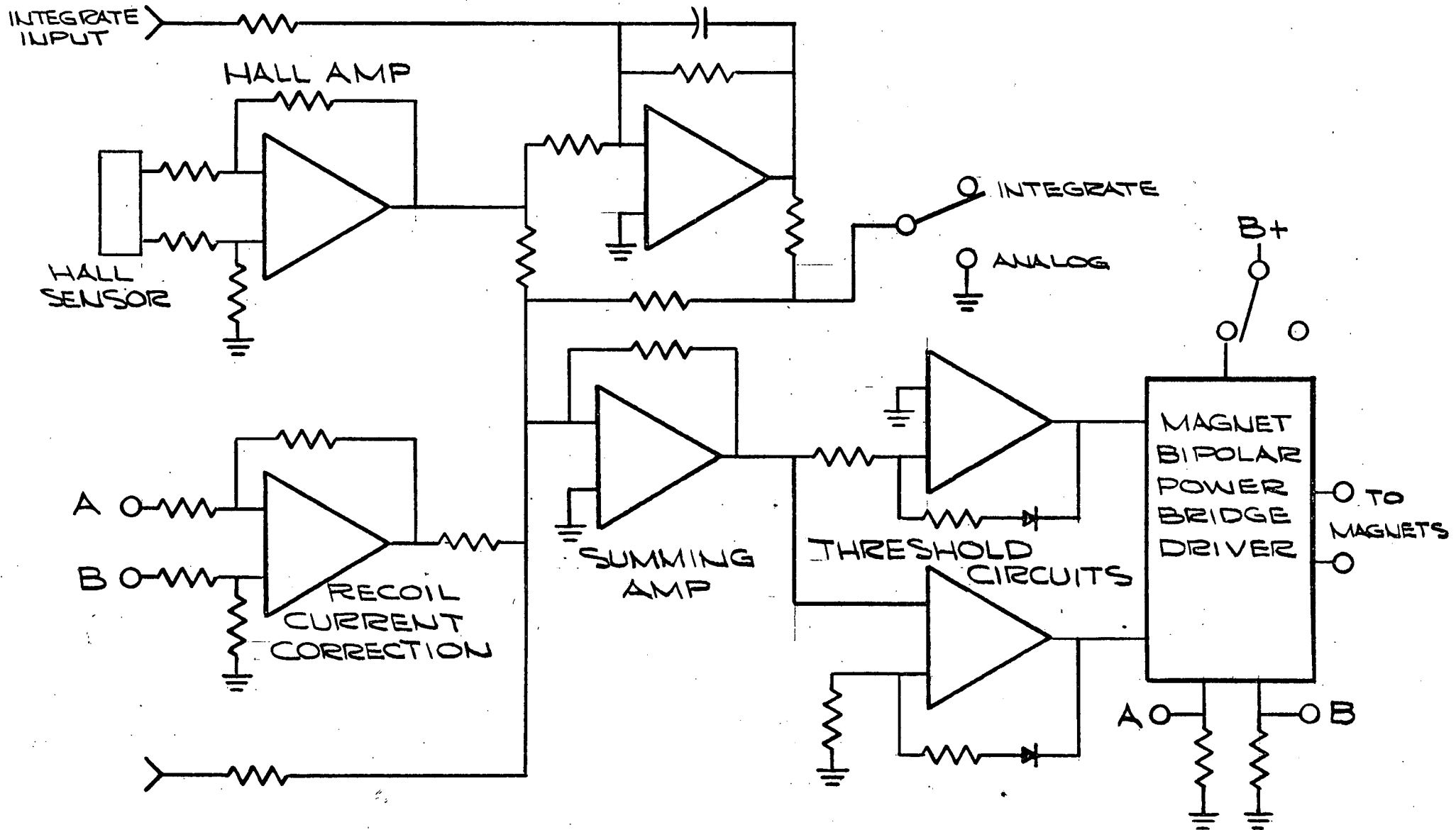
As an example consider a magnet capable of 10,000 p-cm initially at a 1,000 p-cm state with a desired new state of 7300 p-cm. Let the threshold be set at 500 p-cm and the integrator time constant and input set so that the state is changed 500 p-cm every ten seconds. The system would require 120 seconds to attain 7,000 p-cm and the momentary set command would be inserted at 126 seconds from the initial integrate command. The 7300 p-cm state would then be maintained for the next ten seconds during which time the driver would be de-energized.

### 3.0 Variable Permanent Magnet Breadboard Controller

A breadboard control system consisting of a power supply card and magnet control unit was built and trimmed to control a ten inch elliptical magnet made from P-6 material. Schematics & layouts of these two cards are included in this report.

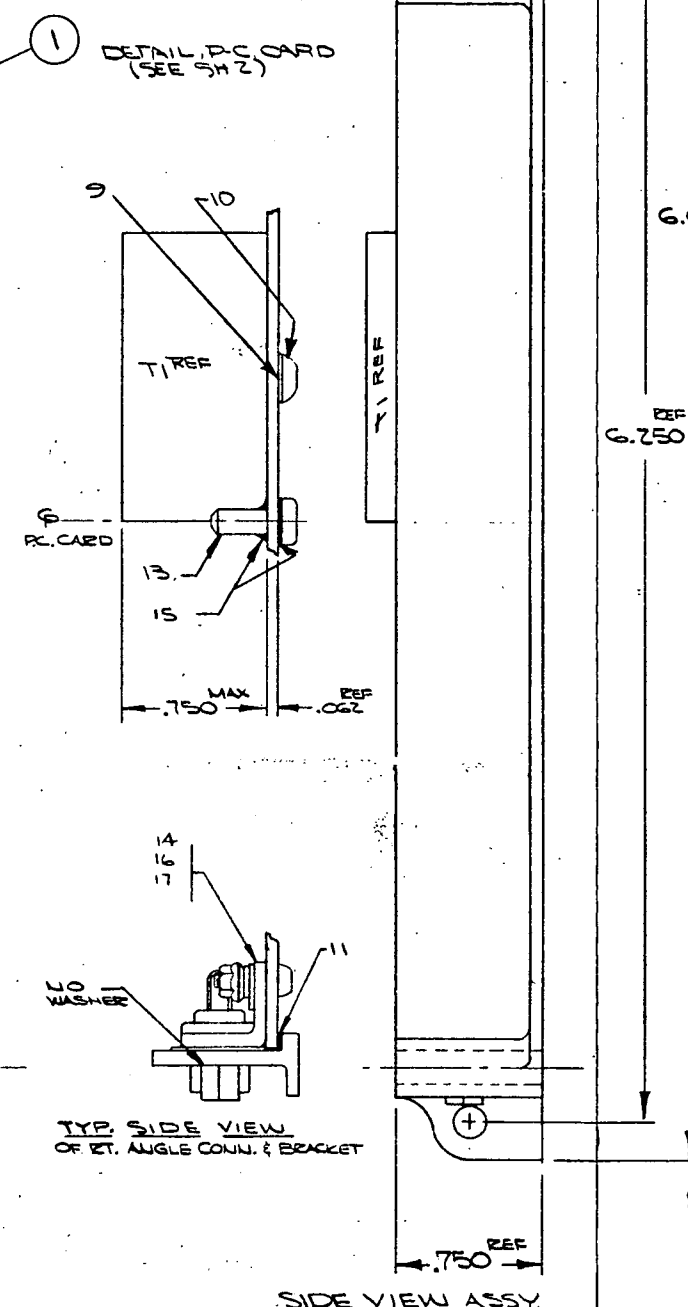
The magnet was found to have a maximum moment capability of  $\pm 6300$  pole-cm. It was determined experimentally that utilizing the recoil current correction was satisfactory with only minor current limiting over 80% of the maximum capability of the magnet. It was also determined that attempting to reduce the threshold to better than 4% of the available moment required careful gain matching and trimming.

The X-Y plot show in Figure 3-3 show the control circuit and magnet being operated in the integrate mode starting from both the positive & negative moment to determine the linearity of the incremental moment changes. The threshold for this curve was set at  $\pm 8\%$  or approximately 400 p-cm increments.



MAGNET CONTROL BLOCK DIAGRAM  
FIGURE 3-2




FOLDOUT FRAME 2



NOTES:

- 
- TYPICAL INTERFACIAL CONNECTION  
(POINTS #1 THRU #13)

SEE SEPARATE PARTS LIST

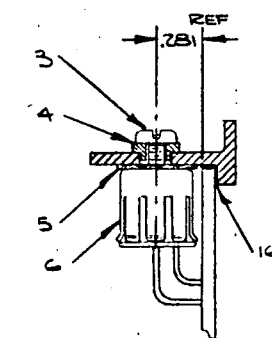
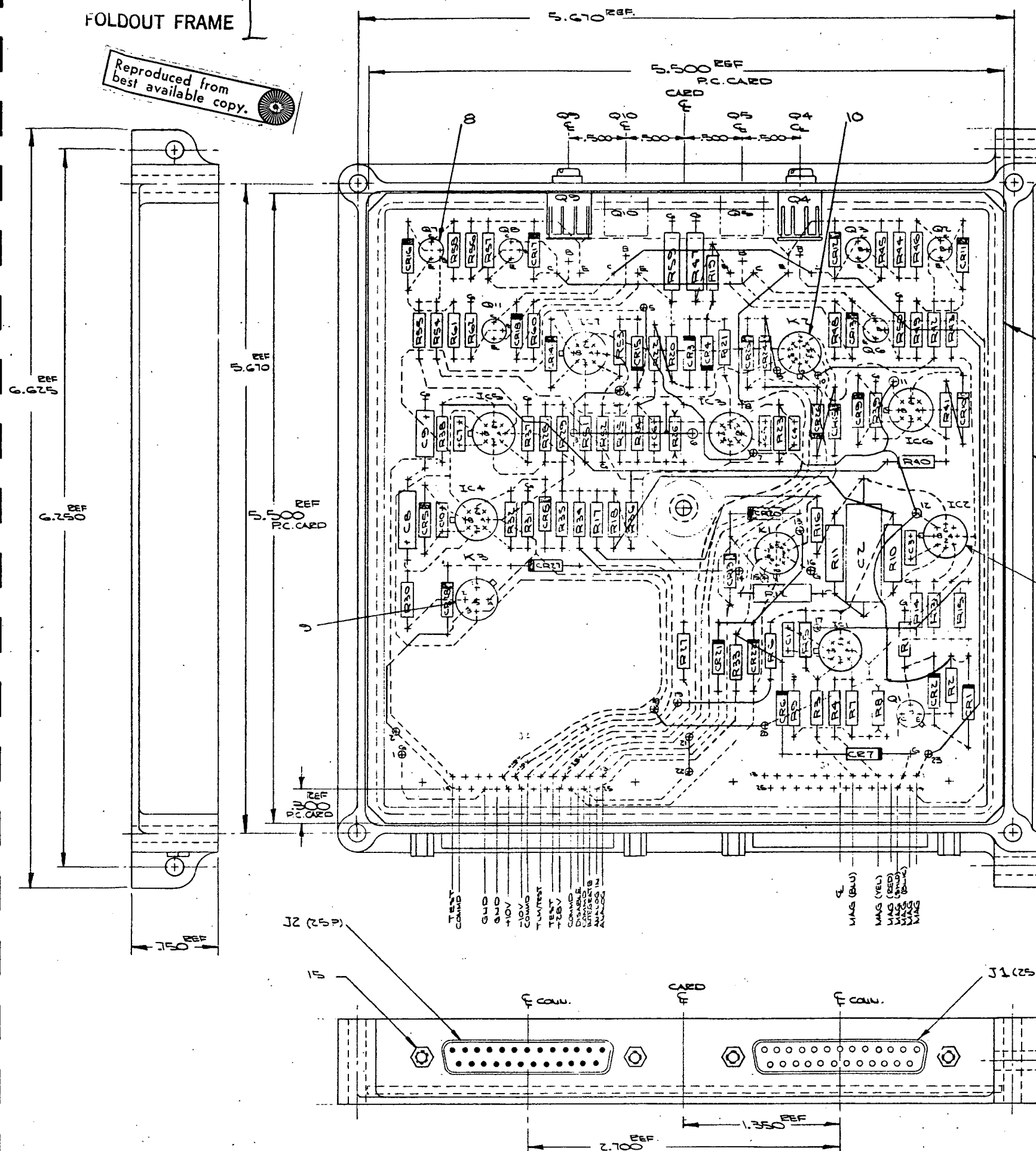
		MATERIAL: SEE SH 2		MODULE, POWER SUPPLY		ITHACO, INC. ITHACA, N. Y.	
		FIN: SEE NOTE 		FMF: JOB# 10-2460		CODE IDENT. NO. 26502	
		SCALE: 		DRAWN BY: TESTER NOV 10, 1971		D SK-00193	
ITEM 522 34-0000191 PS-1		UNLESS OTHERWISE SPECIFIED DIMENSIONS ARE IN INCHES TOLERANCES ON		CHECKED BY:  11-19-71			
REFERENCE DWG USED ON		FRACTIONS DECIMAL ANGLES		APPROVAL: DFTG ENG WAA			
1TH-24M APPLICATION		= 1/64 = .010 = 1/2"		ISSUE DATE: 11-19-71		SHT 1 OF 1	



FOLDOUT FRAME

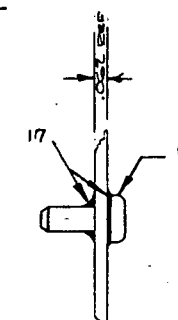
Reproduced from  
best available copy.

FOLDOUT FRAME 2



SIDE VIEW  
TYP INSTALLATION  
Q4, Q5, Q9, Q10

① DETAIL P.C. CARD  
SEE SH.2

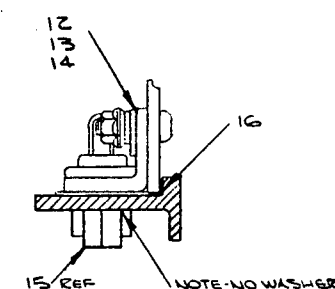


MTG CTR OF CARD

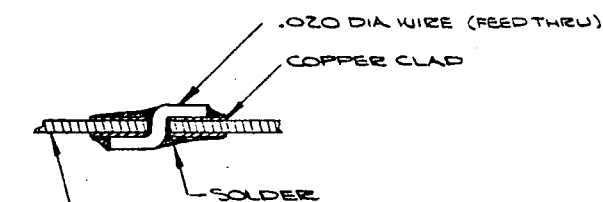
(G1) ASSEMBLY

NOTES:

1. FORM DIODE LEADS PER A 10315.
  2. ASSEMBLE COMPONENTS PER MOPS 30.3
  3. SECURE LARGE COMPONENTS PER M3FC PROC 257 PRIOR TO CONFORMAL COATING.
  4. ASSEMBLE P.C. CARD TO FRAME PER MOPS 30.35.
- △ ASSEMBLY TO BE CONFORMAL COATED PER MOPS 30.2 AFTER CARD TEST.



SIDE VIEW OF  
RT. ANGLE CONN. & BRKT



TYPICAL INTERFACIAL CONNECTION

POINTS  $\oplus 1$  THRU  $\oplus 23$

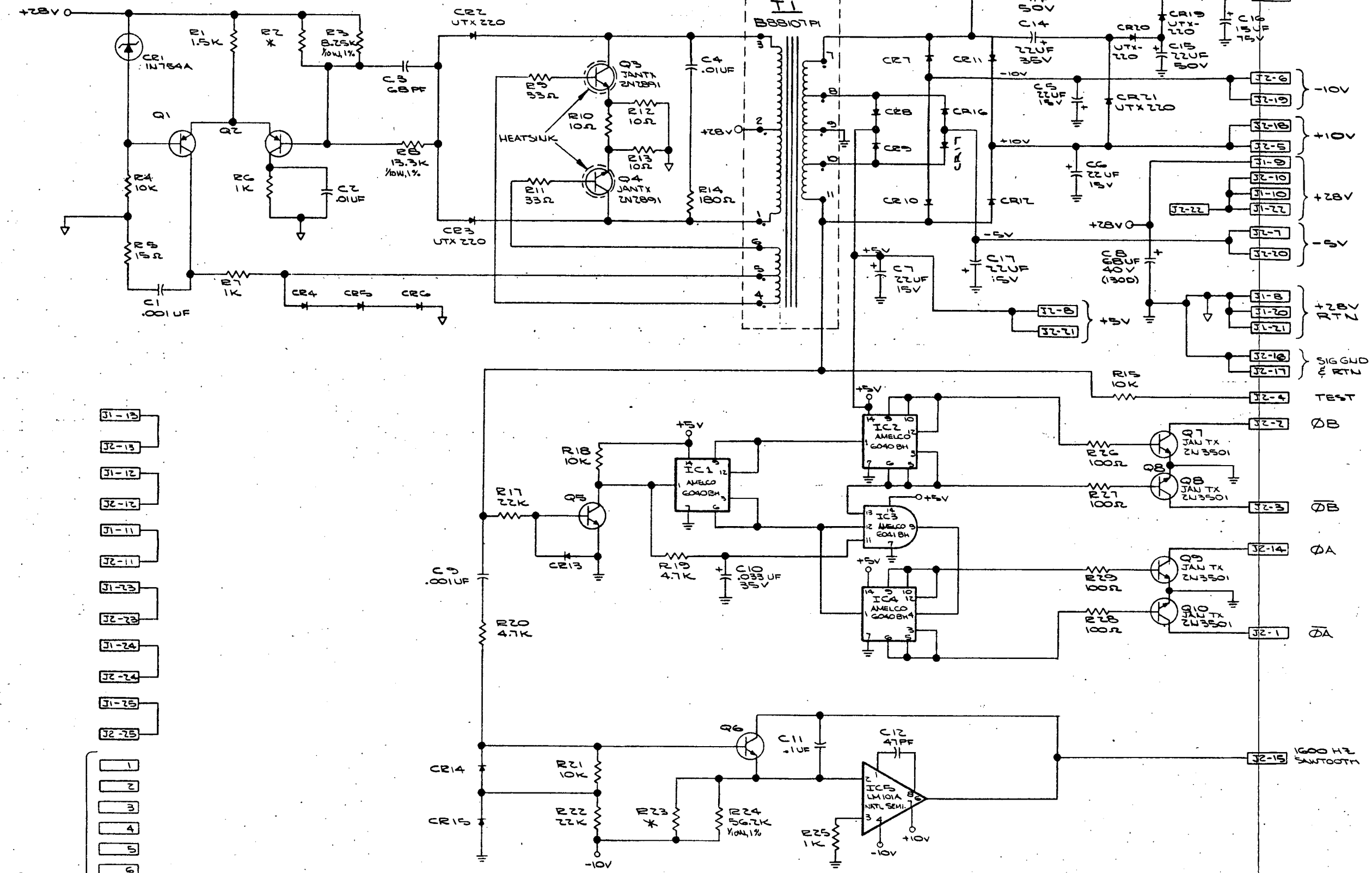
SEE SEPARATE PARTS LIST

		MATERIAL: SEE SHEET 2		MODULE, VARMINT		ITHACO, INC. ITHACA, N. Y.	
		FIN: SEE NOTE A					
		SCALE: 2/1		FMF JOB# 10-2099			
		UNLESS OTHERWISE SPECIFIED DIMENSIONS ARE IN INCHES TOLERANCES ON		DRAWN BY: <i>W. J. Shaw, Jr.</i> 11-18-71		CODE IDENT. NO. 2650	
ELEM. SK-DOOKG VMT-1		FRACTIONS DECIMALS ANGLES		CHECKED BY: <i>Wm. J. Shaw</i> 11-19-71		D SK-00222	
REFERENCE DWG		= 1/64 = .010 = 1/2°		APPROVAL: DFTG. <i>W</i> ENG 484		ISSUE DATE: 11-19-71	
APPLICATION						SMT OF	

FOLDOUT FRAME 1

FOLDOUT FRAME 2

REVISIONS				D SK-00191	
ZONE	SYM.	DESCRIPTION	DATE	SHT	OF 1



NOTES:

- UNLESS OTHERWISE SPECIFIED:  
A. - ALL CAPACITORS ARE MYLAR, GE 63F  
- VALUES IN PPS ARE STYLE CKR  
- POLARIZED ARE SOLID ELECTROLYTIC  
- SPEAGUE 3500's  
B. - ALL DIODES ARE JAN TX 1N4148  
UTX ARE UNIDODE TYPE  
C. - ALL RESISTORS ARE 1/4W, 5% STYLE RC07  
- \* INDICATES TRIM, VALUE TO BE  
SELECTED AT TEST.  
- 1/4W, 1% ARE STYLE RNRE55H  
D. - TRANSISTORS -  
NPN ARE JAN TX 2N2222A  
PNP ARE JAN TX 2N2907A  
E. CONNECTORS  
J1 CANNON DBM 25P-K  
J2 CANNON DBM 25S-K

- J1 SPARES
- 1
  - 2
  - 3
  - 4
  - 5
  - 6
  - 7
  - 14
  - 15
  - 16
  - 17
  - 18
  - 19

MATERIAL		ELEM. DIAG.		POWER SUPPLY		ITHACO, INC.	
FIN:		SCALE:		FMF: JOB# 10-7460		ITHACA, N. Y.	
UNLESS OTHERWISE SPECIFIED DIMENSIONS ARE IN INCHES TOLERANCES ON		DRAWN BY: D. Woolley		OCT 4, 1971		CODE IDENT. NO. 26502	
FRACTIONS DECIMALS ANGLES		CHECKED BY: [Signature]		11-18-71		D SK-00191	
REFERENCE DWG USED ON		APPROVAL: DFTG. [Signature]		11-18-71		SHT 1 OF 1	
APPLICATION		± 1/64 ± .010 ± 1/2°		ISSUE DATE: 11-17-71			



## IV HORIZON SCANNER BREADBOARD

### 1.0 Introduction

### 2.0 Description of the X Scanner

### 3.0 Operational Description

### 4.0 Figures

Appendix #1 Patent Disclosure - Horizon Sensor - Any Altitude Satellite

Appendix #2 Patent Disclosure - Horizon Sensor - Any Altitude Satellite

Appendix #3 Report #90274

Appendix #4 Report #90276

## IV HORIZON SCANNER BREADBOARD

### 1.0 Introduction

As a part of the work under the subject contract, a demonstration breadboard of a new proprietary horizon scanning system developed by ITHACO was fabricated. The purpose of this breadboard is to illustrate the adaptation of this "X Scanner" to an existing Bendix Reaction Wheel.

There are many solutions to solving the circular body (Earth) edge scanning problems. Complexity should be avoided.

We think this has been done in the following description of the "X Scanner". The Patent Disclosure, Appendix #1 and #2, gives a detailed description of the scanner design and detector arrangement.

The basis for this design is to keep the system to its simplest, lightest and most reliable configuration. In general, the fewer the number of parts, the less there is to get out of order.

### 2.0 Description of the X Scanner

This system consists of one reaction wheel which mounts the optical scanner parts. This reaction wheel mounts the scanning double dove prism so that there is only one set of bearings and one scanning optical element. The single window, one sealing joint, is mounted rigidly to the case. The lens is also rigidly mounted to the case, as is the bolometer (or detector system), so that the optics cannot move or jump in relation to each other.

The scan prism drive reaction wheel is oriented so that its axis of rotation is parallel to the flight axis, the center of the earth.

The detector system, as explained in Appendix #2, consists of three detectors in the shape of a right triangle with a flake at each apex. This is required because the double dove prism, being set at 45° or close to it (this can vary due to requirements), rotates the image at twice this angle. It was necessary to have two flakes contact the earth at the same time for Sun control or compensation.

### 3.0 Operational Description

The scan pattern is such that one leg of the "X" crosses the earth with  $180^\circ$  rotation of the reaction wheel and the other leg with the next  $180^\circ$  rotation of the wheel. With the prism tilted  $45^\circ$  to the axis, the first  $180^\circ$  rotation crosses the earth and then the second  $180^\circ$  rotation has the prism tilted  $90^\circ$  from the first position. In this manner the common flake and the number 1 apex flake cross tangent to the earth on the first  $180^\circ$  rotation, and the common flake and the number 2 apex flake cross tangent to the earth on the next  $180^\circ$  rotation of the prism.

In this manner one reaction wheel, one window, one prism, one lens, one detector and preamp will give a complete scan report on one revolution of the reaction wheel. The line of sight contact is tangential to the earth for the pair of flakes. Also, the line of sight of this optical system is in line with the optics, which means good optical performance (this is an improvement over some previous systems).

The mathematical analysis is given by Appendix #3 (Report #90274) and Appendix #4 (Report #90276).

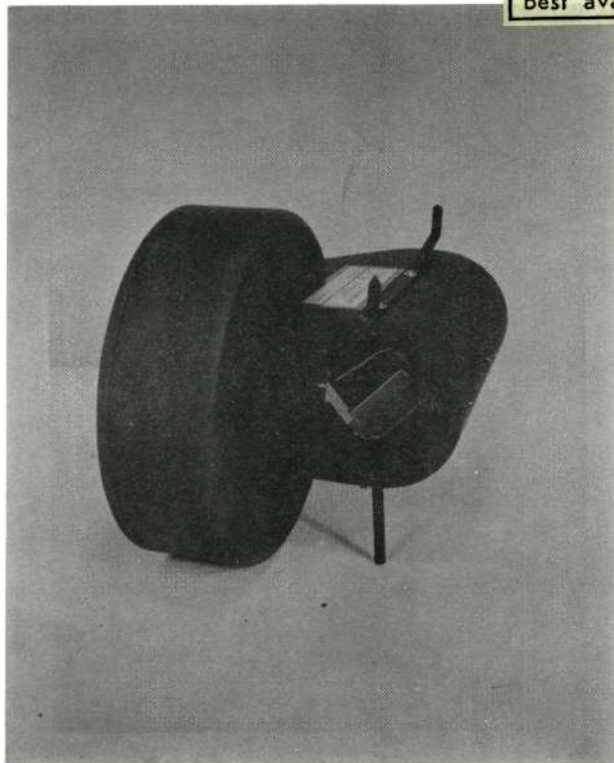
- 4.0 Figure IV-1 shows the demonstration model and the double dove prism. The large diameter at the left simulates an 8" reaction wheel. This shows the prism without any window.

Figure IV-2 shows the synchronous type scanner with a small plain window. The prism can be quite close to the reaction wheel.

Figure IV-3 shows the elliptical orbit scanner with a dome to cover the wide angle of this scan. The large distance between the prism and reaction wheel is required for the line of sight to clear the reaction wheel case for the lower altitudes.

**Preceding page blank**

Reproduced from  
best available copy.



**Figure IV-1**  
Scanner Without Window  
(to show prism)

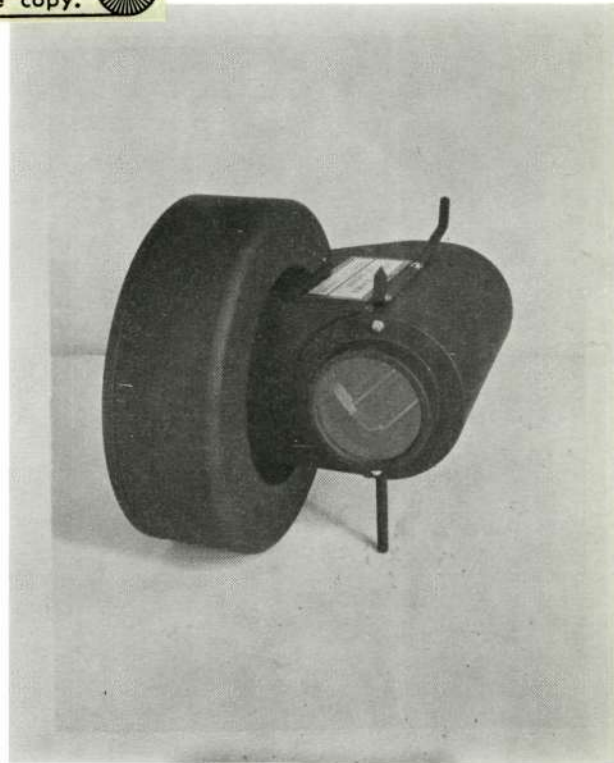


**Figure IV-2**  
Synchronous Orbit Scanner  
(with flat window)

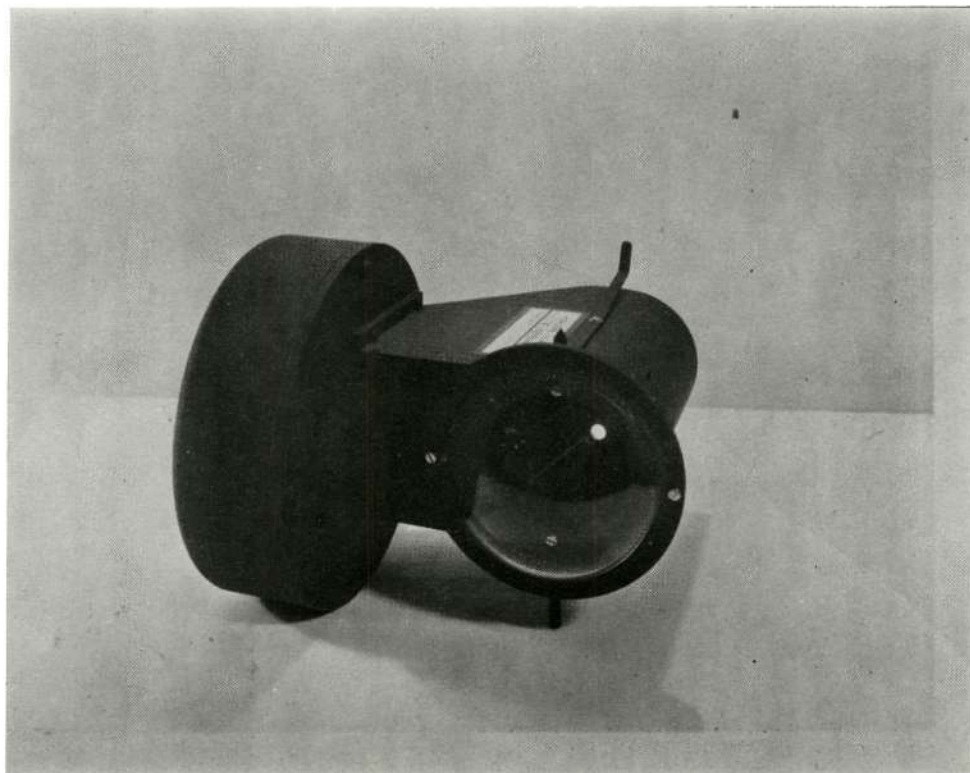


**Figure IV-3**  
Elliptical Orbit Scanner  
(with dome)

## PATENT DISCLOSURE

## HORIZON SENSOR - ANY ALTITUDE SATELLITE

Purpose - This horizon sensor is to operate at any altitude to the earth from approximately 500 N. Mi. out to greater than 24,000 N. Mi. within an accuracy of 0.1 degree.

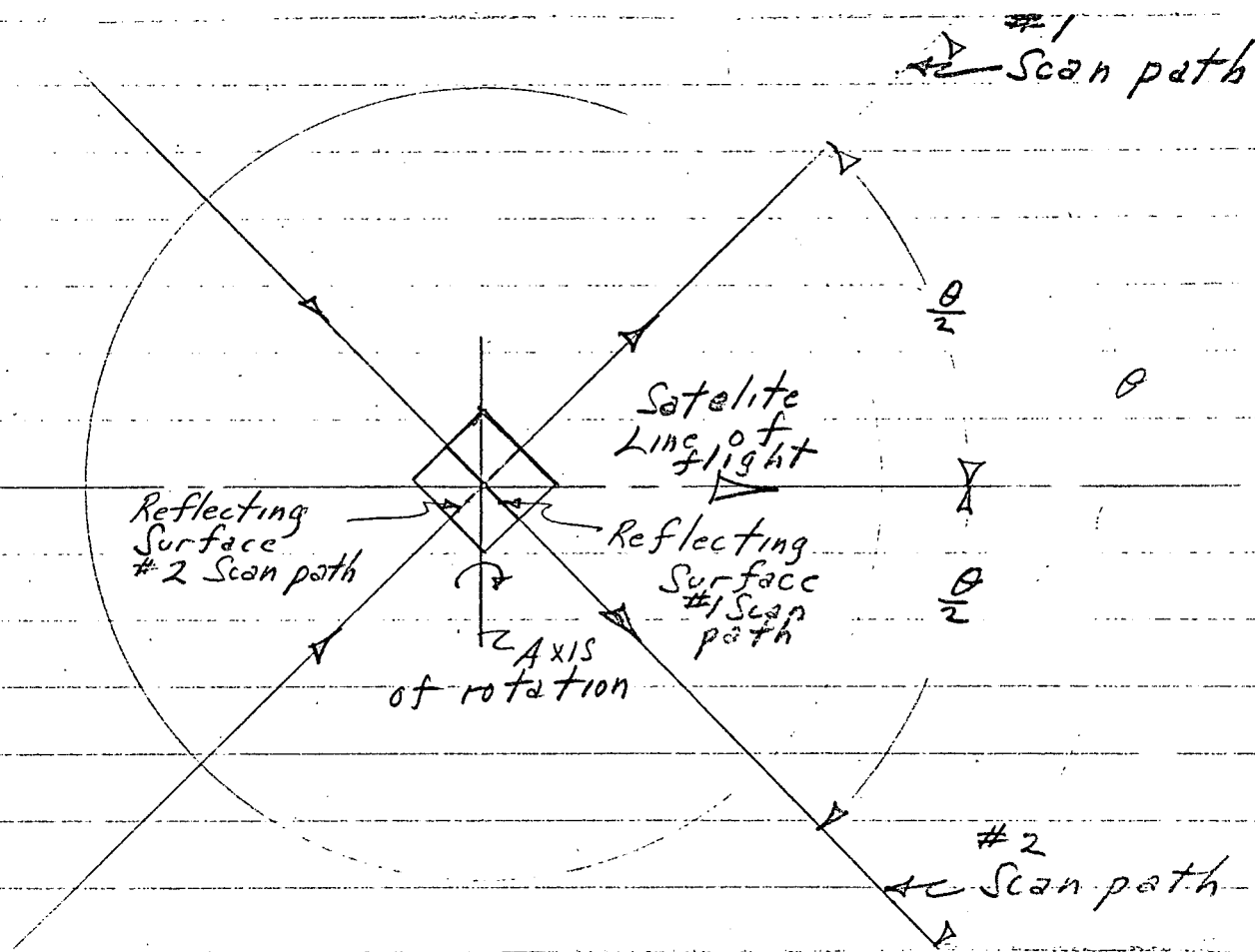


FIGURE I

Invention - This invention describes a scanner, single head consisting of a detector, a lens system and a scanning prism mounted on an axis of rotation shown basically in Figure I. This scans two paths at an angle  $\theta$  to each other and at  $\theta/2$  to the line of flight. The angle  $\theta$  in the sketch is shown as  $90^\circ$  to illustrate.

This accomplishes the purpose of controlling both Pitch and Roll with one scanner (previous systems used two scanners).

Invented by

Kennard Watson Harper April 1, 1971

Witnessed and Understood by

- 1) David [Signature] 4-6-71 (48-7185.)
- 2) [Signature] 4-8-71

Kennard Watson Harper  
Apr. 8, 1971



The system shown basically in Figure II shows the various parts:

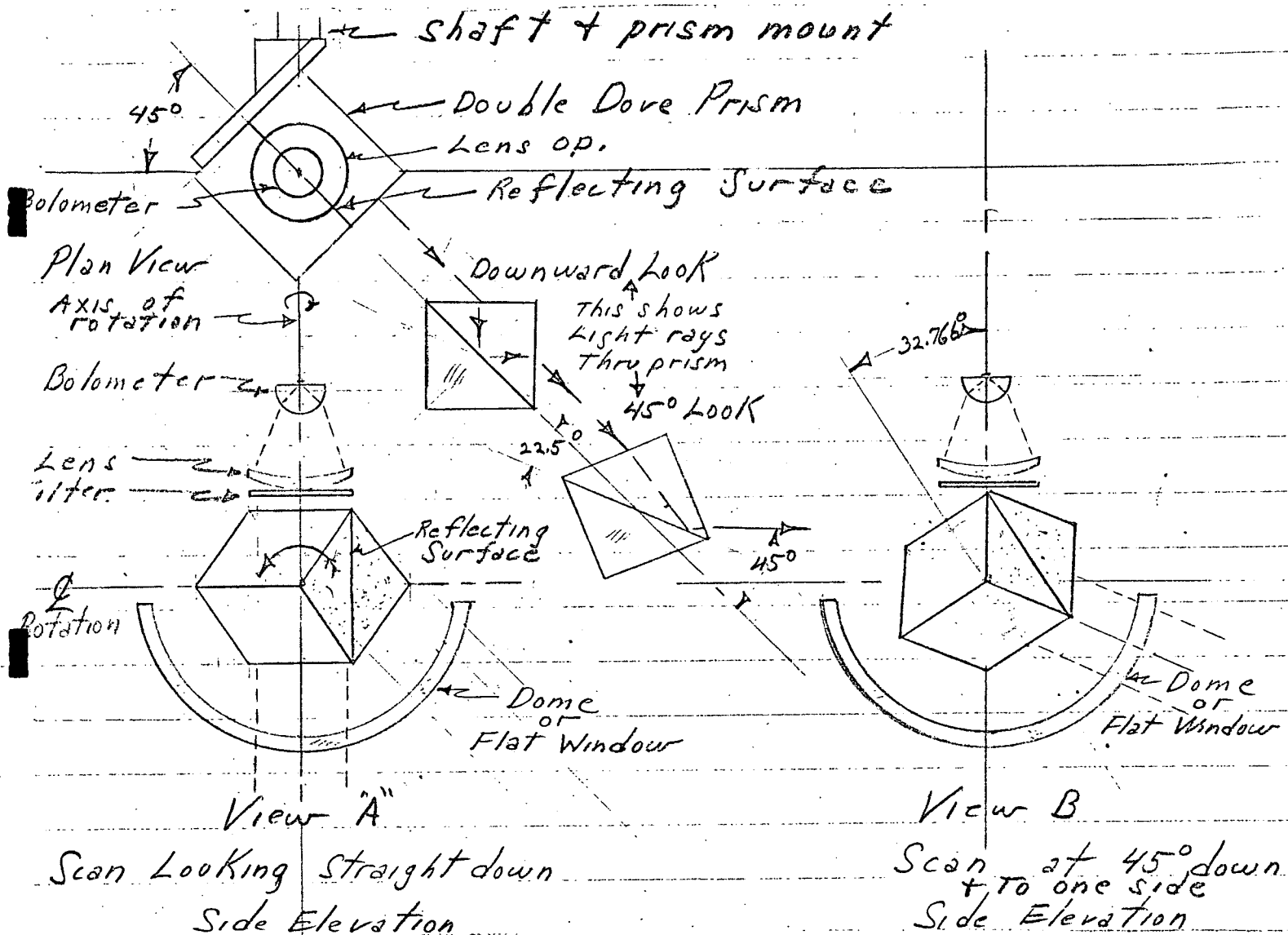


FIGURE II

The optical scanner consists of a bolometer (detector), a lens, a filter and substrate (cut on), a rotating double dove prism and a dome (or window).

Figure II view "A" shows the scanner looking at the center of the earth (the intersection of the two scans).

Invented by

Kennard Watson Harper April 1, 1971

Witnessed and Understood by

1) David Lowmyer 4-8-71

2) ~~Ernst~~ 4-8-71

71 *Kennard Watson Harper*  
Apr. 8, 1971

Figure II view "B" shows the scanner in a low orbit (at about 500 N. Mi. above the earth) looking at the horizon of the earth, about  $45^\circ$  from the vertical.

Figure II the view at  $45^\circ$  from the plan view shows the profile of the double dove prism and the  $45^\circ$  look shows it swung  $22.5^\circ$  to look at the edge of the earth.

Figure III shows the trace of rays through a typical double dove prism.

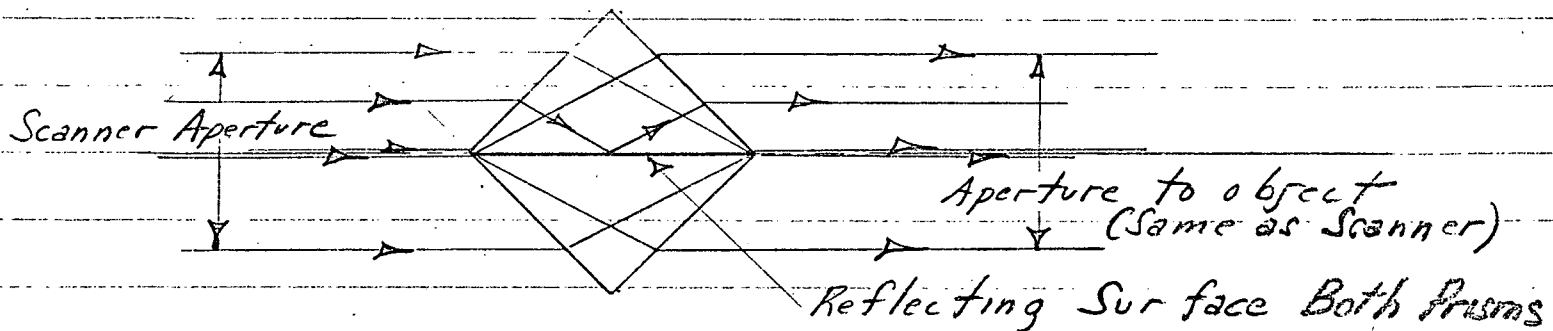


FIGURE 3

The index of refraction controls the prism length ratio to its height. The higher the index the shorter the prism. The prism design does have to be proportioned for its particular application. The face angles can be varied to accomplish this purpose.

- Claims -
- 1) One scanner head has two scan paths to control both pitch and roll for any altitude of orbit.
  - 2) One scanner drive with one axis of rotation can be oriented to its best position.
  - 3) There is one complete scan (two axis) with one revolution of the scanner drive, which means longer bearing life.
  - 4) The use of a double dove prism placed at a fixed angle of  $\theta/2$  Figure I controls angles of the scan pattern.

Invented by

Kennard Watson Harper April 1, 1971

Witnessed and Understood by

1) *Pavitt* 4-6-71

2) *E. E. Mott* 4-8-71

B

Claims - 5) The scan pattern angle  $\theta$  Figure I can be varied by simply changing the swing of the reflecting hypotenuse from the basic  $45^\circ$  to the desired angle.

Invented by

Kennard Watson Harper April 1, 1971

*Kennard Watson Harper Apr. 6, 1971*

Witnessed and Understood by

- 1) *David [Signature]* 4-6-71
- 2) *EE [Signature]* 4/6/71

# PATENT DISCLOSURE

## HORIZON SCANNER - ANY ALTITUDE SATELLITE

This is in addition to the disclosure of April 1, 1971.

This additional disclosure covers the special detector flake arrangement which is dictated by the tilting of the image due to the Double Dove Prism being tilted  $45^\circ$  to  $50^\circ$ .

When the dual flake (Sun rejection) bolometer is required the present two flake design will not work because the Double Dove Prism tilts the image  $90^\circ$ . The dual flakes will not cross the horizon simultaneously for both scans. That is, that two flakes are tangential to the earth.

This means that the arrangement of the flakes will be as shown by Figure 4 so that one pair will be tangential to the horizon on one leg of the crossing and the other pair will be tangential to the horizon on the other leg of the crossing. The middle flake ("C") is the common flake.

As the lens system flops the detector image over and around, Figure 5 demonstrates how this works.

The lens both inverts and reverts the individual flakes and whole pattern. This is shown by the intermediate aerial image.

In addition - the Double Dove Prism inverts the flakes and image due to the reflecting surface in the middle of the prism. This is shown by the last aerial image.

As the prism in its working position is tilted  $45^\circ$  to  $50^\circ$  from its normal position the flakes are tilted  $90^\circ$  to  $100^\circ$ . Figure 6 shows the Double Dove Prism tilted  $45^\circ$  which tilts the flakes  $90^\circ$ . If the prism were tilted  $50^\circ$  the flakes would be tilted  $100^\circ$ .

By placing these flakes as shown the first two flakes such as the Number 2 and common flake intersect the earth, and the Number 1 flake (trailing) can be blanked out as it isn't important. On the other half of the scan the Number 1 and common flakes will intersect the earth and the Number 2 (trailing) flake can be blanked out. The intersecting pair of flakes in each case is very nearly tangential to the earth. The tangential intersection is better at the higher altitude than at the lower altitudes.

Invented by

Kennard Watson Harper June 2, 1971

Witnessed and Understood by

1) *Paul [Signature]* 6-2-71

2) *[Signature]* 6/2/-71

*Kennard Watson Harper*  
6-2-71

Claim - That the three flake bolometer arranged as shown is required for sun rejection in the Double Dove Prism disclosure.

The three flakes can be rotated into other axes with the same result except it is felt that the logical operation dictates that the blanked or unused flake be the trailing one.

Invented by

Kennard Watson Harper June 2, 1971

Witnessed and Understood by

1) David [Signature] 6-2-71

2) [Signature] 6/2/71

Kennard Watson Harper  
6-2-71

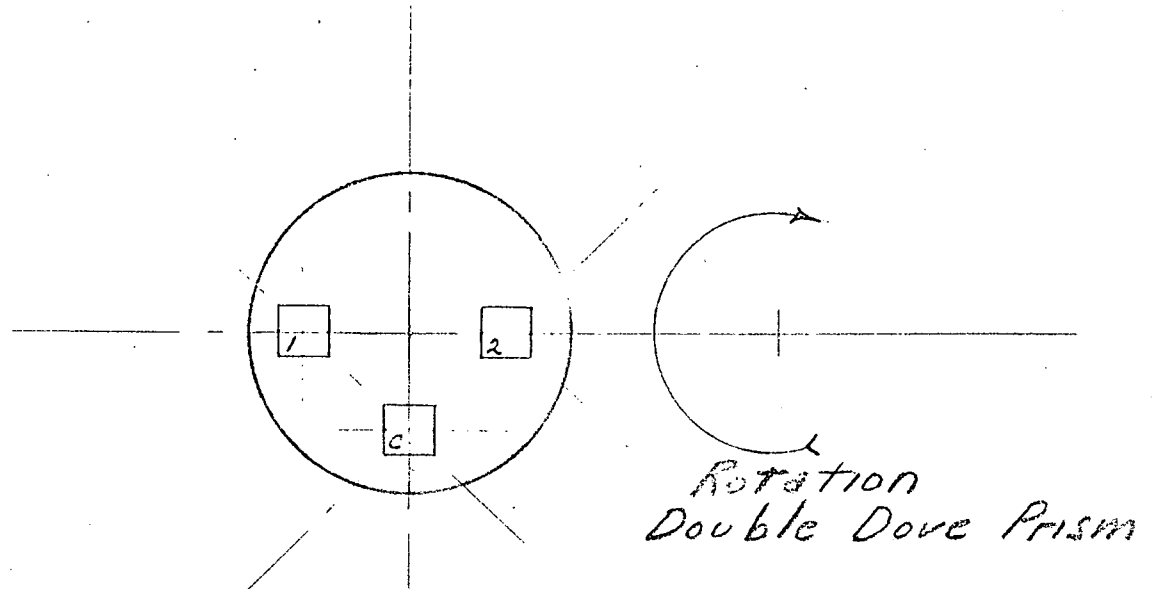


Figure No. 4

Bolometer positioned in scanner  
Looking at earth

Three flake bolometer  
"c" flake is common to both  
#1 + #2 flakes

Invented by

Kennard Watson Harper Apr. 26, 1971 / Kennard Watson Harper  
Witnessed & understood by

David [signature] 6-2-71

E. E. [signature] 6-2-71

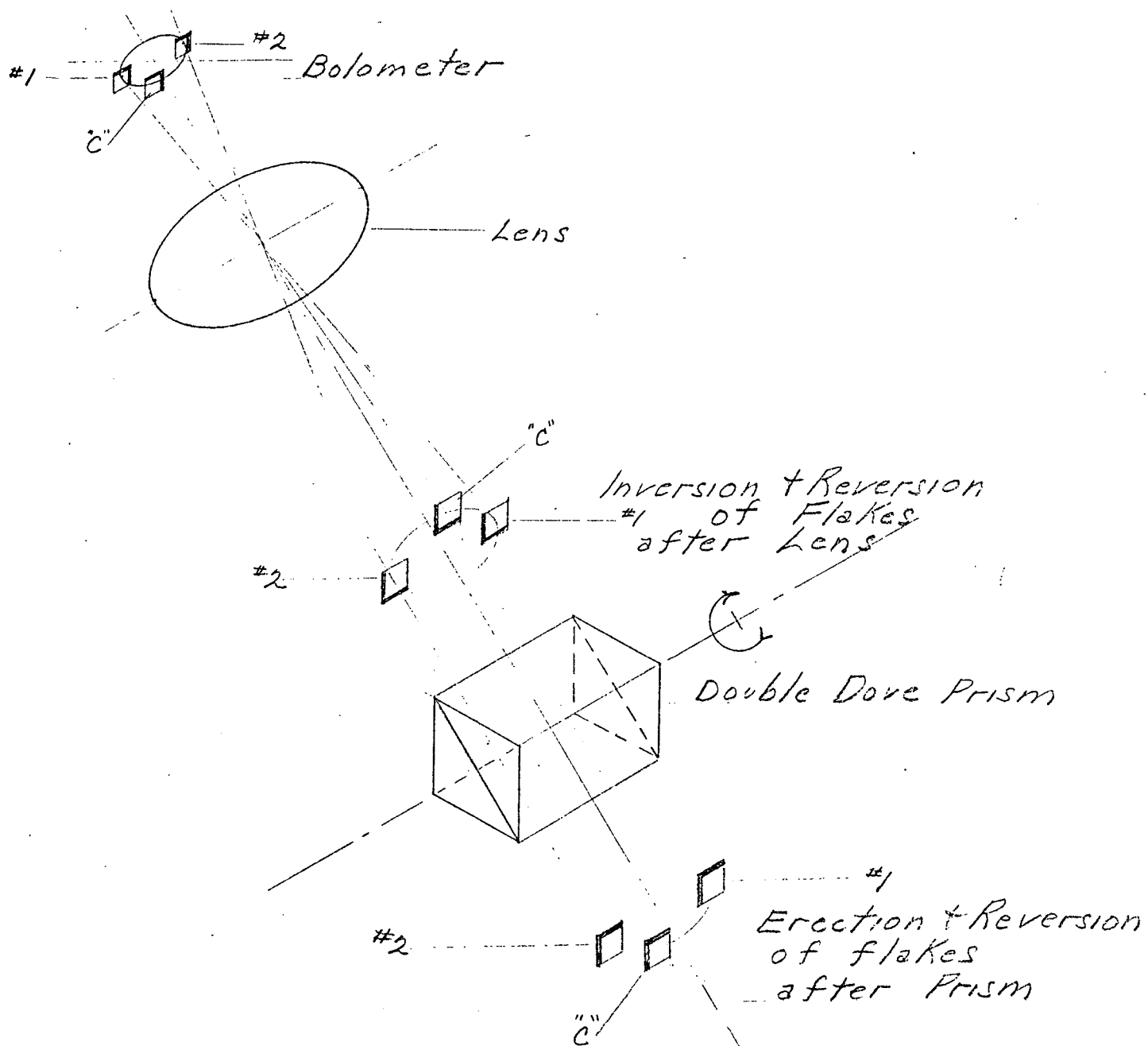
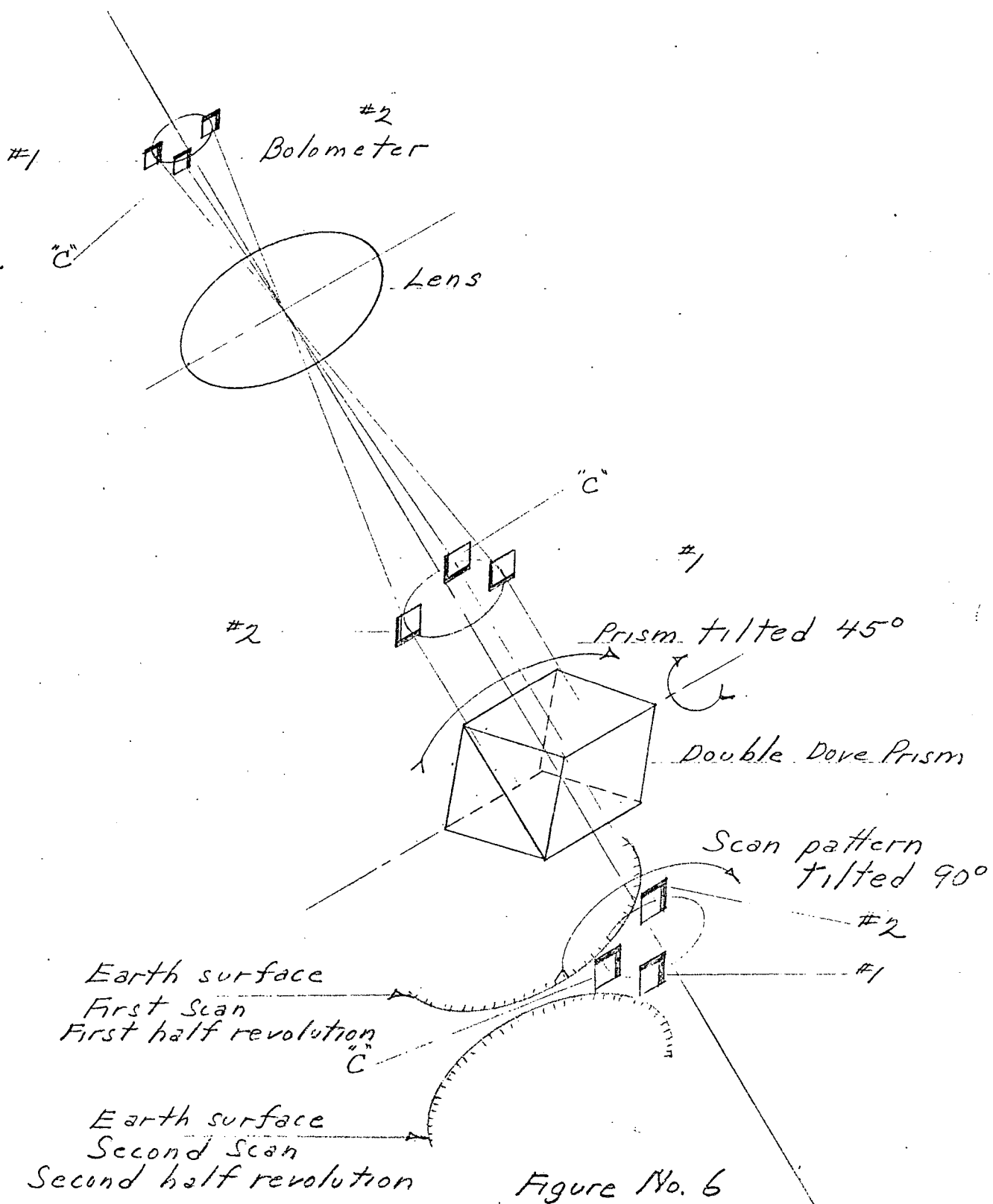


Figure No. 5

Invented by  
 Kennard Watson Harper Apr. 26, 1971 / Kennard Watson Harper  
 Witnessed & understood by  
 Paul [Signature] 6-2-71  
 [Signature] 6-2-71



Invented by  
Kennard Watson Harper Apr. 26, 1971 / Kennard Watson Harper  
Witnessed & understood by  
Paul D. [Signature] 6-2-71  
E. F. [Signature] 6-2-71



April 13, 1971

## MEMO

TO: File  
 FROM: D. Sonnabend  
 SUBJECT: X Scanner Beam Analysis

Consider a horizon scanner of the type described by Harper.\* The purpose of this memo is to determine the direction of the beam relative to the spacecraft at any position of the shaft or wheel. Assume a coordinate system with base vectors  $E_{\beta}^B$  fixed to the case. Suppose that the direction of the telescope as seen from the prism is  $E_1^B$ . Also suppose that the shaft axis on which the prism rotates is  $E_3^B$ .

Now, for the purpose of analysis, the double dove prism acts like a mirror whose reflecting surface is the total internal reflecting surface of the prisms. Both sides of this "mirror" reflect. We suppose that the mirror is fixed in a rotating coordinate system with base vectors  $E_{\alpha}^W$  which must obey the relation:

$$E_{\alpha}^W = R_{\alpha\beta}^3(\eta) E_{\beta}^B \quad (1)$$

Within  $E^W$ , the mirror is completely described by its unit normal  $U$ , which for definiteness we take as:

$$U = E_2^W \cos \lambda + E_3^W \sin \lambda = R_{2\alpha}^1(\lambda) E_{\alpha}^W \quad (2)$$

This definition is completely general, as any other arrangement at the same cant  $\lambda$  differs only by some fixed phase angle added to  $\eta$ . The mirror cant  $\lambda$  is suggested as  $\pi/4$  by Harper, but it is not necessary to pin it down in this analysis.

\*Patent Disclosure 4-6-71, by Kennard W. Harper

We define the beam direction by the unit vector  $V$ , and note that it is determined by reflecting the telescope  $E_1^B$  off the "mirror". Thus  $V$  must obey the vector relation:

$$E_1^B \times U = U \times V \quad (3)$$

Observe that replacing  $U$  by  $-U$  leads to the same result, so that both scans are included in the solution. It is easiest to express each vector in  $E^B$ . Accordingly:

$$U_\alpha^B = R_{\mu\alpha}^3(\eta) U_\mu^W = R_{2\mu}^1(\lambda) R_{\mu\alpha}^3(\eta) U_\mu^B$$

$$U^B = [-c\lambda s\eta, c\lambda c\eta, s\lambda] \quad (4)$$

The general cross product relation for  $C = A \times B$  is

$$C_\alpha = \epsilon_{\alpha\beta\gamma} A_\beta B_\gamma; \text{ and in this case we have:}$$

$$\epsilon_{\alpha\beta\gamma} U_\beta^B V_\gamma^B = \epsilon_{\alpha\beta\gamma} \delta_\beta^1 U_\gamma^B = \epsilon_{\alpha 1 \beta} U_\beta^B$$

so that:

$$(\epsilon_{\alpha\beta\gamma} V_\gamma^B + \epsilon_{\alpha\beta 1}) U_\beta^B = 0 \quad (5)$$

Now combining (4) and (5), a relation between the  $V_\gamma^B$  is produced for each value of  $\alpha$ . Working this out:

$$V_2^B s\lambda = V_3^B c\lambda c\eta \quad (6)$$

$$(V_1^B + 1)s\lambda + V_3^B c\lambda s\eta = 0 \quad (7)$$

$$(V_1^B + 1)c\eta + V_2^B s\eta = 0 \quad (8)$$

The systems (6)-(8) is homogenous in the variables  $V_1^B + 1$ ,  $V_2^B$ , and  $V_3^B$ ; so it is solvable only if the determinant of coefficients vanishes, and then only for the ratios of the  $V_\alpha^B$ . That the determinant vanishes is easily verified; so a further relation between the  $V_\alpha^B$  will produce a solution.

The relation  $\mathbf{E}_1^B \cdot \mathbf{U} = \mathbf{U} \cdot \mathbf{V}$  is true, but it is coplanar to (6)-(8), so it is no help.

The way out is that no use has been made of  $\mathbf{V} \cdot \mathbf{V} = 1$ . Substituting (6) and (7) into this gives:

$$(\mathbf{V}_3^B c \lambda s \eta + s \lambda)^2 + (\mathbf{V}_3^B c \lambda c \eta)^2 + (\mathbf{V}_3^B s \lambda)^2 = s^2 \lambda \quad (9)$$

The solution  $\mathbf{V}_3^B = \mathbf{V}_2^B = 0$ ,  $\mathbf{V}_1^B = -1$  is readily seen to be irrelevant. The remaining solution works out to:

$$\mathbf{V}_1^B = 2c^2 \lambda s^2 \eta - 1 \quad (10)$$

$$\mathbf{V}_2^B = -2c^2 \lambda s \eta c \eta \quad (11)$$

$$\mathbf{V}_3^B = -2s \lambda c \lambda s \eta \quad (12)$$

Equations (10)-(12) are a complete description of the beam for an X type horizon scanner.

It is of interest to determine the directions of motion of the beams. To find these we find the change in  $\mathbf{V}^B$  due to a change  $d\eta$ :

$$d\mathbf{V}^B = 2c \lambda d\eta [c \lambda s(2\eta), -c \lambda c(2\eta), -s \lambda c \eta] \quad (13)$$

These components are the direction numbers of the instantaneous rotation axis of the beam. Now at either  $\eta = 0$  or  $\eta = \pi$  we have  $\mathbf{V}^B = [-1, 0, 0]$ ; i.e., the beam is straight down from the telescope. At these values:

$$d\mathbf{V}^B(0) = 2c \lambda d\eta [0, -c \lambda, -s \lambda]$$

$$d\mathbf{V}^B(\pi) = 2c \lambda d\eta [0, -c \lambda, s \lambda]$$

Since the bracketed quantities are each of unit length, the angle  $x$  between the scans where they cross is:

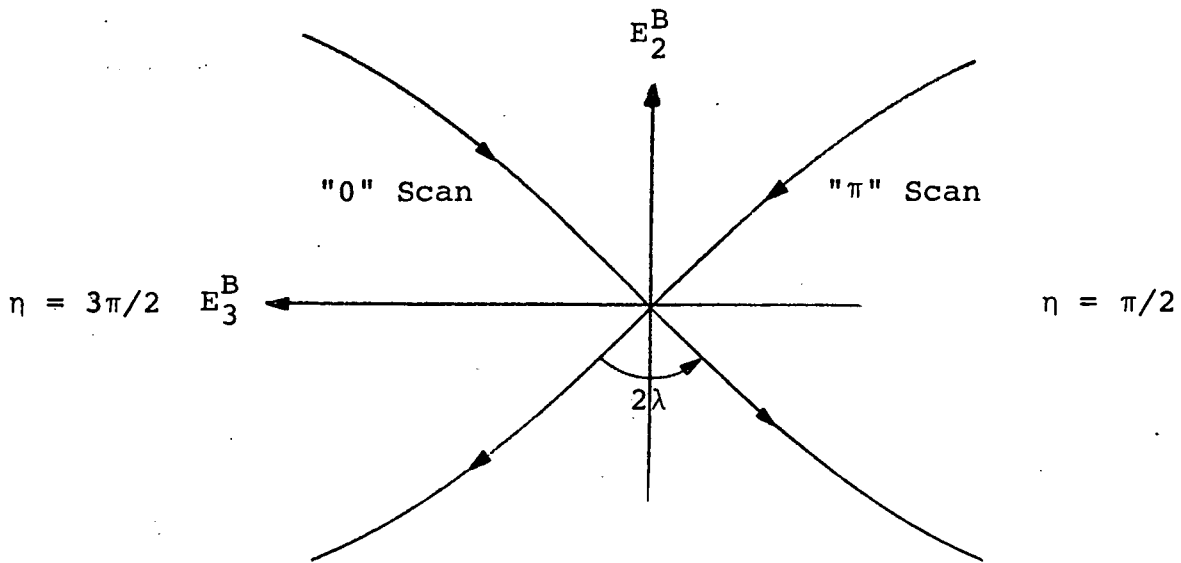
$$c x = c^2 \lambda - s^2 \lambda = c(2\lambda) \quad (14)$$

Thus the beam crosses itself at an angle  $2\lambda$ .

As a final note, if  $\lambda = \pi/4$ , the beam crosses itself at right angles and  $v^B$  has the special form:

$$v^B = -[c^2\eta, \operatorname{sn}\eta, \operatorname{sn}\eta] \quad (15)$$

Looking down from the telescope the projection of the beam will look essentially like this:



## MEMO

TO: File

FROM: D. Sonnabend

SUBJECT: X Scanner Computational Analysis for Small Angles

In a previous memo\* the Harper X Scanner was analyzed to determine the direction of the beam relative to its outer case, as a function of wheel (prism) position. Here this analysis will be extended to find the conditions at horizon crossings, and use these to obtain computational equations for the determination of satellite attitude and altitude. The main results are valid only for small attitude errors.

The notations of the previous memo will be preserved intact, but augmented to describe satellite attitude. We assume a reference or trajectory coordinate system with unit base vectors  $E_{\alpha}^T$  defined so that  $E_1^T$  is along the outward pointing radius vector from the earth's center,  $E_3^T$  is along the orbit normal as though the orbit were a right hand screw, and  $E_2^T$  is forward in the orbit plane to complete a right handed system. We suppose that the body fixed system  $E^B$  used in the previous memo is related to  $E^T$  by:

$$E_{\alpha}^B = F_{\alpha\beta} E_{\beta}^T \quad (1)$$

and for simplicity, suppose that  $F = I$  corresponds to no attitude error. This implies that the telescope looks straight down ( $-E_1^T$ ) when there is no error.

Since a horizon scanner can give no information about yaw (i.e., rotation about  $E_1^T$ ) it will prove convenient to factor  $F$  as follows:

$$F = AR^1(\psi) \quad (2)$$

To assure that the rotation A contains no yaw component, we will require that  $\psi$  be so chosen that the eigenvector of A is orthogonal to  $E_1^T$  whenever  $F \neq I$ ; if  $F = I$  then  $A = I$  and  $\psi = 0$ .

The angle  $\alpha$  between the beam axis V and the nadir  $-E_1^T$  is:

$$c\gamma = -V \cdot E_1^T = -V_{\alpha}^B E_{\alpha}^B \cdot E_1^T$$

and substituting from (1) this works out as:

$$c\gamma = -V_{\alpha}^B F_{\alpha 1}$$

Then using (2) we have:

$$c\gamma = -V_{\alpha}^B A_{\alpha 1} \quad (3)$$

The point of using A rather than F is that the analysis is not cluttered with an angle which cannot be determined.

In practice, (3) is useful whenever the beam crosses a horizon so that  $\gamma$  has the special value  $\gamma_e$  given by:

$$s\gamma_e = (1 + h/r_e)^{-1} \quad (4)$$

where h is the satellite altitude and  $r_e$  is the radius of the earth. Various effects such as clouds and oblateness introduce errors through (4) in that the horizons may not be affected symmetrically; but these will not be considered in this memo.

From the previous memo we may substitute the expressions for the  $V^B$  in terms of the prism angle  $\lambda$  and the wheel position  $\eta$ . When this is done each horizon crossing yields this relation:

$$(1 - 2c^2\lambda s^2\eta)A_{11} + 2c^2\lambda s\eta c\eta A_{21} + 2s\lambda c\lambda s\eta A_{31} = c\gamma_e \quad (5)$$

If the attitude error is not too great, there will be four distinct values of  $\eta$  corresponding to the four separate horizon crossings on each turn of the wheel. Thus four, not necessarily independent, relations exist for computing attitude. In sorting these out it is convenient to define the angle  $\eta_0$  by the relation:

$$c\gamma_e = 1 - 2c^2\lambda s^2\eta_0 \quad (6)$$

Only the first quadrant value of  $\eta_0$  will be used ( $0 < \eta_0 \leq \pi/2$ ). Now for the case of no error,  $A = I$  and it follows that  $s^2\eta = s^2\eta_0$ . The four possible solutions obviously correspond to the four horizon crossings, and one will occur in each quadrant. Thus, for no error, we can label the four  $\eta$  values by quadrant:

$$\eta_1 = \eta_0; \eta_2 = \pi - \eta_0; \eta_3 = -\pi + \eta_0; \eta_4 = -\eta_0$$

The physical significance of  $\eta_0$  is now evident -- it is the rotation of the wheel from when the beam is vertical to when it crosses the horizon, if there is no attitude error. It depends only on satellite altitude.

Using this null case as a guide, we can in general define a set of variations  $\delta\eta_i$  from null by these relations:

$$\eta_1 = \eta_0 + \delta\eta_1; \eta_2 = \pi - \eta_0 - \delta\eta_2; \eta_3 = -\pi + \eta_0 + \delta\eta_3;$$

$$\eta_4 = -\eta_0 - \delta\eta_4 \quad (7)$$

In general, the  $\delta\eta_i$  will be small if the rotation  $A$  is small. Returning now to  $A$ , for small rotations, any set of parameters will serve for computation, with equal facility. Accordingly, if we resolve  $A$  into pitch  $\theta$  and roll  $\phi$  by either  $A = R^3(\theta)R^2(\phi)$  or  $A = R^2(\phi)R^3(\theta)$ , then for small angles we have to first order:

$$A_{11} = 1, A_{21} = -\theta, A_{31} = \phi$$

Thus, from (5) and (6):

$$\phi \tan \lambda s \eta - \theta s \eta c \eta = s^2 \eta - s^2 \eta_0 = s(\eta + \eta_0)s(\eta - \eta_0) \quad (8)$$

It is clear that one of the terms on the right of (8) must be small. Substituting in the four definitions (7) clears this up, and after rejecting all second order terms the four equations become:

$$\phi \tan \lambda - \theta c \eta_0 = 2\delta \eta_1 c \eta_0 = 2(\eta_1 - \eta_0) c \eta_0 \quad (9)$$

$$\phi \tan \lambda + \theta c \eta_0 = 2\delta \eta_2 c \eta_0 = 2(\pi - \eta_2 - \eta_0) c \eta_0 \quad (10)$$

$$\phi \tan \lambda + \theta c \eta_0 = -2\delta \eta_3 c \eta_0 = 2(\eta_0 - \eta_3 - \pi) c \eta_0 \quad (11)$$

$$\phi \tan \lambda - \theta c \eta_0 = -2\delta \eta_4 c \eta_0 = 2(\eta_4 + \eta_0) c \eta_0 \quad (12)$$

The purpose of the  $\delta \eta_i$  in linearizing these relations has been served, and as they are not directly observable, they will now be ignored. Viewing (9-12) as a system of four equations in the three unknowns  $\phi$ ,  $\theta$ , and  $\eta_0$ , we see that there must be a relation between the observables  $\eta_i$ . To find this we compare (9) and (12) to get:

$$\eta_1 - \eta_0 = \eta_4 + \eta_0$$

and also (10) and (11):

$$\pi - \eta_2 - \eta_0 = \eta_0 - \eta_3 - \pi$$

This shows that  $\eta_0$  can be calculated by any of these:

$$\eta_0 = \frac{1}{2}(\eta_1 - \eta_4) = \pi + \frac{1}{2}(\eta_3 - \eta_2) = \frac{\pi}{2} + \frac{1}{4}(\eta_1 - \eta_2 + \eta_3 - \eta_4) \quad (13)$$

Thus the internal relation between the  $\eta_i$  is:

$$\eta_1 + \eta_2 - \eta_3 - \eta_4 = 2\pi \quad (14)$$



In practice, the amount by which (14) fails may be looked upon as a measure of the lack of circularity of the observed horizon. It is also possible to use (14) to adjust the  $\eta_i$  to improve the system accuracy. If  $\eta_x$  is the actual value on the left of (14), then the adjusted values of the  $\eta_i$  are  $\eta_i(2\pi/\eta_x)$ .

The pitch angle  $\theta$  can be found by subtracting (9) from (10) or (12) from (11):

$$\theta = \pi - \eta_1 - \eta_2 = -\pi - \eta_2 - \eta_4 = -\frac{1}{2}(\eta_1 + \eta_2 + \eta_3 + \eta_4) \quad (15)$$

Finally, the roll angle  $\phi$  may be obtained by adding (9) to (11) or (10) to (12):

$$\begin{aligned} \phi &= \cot\lambda c\eta_0(\eta_1 - \eta_3 - \pi) = \cot\lambda c\eta_0(\pi + \eta_4 - \eta_2) \\ &= \frac{1}{2} \cot\lambda c\eta_0(\eta_1 - \eta_2 - \eta_3 + \eta_4) \end{aligned} \quad (16)$$

In (16) the gain factor  $\cot\lambda$  is fixed by the design of the scanner. The factor  $c\eta_0$  however, is altitude dependent. It is possible to calculate it from (13), or, if the orbit is sufficiently circular, it may be precalculated and fixed, or its variation can be simply ignored. To see whether the latter may be feasible, this table, calculated from (4) and (6) may be useful. The radius  $\gamma_e$  is assumed to be 6367.37km = 3435.79nmi, and  $\lambda$  is taken to be  $\pi/4$ .

h-km	0	200	300	500	1000	5000	40,000
h-nmi	0	107.9	161.9	269.8	539.6	2698	21,584
$\gamma_e$	90°	75°49'	72°45'	68°0'	59°48'	34°4'	7°54'
$c\gamma_e$	0	.24491	.29659	.37459	.50303	.82839	.99052
$\eta_o$	90°	60°20'	57°0'	52°16'	44°50'	24°28'	5°35'
$c\eta_o$	0	.49488	.54460	.61203	.70925	.91016	.99525

Thus, above 300km, the gain will change by less than two to one for any higher altitude.